WASHINGTON UNIVERSITY IN ST. LOUIS

School of Engineering and Applied Science

Department of Energy, Environmental, and Chemical Engineering

Dissertation Examination Committee:
Daniel E. Giammar, Chair
Jeffrey G. Catalano
John D. Fortner
Young-Shin Jun
Li Li
Palghat Ramachandran

Sorption of Metals onto Natural Sediments and Engineered Iron Oxide Nanoparticles

by

Zezhen Pan

A dissertation presented to
The Graduate School
of Washington University in
partial fulfillment of the
requirements for the degree
of Doctor of Philosophy

August, 2017

Saint Louis, Missouri

Table of Contents

List of Figures

List of Tables

Acknowledgements

First and foremost, I am extremely thankful to my advisor Daniel Giammar who has been guiding and encouraging me throughout my Ph.D. life. His endless support and patience on my work, intellectual curiosity towards unknown and enthusiasm on research have given me confidence to face challenges and guided me to accomplish tasks. His insight into what makes a great researcher and mentor as well as his optimism have motivated me in every aspect of my life and will definitely continue. I feel grateful to him for providing with many multi-discipline collaboration opportunities, which inspired me continuously along my Ph.D. work.

I would like to acknowledge Jeff Catalano, John Fortner, Young-Shin Jun, Palghat Ramachandran and Li Li for agreeing to be members of my thesis committee and giving their valuable time and insightful suggestions along the course of this research. I would like to give my special thanks to Jeff Catalano, who helped me to identify many key scientific questions in the research project and provided me with novel perspectives and constructive suggestions throughout the collaborative project. I enjoyed working with Zheming Wang from PNNL, who is always ready to answer my questions and his expertise in LIFS contributed greatly to the project. John Fortner guided one of my rotations when I started in WUSTL and more importantly, his support on the nano-project made the transition of my research to a new field possible. I always enjoyed working with Li Li at Penn State University, whose expertise in modeling work has contributed in many ways to my work and her curiosity and input really made the collaboration possible. Young-Shin Jun and Palghat Ramachandran provided insightful suggestions to my

research and shared with many of their ideas. Meanwhile, they have given several of the most important courses that I have taken in WUSTL, which benefited my understanding from many aspects in my own research. I am grateful to my undergraduate advisor Ke Sun at Beijing Normal University, who brought me into the world of research, gave me hands-on instructions and encouraged me to graduate school.

I am so grateful to have opportunities to participate in projects with groups within and outside the university. The two collaboration projects with Zorimar Rivera-Nunez both showed me how strongly research can be related to human health and living environments. I would appreciate the opportunity offered by Michael Frachetti that I joined a field campaign of an archaeological study and applied the geochemical knowledge to a field study, which would be one of the most unforgettable experiences during my Ph.D. life. Special thanks to T.R. Kidder for his hand-on guidance of my geochemical field study skills and encouraging words in the site. I enjoyed working with Lyndsay Troyer, who has been very supportive in the Hanford project and offered me help whenever needed. Special thanks to Hang Wen (PSU), who has devoted time to work with me to develop a model with his modeling expertise. Thanks to Wenlu Li for providing first batch of nanoparticles that I could quickly start my second project. Many thanks are due to Sanmathi Chavalmane, Patty Wurm, Remya Nair and Huafang Li and Paul Carpenter, for their help in training me on various analytical instruments. I would also want to extend my gratitude to department staffs for their endless support, especially to Rose Baxter.

The Aquatic Chemistry Laboratory (ACL) has been a most wonderful place that I have stayed, where I received countless help and support from my peers, past and present.

Lin Wang mentored me for my research rotation and got me started in our lab. My sincere thanks to Vrajesh Mehta, who served as my mentor, shared me with his knowledge and experience and guided me to build up my very first experiment system. He was always available and willing to answer my questions. Rachel Wells, Wei Xiong, Chao Pan, Yeunook Bae, Peng Liao and Ao Qian are always ready to help and give my helpful feedback to improve my research. I appreciate the opportunities to mentor and work with rotation students, undergraduates and high school students, including Zongsen Zou, Qingqing Zeng, Anshuman Satpathy, Yi-Ling Lin, Manvitha Marni, Anna Ivarson, Xiaoming Zhu and Nevel Vaidyan. I would like to thank Daniel Giammar and Jay Turner, for giving me the opportunity to serve as a teaching assistant. The TA experience in Environmental Engineering lab involved me into great interactions with undergraduates that made the experience so rewarding. I cannot forget colleagues and friends within and outside the department, who went through hard times together, cheered me on, and celebrated each accomplishment, which have been making my Ph.D. life enjoyable.

This work was supported by the U.S. Department of Energy (DOE) Subsurface Biogeochemical Research Program (Award No. DE-SC0006857), National Science Foundation (CBET, Award #1437820) and the International Center for Advanced Renewable Energy and Sustainability (I-CARES).

Finally, my biggest and deepest thanks go to my parents, Renfa Pan and Xinjuan Wen, for their long-distance love and encouragement, for their unlimited support on my every decision and for all the time they want me to be happy and to understand myself and the world that have shaped me into who I am. To my grandma, to my family, to the ones beloved, I dedicate this dissertation.

Zezhen Pan

Washington University in St. Louis

August 2017

ABSTRACT OF THE DISSERTATION

Sorption of Metals onto Natural Sediments and Engineered Iron Oxide Nanoparticles

by

Zezhen Pan

Doctor of Philosophy in Energy, Environmental, and Chemical Engineering

Washington University in St. Louis, 2017

Professor Daniel Giammar, Chair

Metal contamination of subsurface environments and engineered water systems can be derived from natural processes and anthropogenic activities associated with industrial processes, past weapons production, and mining works. The toxic and carcinogenic effects of uranium and chromium pose a significant risk to the environment and human health. For uranium contamination in subsurface environments, phosphate addition has been performed for in-situ immobilization, which can avoid the costs associated with pump-and-treat or excavation-based remediation strategies. The interactions of uranium and phosphate in Hanford sediments had been insufficiently explored in terms of its site-specific groundwater chemistry and aquifer sediment properties. For water treatment system, novel materials such as engineered magnetite nanoparticles have gained attention due to their promising performance in separating heavy metals from the aqueous phase. As a result, the study of the interaction between metals with either sediments or nanocomposites is imperative in designing and implementing subsurface in-situ remediation and improving water treatment processes.

To investigate the impact of phosphate on the immobilization of U(VI) in Hanford sediments, batch and column experiments were performed with artificial groundwater prepared to emulate the conditions at the site. Batch experiments revealed enhanced U(VI) sorption with increasing phosphate addition. X-ray absorption spectroscopy (XAS) measurements of samples from the batch experiments found that U(VI) was predominantly adsorbed at conditions relevant to most field sites (low U(VI) loadings, < 25 μM), and U(VI) phosphate precipitation occurred only at high initial U(VI) (>25 μM) and phosphate loadings. While batch experiments showed the transition of U(VI) uptake from adsorption to precipitation, the column study was more directly relevant to the subsurface environment because of the high solid:water ratio in the column and the advective flow of water. In column experiments, more U(VI) was retained in sediments when phosphate-containing groundwater was introduced to U(VI)-loaded sediments than when the groundwater did not contain phosphate. This enhanced retention persisted for at least one month after cessation of phosphate addition to the influent fluid. Sequential extractions and laser-induced fluorescence spectroscopy (LIFS) of column sediments suggested that the retained U(VI) was primarily in adsorbed forms. These results indicate that in-situ remediation of groundwater by phosphate addition provides lasting benefit beyond the treatment period via enhanced U(VI) adsorption to sediments. U(VI) transport through sediment-packed columns have been demonstrated to be kinetically controlled and the heterogeneous system contributed to the transport behavior under different flow rates.

In water treatment processes, surface-functionalized magnetite nanoparticles have high capacity for U(VI) and Cr(VI) adsorption and can be easily separated from the

aqueous phase by applying a magnetic field. A surface-engineered bilayer structure enables the stabilization of nanoparticles in aqueous solution. Functional groups such as carboxylic or amine groups in stearic acid (SA), oleic acid (OA), octadecylphosphonic acid (ODP), and trimethyloctadecylammonium bromide (CTAB) coatings led to different adsorption extents towards U(VI) and Cr(VI). The adsorption of U(VI) to OA-coated nanoparticles was examined as a function of initial loading of U(VI) (5-15 μM), pH (4.5 to 10), and the presence or absence of carbonate. CTAB-coated nanoparticles possess higher Cr(VI) adsorption affinity than nanoparticles with carboxyl groups (SA), due to the strong electrostatic interactions between opposite charges. For both U(VI) and Cr(VI), the entire adsorption dataset were successfully simulated with surface complexation models with a small set of adsorption reactions. The results show that the adsorption behavior was related to the changing aqueous species and properties of surface coatings on nanoparticles. The models could also capture the trend of pH-dependent surface potential that are consistent with measured zeta potentials.

While developing novel materials for metal removal, the stability and treatment efficiency of the material need to be tested in real water systems. The application of CTAB-coated nanoparticles was tested with the presence of two drinking water supplies, and decreases in Cr(VI) adsorption were associated with the presence of Ca^{2+}. When the Ca^{2+} concentration increased from 0 to 3.3 mM, adsorption decreased. Because only slight aggregation was associated with Ca^{2+} and an observed increase in zeta potential with Ca^{2+} addition should actually enhance Cr(VI) adsorption, the causes of inhibition of Cr(VI) by Ca^{2+} are not associated with particle size or surface charge. Instead it is likely

that Ca^{2+} influences the structure of the organic bilayer on the nanoparticle surfaces in a way that decreased the availability of surface sites.

The information gained from these research projects improved our understanding of metal interactions with both sediments from subsurface environments and engineered nanoparticles. It broadened knowledge of the controlling processes during the in-situ remediation of field sites and the separation of heavy metals from in water treatment. For remediation, the results illustrate the consideration of optimizing the timing and doses of phosphate addition in remediation strategies could lead to slower U(VI) release with effectively controlled levels. For water treatment the application of the material-based treatment processes needs more consideration of its stability and treatment performance with real water resources.

Chapter 1. Introduction

1.1 Background and Motivation

The contamination of heavy metals and radionuclides in soils and drinking water system is a serious public health concern due to their toxic and carcinogenic effects. Interfacial interactions between solid and aqueous phases can control the fate and transport of metals and radionuclides in subsurface environments as well as the removal of metals from aqueous phase for water purifications. Uranium contamination of soil and groundwater is largely due to the past weapon productions, mining processes and waste disposal activities. Uranium contamination of subsurface environments in the U.S. is widespread with more than 120 DOE contaminated sites across 36 states (Palmisano and Hazen 2003). The drinking water standard of uranium is 30 µg/L based on its chemical toxicity, and radiological effects are another concern for human health. Chromium contamination has both natural and anthropogenic sources. A current national drinking water standard of 100 µg/L is set for total chromium. However, California has specifically set the standard for Cr(VI) as 10 µg/L, which can drive the need for deployment of treatment processes at utilities that had not been previously needed.

1.1.1 Aqueous uranium geochemistry and associated uranium sorption processes

In environmental systems, uranium exists primarily in the oxidation states of U(IV) and U(VI) (Figure 1.1). U(VI) exists as uranyl ion, and forms uranyl-

carbonates and uranyl-hydroxides. Adsorbed forms of U(VI) on iron oxides and clays have been observed in uranium contaminated field sites. Precipitation of U(VI)-phosphate species could lower the solubility of uranium in oxic conditions. U(IV) is primarily found as uraninite UO_2(s) in reducing environments and has low solubility. The remediation of uranium has been conducted in many field sites through biotic or abiotic processes, which reduces U(VI) to U(IV) to achieve immobilized uranium. However, long-term stability of reduced UO_2 is a concern when the site is exposing to oxic conditions. As a result, the immobilization of U(VI) species can serve as a stand-alone method or a complement method to bioremediation. U(VI) can be adsorbed to many forms of iron oxides that are naturally abundant in sediments.

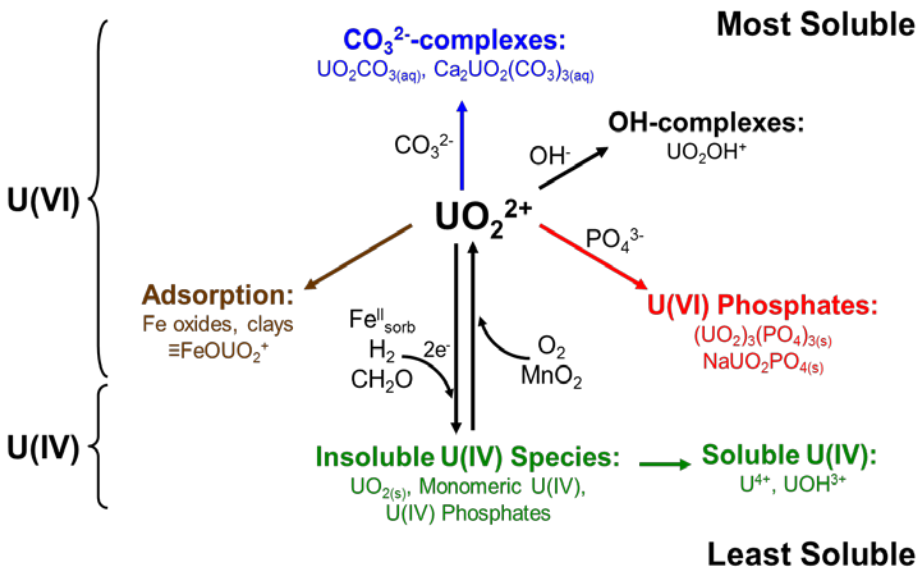

Figure 1.1. Overview of uranium aqueous biogeochemistry

Interfacial interactions between metals with natural sediments are relevant to the fate and transport of uranium in sediments collected from the Hanford 300 Area,

which is a widely studied uranium contaminated site where two process ponds received 58,000 kg of U from 1943 to 1975 (Catalano et al. 2006). The contamination of groundwater and soil occurred as a result of direct injection of mixed waste into the subsurface, leakage from storage tanks, and infiltration from unlined storage ponds into the surrounding media. The water table at this site is influenced by the stage of the nearby Columbia River, and released uranium can be mobilized from the sediments when the water table rises during high river stages. In the alkaline pH range, U(VI) exits as aqueous complexes with carbonate, hydroxide and phosphate whose predominance changes with changing pH and concentrations of carbonate and phosphate (Figure 1.2).

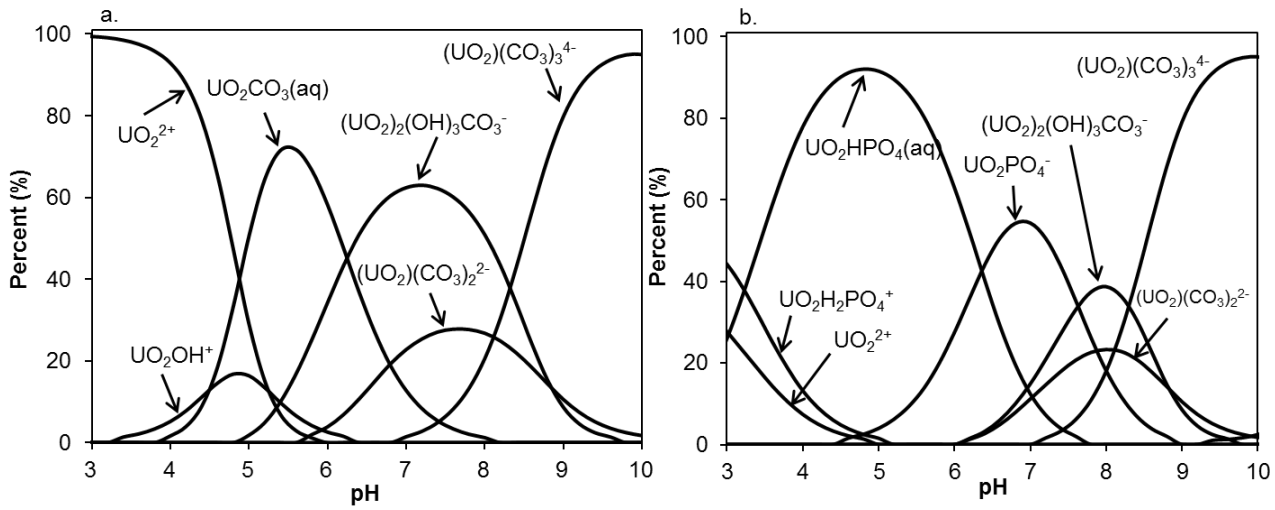

Figure 1.2. Speciation calculations predicted using the equilibrium modeling system MINEQL+, v 5.0, with the thermodynamic constants listed in Appendix A, Table A.1. No precipitation of solids was considered. a. TOT U=4 µM, TOT CO_3 = 1 mM, closed to atmosphere; b. TOT U=4 µM, TOT CO_3 = 1 mM, TOT PO_4= 1 mM, closed to atmosphere.

In-situ immobilization of uranium can avoid the costs associated with pump-and-treat or excavation-based remediation strategies. In natural systems, uranium has

been observed to be immobilized by the presence of uranyl phosphate minerals (Jerden et al. 2003, Fuller et al. 2002). The potential mechanisms responsible for uranium immobilization after phosphate addition include precipitation of low solubility uranium phosphates, enhanced adsorption to minerals originally present, and adsorption or incorporation into newly formed calcium phosphate minerals such as hydroxyapatite (Fuller et al. 2002, Shi et al. 2009 and Mehta et al. 2016). Several laboratory studies have shown that uranyl phosphate phases can precipitate quickly at acidic to circumneutral pH (Mehta et al. 2014, Kanematsu et al. 2014). Adsorption of uranium to iron oxides (such as ferrihydrite and goethite) can be enhanced by the presence of phosphate through the formation of ternary surface complexes and changing surface charge (Singh et al. 2012, Cheng et al. 2004).

The extent of U(VI) adsorption to natural sediments varies depending on sediment mineralogy and the aqueous solution's inorganic carbon level, pH, and total dissolved solids (Barnett et al. 2000, Serne et al. 2002 and Stoliker et al. 2011). For example, because of high dissolved inorganic carbon (DIC) and calcium concentrations, experiments conducted with Rifle sediments showed only slight retention of U(VI) upon phosphate addition because the ternary Ca-U(VI)-carbonate species were dominant and have higher solubility and lower sorption affinity to the sediments (Mehta et al. 2015). As a result, the effectiveness of phosphate treatment may vary greatly depending on the site-specific mineralogy and groundwater chemistry, especially the pH and carbonate concentration. Further, the fate of the U(VI) after stopping phosphate injection remains unknown.

1.1.2 Chromium water chemistry and application of nanoparticles

Investigation on the interactions between metals and novel nanocomposites would benefit the future application of the sorbents for water purifications. Similar to uranium speciation, the predominant chromium species changes with changing water chemistry (Figure 1.3). Cr(III) is primarily found as cationic species, while toxic Cr(VI) occurs as the anions chromate (CrO_4^{2-}) and biochromate ($HCrO_4^-$).

Iron oxide nanoparticles can be more effective sorbents than larger iron oxides and other sorbents due to their large specific surface area, high dispersion, high surface reactivity and ease of surface modification (Zeng et al. 2008, Xu et al. 2012 and Wang et al. 2012). Iron-oxide nanoparticle surfaces can be modified with a variety of materials (humic acid, polymers and fatty acids) (Ge et al. 2015, Jiang et al. 2014) (Ge et al. 2015, Jiang et al. 2014) that can stabilize nanoparticles while maintaining the ability to remove metal contaminants (U(VI), As(V), Cu(VI) and Cr(VI)). Humic acid-covered magnetite particles effectively removed the metal contaminants Hg(II), Pb(II), Cd(II) and Cu(II) from tap water and natural waters at pH from 2 to 9 (Liu et al. 2008). Functional groups of humic acid were also reported to be responsible for the reduction of Cr(VI) to non-toxic Cr(III) (Jiang et al. 2014). Chitosan (polysaccharide)-bound magnetic nanoparticles were prepared for removal of Cu(II) ions (Chang et al. 2005). Manganese ferrite/magnetite nanoparticles coated with fatty acids have been applied for U(VI) sorption. NH_2-functionalized nanomagnetic polymer adsorbents (NH_2-NMPs) have been studied for Cr(VI) removal that had adsorption mechanisms as electrostatic attraction, ion exchange and coordination interactions (Zhao et al. 2010). However, the impact of water chemistry

on the adsorption of U(VI)/Cr(VI) to magnetite coated with fatty acids had not previously been evaluated with respect to systematic variation in the water chemistry.

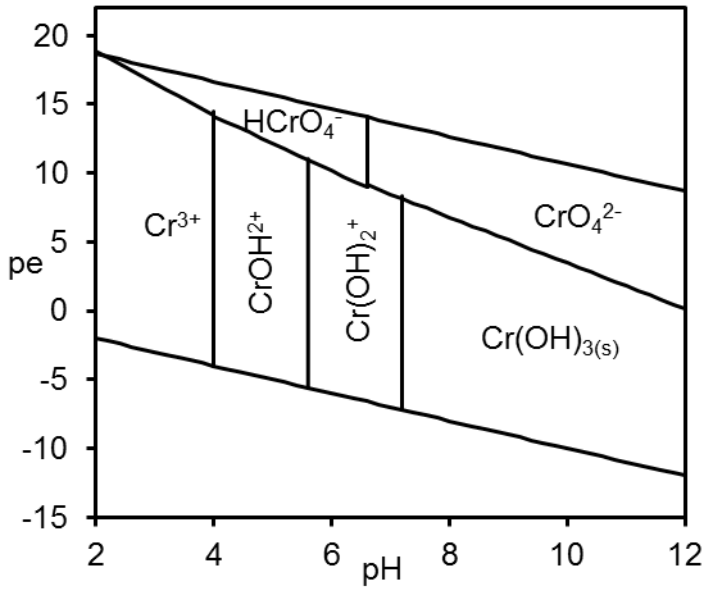

Figure 1.3. pe-pH diagram for chromium species with pH from 2 to 12, TOTCr = 0.1 µM.

While developing novel materials for metal removal, the stability and treatment efficiency of the material needs to be tested in real water systems. Of particular concern is the potential for nanoparticle suspensions to become destabilized and for nanoparticles to aggregate such that their effective surface area is greatly reduced. Aggregation of oleic acid-coated nanoparticles at pH 7.2 by Na^+ and Ca^{2+} has been reported with critical coagulation concentrations of 710 mM and 10.6 mM, respectively (Li et al. 2014). These are high concentrations relative to those that will be encountered in drinking water treatment. In a previous study with a natural water with dissolved Ca^{2+} and Mg^{2+}, these solutes did not influence Cu^{2+} removal by NH_2-NMPs (Hao et al. 2010). However, the impact of cations/anions on Cr(VI) adsorption to amine functionalized nanoparticles remains unknown as Cr(VI)

is present as anionic forms that may respond differently than the cationic Cu(II) species studied in that earlier work.

1.1.3 Surface Complexation Modeling and Reactive Transport Modeling

Surface complexation modeling (SCM) is a quantitative tool for predicting metal adsorption in a reaction-based framework that accounts for the full aqueous speciation, surface chemical reactions, and the impacts of surface potential on the adsorption of charged species (Wang et al. 2012, Xie et al. 2016). SCM accounts for the impact of water chemistry on aqueous and surface speciation in predicting adsorption over a broad range of conditions with a set of reactions and corresponding reaction constants (Wang et al 2013). Metal adsorption has been described by various types of SCMs. For U(VI) adsorption to solids that are comprised of multiple types of adsorbents, a non-electrostatic model can be applied, such as was done for modeling the U(VI) adsorption to Hanford sediments (Stoliker et al. 2011). The diffuse double layer model is one of most widely used electrostatic SCMs that accounts for the energetics associated with both chemical binding to the sorbent surface and electrostatic interactions between solutes and sorbent surfaces, which is suitable for understanding contaminant adsorption to minerals in sediments and to sorbents used in water treatment. A diffuse double layer model includes a compact layer and a diffuse layer. A schematic of the interfacial structure is shown in Figure 1.4. The compact layer contains all specifically adsorbed ions. The diffuse layer starts from the *d* plane and contains non-specifically adsorbed ions at concentrations

that differ from their values in bulk solution. These ions are attracted to or repelled from the surface due to electrostatic interactions. The relation between the charge and the potential at the *d* plane can be determined based on the Gouy-Chapman equation (Equation 1.1) (Benjamin 2014):

$$\sigma_d = -0.1174 C_s^{0.5} sinh \frac{zF\psi_d}{2RT} \qquad \text{Equation 1.1}$$

where σ_d is the equivalent charge density (C/m^2), F as the Faraday constant (96,485 C/mol), C_s is the electrolyte concentration (mol/L), z is the absolute value of the ionic charge number of the electrolyte ions, ψ_d is the electrical potential in the d plane (V), R is the gas constant (8.314 J/mol-K) and T is temperature (K).

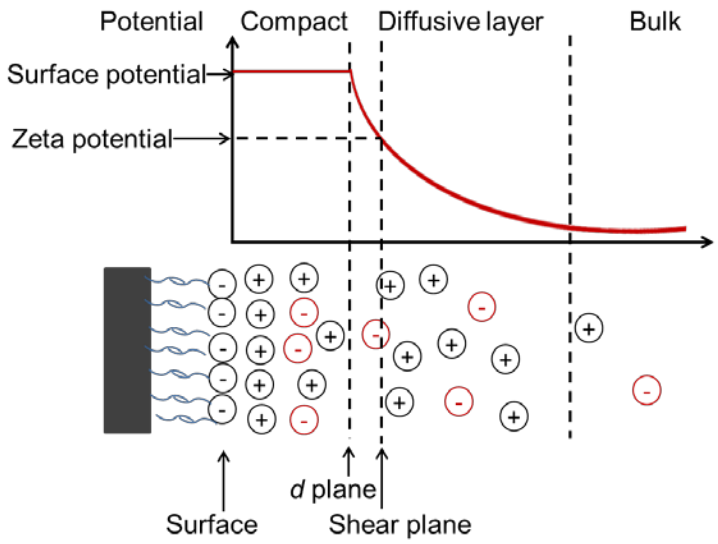

Figure 1.4. Profiles of potentials versus distance from the surface (assuming negatively charged nanoparticle surface). The locations of the surface, *d* plane and shear plane are indicated in the schematic diagram.

When adsorption of ions to a charged surface occurs, the change of both chemical and electrical potential energy can result in different criterion for the reaction equilibrium, with an activity coefficient ($\gamma_{i,\ ext}$) accounting for the imposed

electrical potential from the external side. Based on that, the intrinsic equilibrium constant K_{int} would not only consider the chemical interactions but also the electrical interactions and it is linked to the apparent adsorption equilibrium constant K_{app} by $\gamma_{i,\ ext}$ (Equation 1.2). When applying a SCM that accounts for electrostatic contributions to adsorption, this modification of the intrinsic equilibrium constant to yield an apparent equilibrium constant needs to be considered in the model (Benjamin 2014).

$$\gamma_{i,\ ext} = \exp[z_i F \psi_{i,ext}/(RT)] \qquad \text{Equation 1.2}$$

While studying the interactions between dissolved metals and charged surfaces, it is important to consider the concepts of zeta potential and surface potential (Figure 1.4). The surface potential is defined as the electrokinetic potential between the surface and any point in the mass of the suspending liquid. Zeta potential is the electrical potential at the shear plane, which is a small distance from the surface and separates the mobile fluid from fluid attached to the surface. The zeta potential is a key indicator of the stability of colloidal dispersions. As the surface potential cannot be measured directly, zeta potential can be used to provide qualitative information about the electrical properties of the surface.

In most previous studies that used SCM to interpret U(VI) adsorption to a material, the adsorption sites were the hydroxyl groups at the surface of inorganic solids (e.g., iron oxides, aluminum oxides, or clay minerals) (Zeng et al. 2009 and Xu et al. 2006). SCM can be applied for uranium adsorption to site-specific sediments and can be used to predict sorption behavior for untested conditions and provide reference information for future in-situ remediation. However, the ability to apply SCM to understand the binding of adsorbates to functional groups of organic

compounds that are coated on the surface of an inorganic solid had not previously been unexplored. Whether or not modeling metal adsorption to such functionalized metal oxide sorbents must still consider electrostatic contributions to adsorption in addition to the chemical binding to the functional groups remained an open question when we designed our experiments.

Removal of contaminants in groundwater and in columns loaded with sorbents is controlled by advective flow, rates of diffusive mass transfer, reactions in the aqueous phase and sorption reactions on surface sites. Column studies have been applied to evaluate transport behavior of heavy metals through porous media (Qafoku et al. 2005, Surasani et al. 2013). Many modeling studies have been conducted to describe processes affecting metal transport in columns. When integrated with ion exchange or surface complexation, a one-dimensional transport model was applied to model the effect of bicarbonate on U(VI) desorption from contaminated sediments at the Rifle site (Fox et al. 2012). A study on arsenate removal by an iron oxide-based sorbent in a packed bed used a pore and surface diffusion model, where the column is considered to have mobile and immobile zones and a diffusion process was included between two zones. A multi-rate SCM has been implemented into a transport model to predict the long-term rate of uranium desorption from Hanford sediments (Shang et al. 2014). Reactive transport models can be strong tools to identify and understand the processes that control the fate and transport of metals in laboratory and natural systems and provide insights for site remediation.

1.2 Research Objectives

The overall objective of this project was to investigate interfacial interactions of metals between aqueous and solid phases and determine the dominant mechanisms during the uptake process, coupled with modeling approaches. The project focuses on metal sorption behavior related to two systems, one as the subsurface environments and the other as the drinking water treatment system.

The fate and transport of U(VI) are strongly related to site-specific subsurface environments, where the presence of different constituents (pH, calcium and carbonate) can affect the interactions during the phosphate-induced immobilization through various pathways. Batch reaction systems represent equilibrium conditions and various conditions could be tested to explore the broad reaction mechanisms of U(VI) sorption by sediments and the effect of phosphate additions. More importantly, non-equilibrium interactions between U(VI) and sediments with the presence of phosphate needed to be studied and be more strongly related to the in-situ remediation. To improve our understanding towards U(VI) uptake by natural sediments and the impact of phosphate addition, two specific research objectives were pursued.

Objective 1: to identify the dominant processes responsible for phosphate-induced U(VI) immobilization for sediments and groundwater of the Hanford 300 Area.

Objective 2: to quantify the extent and longevity of U(VI) uptake under equilibrium and non-equilibrium conditions by modeling development.

The investigation on the interactions between U(VI) or Cr(VI) and engineered nanoparticles and the evaluation treatment efficiency of nanoparticles in complex systems can benefit the future development of novel materials and their application in real drinking water treatment processes. Surface-modified magnetite nanoparticles had not previously been evaluated with respect to systematic variation in the water chemistry towards metal uptake. To achieve the understanding of metals uptake by novel nanocomposties, two objectives were pursued.

Objective 3: to identify the impact of surface coatings and water chemistry on U(VI) and Cr(VI) adsorption by engineered iron oxide nanoparticles and the development of SCM

Objective 4: to evaluate nanoparticle adsorption performance with more complex and realistic drinking water sources.

1.3 Research Approach

To meet the objectives outlined above, a series of laboratory experiments were designed and conducted. Multiple reactor techniques were used to quantify the rate and equilibrium of various solid:water interactions. Batch adsorption equilibrium experiments allowed understanding of the fundamental mechanisms of phosphate induced uranium retention in sediments and the separation of metals from aqueous phase by engineered nanoparticles under equilibrium. Batch kinetic studies enabled an investigation of the reaction rate, which reveals the controlling steps during the interactions. A set of experiments that required maintenance of CO_2-free

conditions were performed in a controlled-atmosphere chamber, helping to understand the impact of dissolved inorganic carbon on metal sorption behavior. Control experiments were always performed to support the experiments. Column experiments integrated various physical-chemical processes that are more closely related to the real subsurface environments. Controlling the stability and maintenance of system were critical for operating the flow-through experiments.

For both batch and column systems, speciation calculations were used to understand the status of aqueous species and interpret the reaction pathways, based on measurements of aqueous species. Comparing the results from batch and column experiments enabled understanding of the impact of mass transfer processes on overall U(VI) transport. In all experiments, an approach was followed that integrated aqueous phase analysis, solid phase characterizations and modeling development. Inductively coupled plasma mass spectrometry (ICP-MS) was used as the primary analytical method for dissolved metal concentrations. Total organic carbon (TOC) analysis was used to measure dissolved inorganic carbon/organic carbon concentrations. Multiple solid characterization techniques were employed for systems with sediments and nanoparticles. X-ray diffraction (XRD) was used to identify the mineral compositions of field sediments. Extended X-ray absorption fine structure (EXAFS) was used to characterize the atomic coordination environments, which was important to understand coordination environments of uranium in molecular-scale. Sequential extractions were conducted to determine the mass of U(VI) accumulated and identify the dominant species of U(VI) in sediments. Laser induced fluorescence spectroscopy (LIFS) was employed to identify the presence of

various forms of U(VI)-associated solids. For the system with nanoparticles, transmission electron microscopy (TEM) was used to image synthesized nanoparticles to determine the shape and size. Dynamic light scattering (DLS) was able to measure the surface potential and the hydrodynamic diameter of nanoparticles.

1.4 Overview of Dissertation

This project was operationally divided into two main tasks, one of each in accordance with the four objectives outlined before. Each task included several subtasks that are addressed in corresponding chapters.

Task 1. Evaluation of the effect of phosphate on the immobilization of U(VI) in Hanford sediments, and identification of the processes responsible for the immobilization.

Task 1 was divided into Subtasks 1A and 1B. Subtask 1A evaluated the phosphate-induced immobilization of uranium in Hanford sediments and was addressed in Chapter 2. Batch experiments were designed to examine U(VI) sorption over a wide range of conditions (U(VI) and phosphate loadings). At the conclusion of batch experiments, sediments were analyzed by extended X-ray absorption fine structure (EXAFS) spectroscopy to further probe the speciation of solid-associated U(VI). Column experiments were conducted to quantify the influence of phosphate addition on U(VI) transport at environmentally-relevant

conditions. Sediments from the columns were analyzed by sequential extraction and fluorescence spectroscopy to characterize the nature of the U(VI) that had been immobilized. Equilibrium speciation calculations were performed to support the observed U(VI) species formed during reactions.

Subtask 1B focused on the impact of flow rate on uranium uptake in Hanford sediments. Chapter 3 specifically evaluates the interactions between U(VI) and sediments by modeling approaches. This subtask examined the effects of two flow rates on the transport behavior of U(VI) through sediments by developing a reactive transport model based on the one dimensional non-equilibrium convection-dispersion equation and comparing the model output with data from column experiments. Appendix A presents the development of a more advanced reactive transport model that considered complicated aqueous reactions and surface complexation reactions coupled into a mass conservation equation. It focused on interpreting not only the impact of flow rate on U(VI) transport during the uptake phase, but also combining the impact of phosphate on the U(VI) transport behavior during the release phases. This modeling effort was performed in collaboration with a research group with expertise in reactive transport modeling.

Task 2. Evaluation of the effect of water chemistry on U(VI) and Cr(VI) removal by various engineered magnetite nanoparticles and development of surface complexation modeling

Task 2 is divided into Subtask 2A and Subtask 2B, which are addressed in Chapters 4 and 5 respectively. While Chapter 4 explores interactions between U(VI)

and three negatively charged engineered nanoparticles, Chapter 5 is focused on Cr(VI) and positively charged nanoparticles. Both chapters present data from experiments that were designed to quantify the adsorption of U(VI)/Cr(VI) by various nanoparticles as a function of pH and total U(VI)/Cr(VI) concentrations. Surface complexation models were developed to simulate the surface properties of nanocomposites and to understand the binding of adsorbates to functional groups of organic compounds that are coated on the surface of inorganic solid. In Chapter 4, the impact of dissolved inorganic carbon on U(VI) adsorption was examined at three levels of concentrations and was considered in the surface complexation model. Chapter 5 evaluates nanoparticle adsorption performance for Cr(VI) simple aqueous solutions as well as with two more complex and realistic drinking water sources. With the presence of complex water sources, the stability and surface properties of nanoparticles were monitored along with the adsorption behavior of Cr(VI).

Chapter 6 summarizes the results of the present work and includes recommendations for future work.

In addition to the bench-scale research conducted for the two major tasks, understanding the fate and transport of metals are strongly related to field studies. Water and soil samples need to be collected from wide distributions to study the metal contaminations related to human activities and local development. Appendix B presents a study of the detection of heavy metal concentrations in St. Louis urban community gardens, which addressed environmental health concerns associated with community gardens. Appendix C shows how geochemical analysis can support archaeological research to address the impact of ancient metallurgical processes on

local environments. Appendix D assesses the temporal and spatial variability in metal contaminant levels among the main drinking water sources in a city in Haiti, which is meaningful in not only for environmental aspects but also with respect to human health problems.

Chapter 2. Phosphate-Induced Immobilization of Uranium in Hanford Sediment

Results of this chapter have been published in Environmental Science&Technology, **2016**, 50, (24), 13486-13494.

Graphical abstract

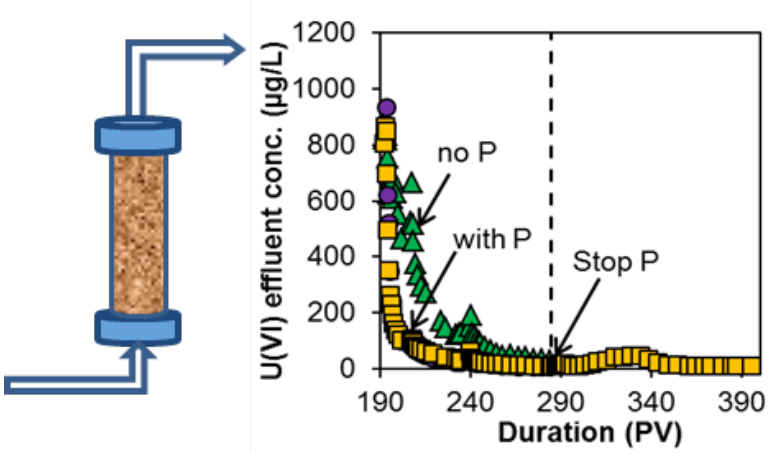

Abstract

Phosphate can be added to subsurface environments to immobilize U(VI) contamination. The efficacy of immobilization depends on the site-specific groundwater chemistry and aquifer sediment properties. Batch and column experiments were performed with sediments from the Hanford 300 Area in Washington State and artificial groundwater prepared to emulate the conditions at the site. Batch experiments revealed enhanced U(VI) sorption with increasing phosphate addition. X-ray absorption spectroscopy measurements of samples from the batch experiments found that U(VI) was predominantly adsorbed at conditions relevant to the column experiments and most field sites (low U(VI) loadings, < 25 μM), and U(VI) phosphate precipitation occurred only at high initial U(VI) (>25 μM) and phosphate loadings. While batch experiments showed the transition of U(VI) uptake from adsorption to precipitation, the column study was more directly relevant to the subsurface environment because of the high solid:water ratio in the column and the advective flow of water. In column experiments, nearly six times more U(VI) was retained in sediments when phosphate-containing groundwater was introduced to U(VI)-loaded sediments than when the groundwater did not contain phosphate. This enhanced retention persisted for at least one month after cessation of phosphate addition to the influent fluid. Sequential extractions and laser-induced fluorescence spectroscopy of sediments from the columns suggested that the retained U(VI) was primarily in adsorbed forms. These results indicate that in-situ remediation of groundwater by phosphate addition provides lasting benefit beyond the treatment period via enhanced U(VI) adsorption to sediments.

2.1 Introduction

Uranium is a contaminant of concern in subsurface environments because of past weapons production and mining processes as well as natural processes. In-situ immobilization of uranium can avoid the costs associated with pump-and-treat or excavation-based remediation strategies. In natural systems, uranium has been observed to be immobilized by the presence of uranyl phosphate minerals (Fuller et al. 2002, Jerden and Sinha 2003). The potential mechanisms responsible for uranium immobilization after phosphate addition include precipitation of low solubility uranium phosphates, enhanced adsorption to minerals originally present, and adsorption or incorporation into newly formed calcium phosphate minerals such as hydroxyapatite (Fuller et al. 2002, Mehta et al. 2016, Shi et al. 2009). Several laboratory studies have shown that uranyl phosphate phases can precipitate quickly at acidic to circumneutral pH (Kanematsu et al. 2014, Mehta et al. 2014). Adsorption of uranium to iron oxides (such as ferrihydrite and goethite) can be enhanced by the presence of phosphate through the formation of ternary surface complexes and changing surface charge (Cheng et al. 2004, Singh et al. 2012, Singh et al. 2010).

This study investigated the immobilization of uranium in sediments from the Hanford site upon phosphate treatment. At the Hanford 300 Area in Washington State, two process ponds received 58,000 kg of uranium from 1943 to 1975 (Catalano et al. 2006). The sediments have been well characterized in previous studies regarding their mineralogy, uranium species distribution, and adsorption and desorption behavior (Catalano et al. 2006, Qafoku et al. 2005, Singer et al. 2009,

Stoliker et al. 2013). Uranium in the subsurface includes both adsorbed and precipitated U(VI) species (Singer et al. 2009). The water table at this site is influenced by the stage of the nearby Columbia River, and U(VI) can be mobilized from the sediments when the water table rises during high river stages (Arai et al. 2007, Qafoku et al. 2005). Previous studies indicate kinetically controlled desorption of U(VI) from natural sediments. The extent of U(VI) adsorption to natural sediments varies depending on sediment mineralogy and the aqueous solution's inorganic carbon level, pH, and total dissolved solids (Barnett et al. 2000, Serne et al. 2002, Stoliker et al. 2011). In a field study of polyphosphate injection at the Hanford 300 Area, uranium concentrations decreased from 80 µg/L to below 30 µg/L due to either the formation of uranium phosphate minerals or adsorption to calcium phosphate (e.g., apatite) minerals (Vermeul et al. 2009). We previously studied phosphate-induced retention in sediments from the Rifle site in Colorado and found only very modest immobilization of uranium (Mehta et al. 2015). However, the effectiveness of phosphate treatment may vary greatly depending on the site-specific mineralogy and groundwater chemistry, especially the pH and carbonate concentration. Further, the fate of the U(VI) after stopping phosphate injection remains unknown and this study sought to provide insight into U(VI) transport during and after phosphate addition to induce immobilization.

The objectives of this study were to (1) identify the dominant processes responsible for phosphate-induced U(VI) immobilization and (2) quantify the extent and longevity of immobilization for sediments and groundwater of the Hanford 300 Area. While the study was performed with materials from this specific site, they are

relevant to other subsurface environments with similar mineralogy and groundwater chemistry. Batch experiments were designed to examine U(VI) sorption over a wide range of conditions, especially U(VI) loadings, and these conditions included one loading that is directly applicable to the column experiments that explored the effect of phosphate on U(VI) fate and transport in sediments. At the conclusion of batch experiments, sediments were analyzed by extended X-ray absorption fine structure (EXAFS) spectroscopy to further probe the speciation of solid-associated U(VI). Column experiments were conducted to quantify the influence of phosphate addition on U(VI) transport at environmentally-relevant conditions. Sediments from the columns were analyzed by sequential extraction and fluorescence spectroscopy to characterize the nature of the U(VI) that had been immobilized.

2.2 Materials and methods

2.2.1 Materials

Background sediments from the Hanford Formation were collected at four depths (15 to 41 ft below ground surface) of an uncontaminated portion of the Hanford 300 Area in Washington and sieved to isolate the <2 mm size fraction. Detailed characterization of sediments from this formation in previous studies has shown that the dominant minerals by mass are quartz and plagioclase feldspar, with lesser amounts of pyroxene and clays (< 5%). The minerals in the fine fraction of the sediments include smectite, vermiculite and iron oxides (Campbell et al. 2012, Stoliker et al. 2011, Stoliker et al. 2013, Zachara et al. 2013). X-ray diffraction

analysis of the sediments used in this study show that the mineral assemblages from the four different depths were similar to one another and consistent with the observations in previous studies (Figure 2.1). Consequently, 200 g of sediment from each depth were combined and physically mixed, with this composite sediment used in all experiments.

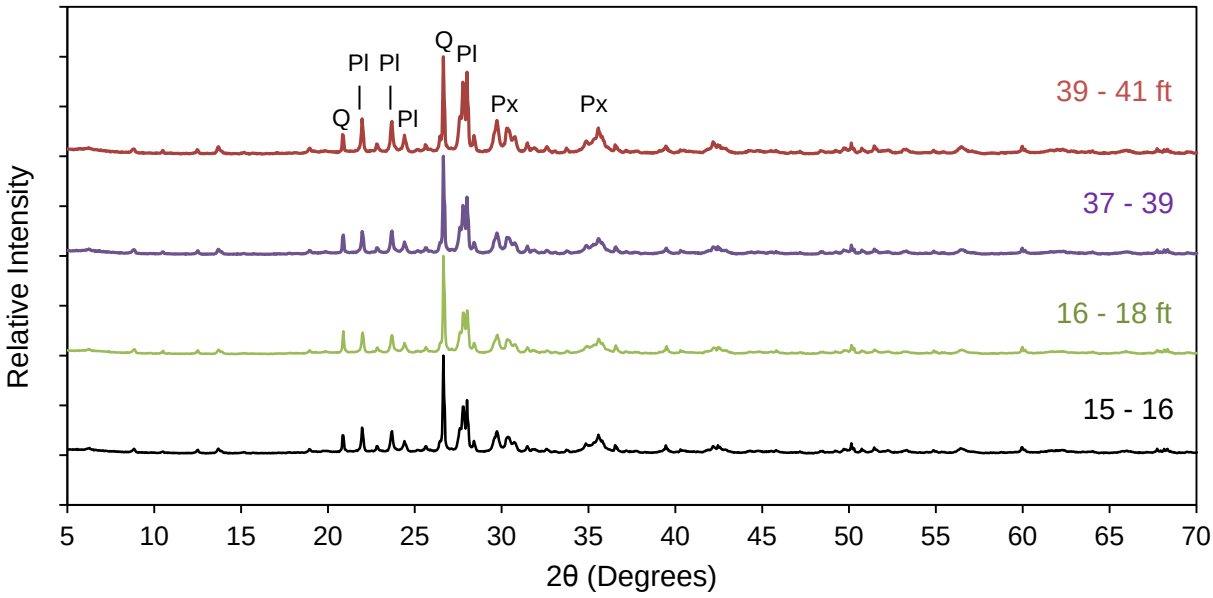

Figure 2.1. XRD spectra of Hanford sediments collected from 4 depths at the same location. The dominant mineralogy for all four depths is the same. For the major peaks, Q: quartz, Pl: plagioclase feldspar, Px: pyroxene.

Synthetic Hanford groundwater (SHGW) with a target pH of 8.05 was prepared to represent the composition of groundwater at the site (Table 2.1) (Zachara et al. 2005). Ultrapure water (resistivity > 18.2 MΩ-cm) was used. SHGW was prepared in ambient condition as oxic conditions are expected at the Hanford 300

Table 2.1. Composition of the synthetic Hanford Groundwater

Species	Conc. (mM)
Ca	1.00
Na	2.00
Mg	0.50
K	0.20
U[a]	3.5×10^{-3}/0
Li[b]	0.13
DIC[c]	1.00
SO_4	1.45
Cl	1.00
NO_3	0.50
$Si(OH)_4$	0.50
PO_4[a]	0/1.00
Br[b]	0.13
Target pH	8.05

[a] Concentration of 0 corresponds to experimental conditions with U-free or PO_4^{3-}-free influent feed

[b] Lithium (Li) and bromide (Br) were added as conservative tracers with the influent for calculation of transport parameters

[c] DIC is dissolved inorganic carbon

Area in the Hanford formation unit (the zone from which the 40 ft samples were collected), where the reported DO is around 6.95±1.21 mg/L (Vermeul et al. 2009). Bromide was added as a conservative tracer for column experiments (more description for SHGW preparation in SI Table S1). For column experiments, a 3.5 µM $UO_2(NO_3)_2$ solution was used during the uptake of U(VI) by the sediments, and 1 mM phosphate (0.85 mM $Na_2HPO_4\cdot7H_2O$ and 0.15 mM NaH_2PO_4) was used for treatment of U-loaded sediments. The synthetic groundwater was stored in impermeable plastic bags (Tedlar) to minimize gas exchange with the ambient atmosphere in order to maintain the desired pH and dissolved inorganic carbon concentration.

2.2.2 Methods

2.2.2.1 Batch Sorption Experiments

Batch experiments were performed with 250 g/L sediment suspensions in freshly prepared SHGW with the same compositions as indicated in Table 1 for column experiments with the exception of having a range of initial U(VI) and phosphate concentrations. The sediments were pre-equilibrated with SHGW for 48 hours in order to stabilize the pH and major ion composition. After separation, the supernatant was discarded and the sediments were re-suspended in fresh SHGW that also included U(VI) and phosphate. The initial U(VI) concentration ranged from 0.1 to 100 µM with phosphate concentrations of 0, 10, 100, or 1000 µM. Suspensions were shaken on an end-over-end rotator for 48 hours, after which samples were centrifuged and the supernatant was decanted and treated for chemical analysis. All the aliquots were filtered through 0.22 µm mixed cellulose ester (MCE) syringe filters (Fisher Scientific). The initial 2 mL of solution were discarded to minimize the effects of uranium adsorption onto the filter membranes. Reacted sediments for the samples with 100 µM initial uranium and 0, 100, or 1000 µM initial phosphate were loaded as wet pastes into polycarbonate sample holders, sealed with Kapton tape, and then heat-sealed in polyethylene bags for secondary containment. The samples were taken immediately to the Advanced Photon Source (APS) at Argonne National Laboratory for speciation of U by extended X-ray absorption fine structure (EXAFS) spectroscopy.

Sorption kinetics were examined with triplicate suspensions at an initial U(VI) concentration of 2.65 µM by combining 30 g of sediments with 120 mL of SHGW in polypropylene tubes (250 g/L). The U(VI) concentration was close to the influent U(VI) concentration (~3.5 µM) used in later column experiments. Aliquots (1 mL) of the suspension were taken immediately after mixing and at 0.10, 0.32, 1.0, 3.2, 10, 30, 102, 316, 960, and 2880 min and treated for chemical analysis.

2.2.2.2 EXAFS Spectroscopy Data Collection and Analysis

U L_{III}-edge EXAFS spectra were collected at room temperature on APS beamline 20-BM-B. The beamline employed a Si (111) fixed-offset, double-crystal monochromator and a toroidal focusing mirror to increase usable flux on the sample (Heald 2011, Heald et al. 1999). Fluorescence-yield data were collected using a 12-element solid-state Ge energy dispersive detector; 6 to 9 scans per sample were averaged to improve the signal to noise ratio. Energy was calibrated using a Y metal foil, setting the first inflection point in Y K-edge to 17038.0 eV. E_0 for the averaged U spectra was set to 17173.4 eV to align the EXAFS regions. Data were processed and fitted using the Athena interface to the IFEFFIT software package (Newville 2001, Ravel and Newville 2005). The spectra of the two samples to which phosphate was added were fit as linear combinations of the spectra of the phosphate-free, U(VI) reacted Hanford sediment and the uranium phosphate mineral chernikovite, taken from Singh et al (Singh et al. 2012). Reported errors in the percentages of each component are the least-squares fitting uncertainties. Chernikovite and other autunite-group minerals have similar sheet structures (Locock et al. 2004a, Locock et

al. 2004b, Morosin 1978). With the identical sheet structure and the very limited effect of the specific cations present between the sheets on the coordination environments of the uranium atoms, the autunite-group minerals have similar U EXAFS spectra (Catalano and Brown 2004).

2.2.2.3 Column Experiments and sequential Extractions

Four glass columns (2.5 cm diameter, 15 cm length) were packed with sediments in ~ 1 cm increments of sediments followed by DI water wetting. Porous plates (20 µm pore size) at the top and bottom of columns distributed the flow and prevented movement of particles. The porosity was 0.29-0.30, which corresponds to a solid:water ratio of around 7,000 g/L inside the columns (Table 2.2). Bromide was added to the column influent at a concentration of 1.25×10^{-4} M to be used as a conservative tracer. The groundwater was pumped into the columns in an upflow mode at flow rates of ~8.0 mL/h (varied from 7.7 to 8.3 mL/h, adjusted by the peristaltic pump), corresponding to pore water velocities of ~1.3 m/d, which is within the typical range for groundwater, although higher velocities (*e.g.* 10 m/d) may occur at the Hanford 300 area due to large hydraulic gradients (Qafoku et al. 2005, Vermeul et al. **2009**).

Table 2.2. Physical Properties of Packed Columns.

	Col-U	Col-U-NP	Col-U-P	Col-U-P-NP
Sediment (g)	145	145	160	142
Water (mL)[a]	22	22	21	22
Porosity	0.29	0.30	0.30	0.30
Flow rate (mL/h)[b]	8.0±0.1	8.0±0.1	8.0±0.1	8.0±0.1
Pore water velocity (cm/d)	137	131	131	131
Residence time (hr)	2.63	2.75	2.75	2.75

[a] Water used to saturate columns
[b] The average flow rate was measured from experiment. Water flux, pore water velocity and residence time were calculated based on the flow rate, porosity and volume of columns.

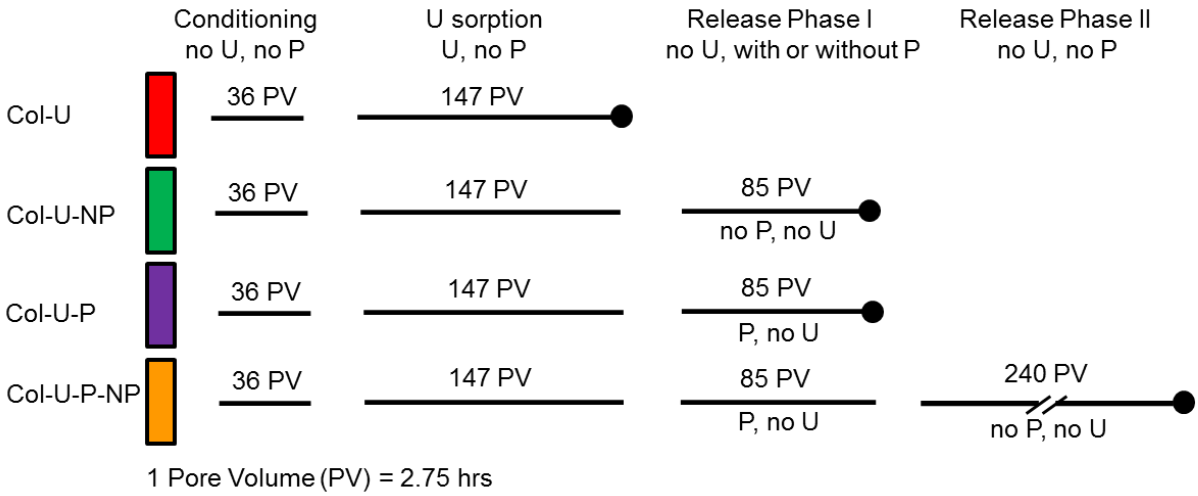

Figure 2.2. Operation phases for four columns. Each phase corresponds to an influent composition. The flow rate was such that one pore volume (22 mL) is equivalent to 2.75 h. Black circles mark the end of the operation for each column.

Columns were operated in a series of phases. A conditioning phase was performed in order to remove background or labile U(VI) from the sediment. Then U(VI)-containing SHGW was pumped into columns during an uptake phase. After loading the sediments in the uptake phase, U(VI)-free SHGW was introduced to

flush U(VI) out of columns either with phosphate (Col-U-P) or without phosphate (Col-U-NP) in Release Phase I. Finally, for one of the columns that had received phosphate, phosphate was removed from the influent during Release Phase II and operated for another month (Col-U-P-NP) (Figure 2.2). Effluent samples were collected every 1.5 h (~0.54 pore volume) by a fraction collector (Spectrum/Chrom CF-1). Several stopped-flow events with 12 hour durations (4.4 PV) were applied to evaluate the extent to which the sediments were in local equilibrium with the pore water.

At the conclusion of each column experiment, sediments were removed and divided into inlet, middle and outlet sections (roughly 5 cm each). Extractions were performed in duplicate on 2 g sub-samples collected from each section and contacted with 50 mL of each extractant. The five-step sequential extraction method was modified from the original method of Tessier (Table 2.3) (Tessier et al. 1979). Extractant was discarded before adding the extractant for next step's extraction. A one-step digestion was also performed to directly measure the total uranium in the sediments by contacting the sediments with strong nitric acid and hydrochloric acid (Campbell et al. 2012). Background concentrations were determined from extractions of sediments collected from a column that had gone through a conditioning phase identical to that used for the four experimental columns. For sediments from all columns, the extracted U(VI) from one-step acid digestion corresponded well with the total U(VI) from sequential extraction (within 15%).

In order to assess the rate of extraction, a time-dependent sequential extraction was conducted with ammonium acetate (extractant in step 2) and then

acetic acid (extractant in step 3). Duplicate samples (8 g each) from each section were mixed with 200 mL of extraction solution. Aliquots of the suspension (1 mL) were collected at 0.10, 0.32, 1.0, 3.2, 10, 30, 60, 100, 316 and 960 min and treated for chemical analysis.

Table 2.3. Steps in sequential extraction

Step	Target	Extract composition	pH	Time
1	Water soluble	Ultrapure water	5.5	16 h
2	Exchangeable	1 M ammonium acetate	7.0	16 h
3	Carbonate	1 M acetic acid/sodium acetate	5.0	16 h
4	Amorphous oxides	0.12 M ammonium oxalate 0.11 M oxalic acid	3.0	4 h
5	Residual	Concentrated 8 mL HNO_3 and 2 mL HCl at 100˚C	--	4 h

2.2.2.4 Chemical Analysis of Aqueous Samples

After filtration, all the aliquots were acidified to 1% HNO_3. Concentrations of dissolved U, Ca, Na, Mg, K and Si were measured using inductively coupled plasma-mass spectrometry (ICP-MS, PerkinElmer). Phosphate concentrations were determined by the ascorbic acid method (Clesceri et al. 1999). Influent and effluent samples from column experiments were measured for pH, dissolved oxygen (DO) and dissolved inorganic carbon (DIC). The measurements and results for pH and DO are included in the SI. DIC was measured using the inorganic carbon mode on a TOC analyzer (Shimadzu, TOC-$L_{CPH/CPN}$ PC-controlled model). Bromide was measured by an ion selective electrode (Cole-Parmer).

2.2.2.5 Laser Induced Fluorescence Spectroscopy (LIFS) Analysis

Sediment samples from inlet, middle, and outlet sections of the columns were loaded into 2 mm × 4 mm × 25 mm quartz cuvettes for analysis. Detailed procedures for LIFS analysis have been described elsewhere (Wang et al. 2005, Wang et al. 2004). The cuvettes were attached to the sample holder of a CRYO Industries RC152 cryostat where the sample was exposed to vaporized liquid helium. Samples were excited at 415 nm with a Spectra-Physics Nd:YAG laser pumped MOPO-730 laser. The emitted light was collected at 85°C to the excitation beam, focused into the entrance slit of an Acton SpectroPro 300i double monochromator spectrograph and detected by a Princeton Instruments PIMAX intensified CCD camera. The spectra were analyzed using the commercial software package IGOR.

2.3 Results and Discussion

2.3.1 Batch Sorption Experiments

U(VI) adsorption was enhanced by phosphate addition (Figure 2.3). Fitting of linear adsorption isotherms to the data resulted in K_d values of 0.8, 0.9, 2.0 and 53.8 mL/g when phosphate concentrations increased from 0 to 10, 100 and 1000 µM. The K_d value with

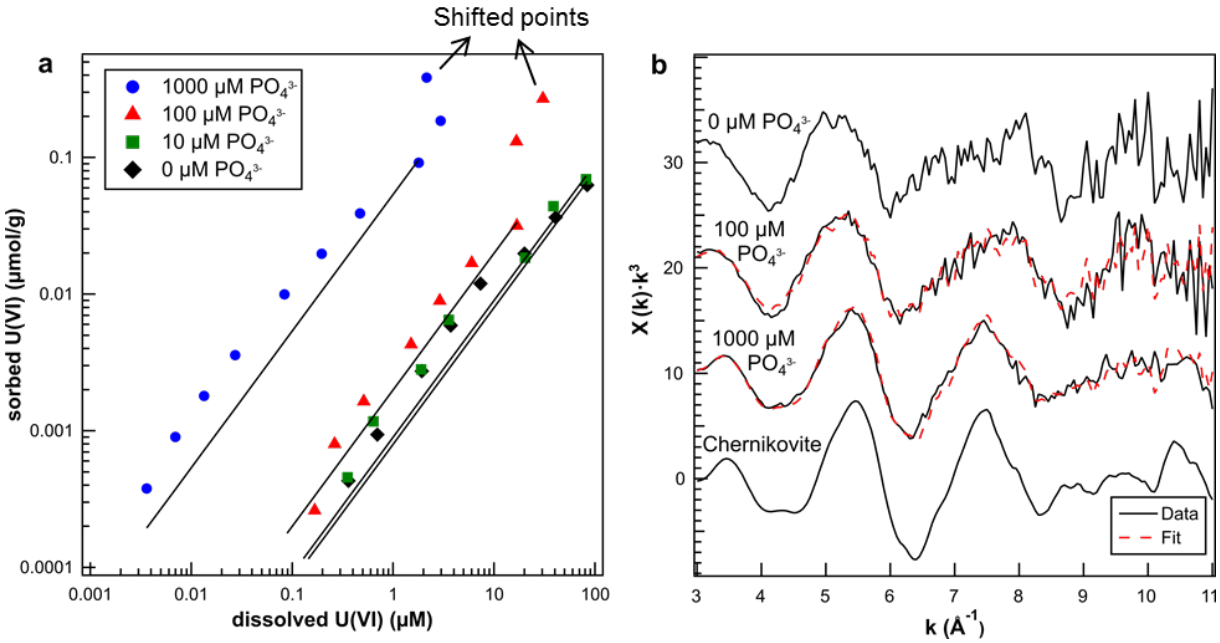

Figure 2.3. (a). Equilibrium sorption experiments (2 days) with Hanford sediments at initial [U(VI)] from 0.1 to 100 µM and 0, 10, 100 or 1000 µM P. Experiments were conducted with SHGW at pH ~ 8.05 at a solid:solution ratio of 250 g/L. Adsorption isotherms were plotted with data for conditions for which precipitation was not anticipated to occur; several high concentrations points for the 100 and 1000 µM PO_4^{3-} are not included. The lines indicate the fit of the data to a linear adsorption isotherm model, and the corresponding K_d values are 0.8, 0.9, 2.0 and 53.8 mL/g. Two points with arrows indicate shifted points that were characterized by EXAFS. (b). Uranium L_{III}-edge EXAFS spectra of Hanford sediments from batch equilibrium experiments containing the highest uranium loading (initial U(VI) concentration of 100 µM) for each PO_4^{3-} condition. The spectra with 100 and 1000 µM PO_4^{3-} were fit as linear combinations of the spectra of the Hanford sediment from the experiment with no added PO_4^{3-} and chernikovite.

no phosphate was comparable to that from a previous study (0.8 ~ 1 mL/g) with similar sediments and groundwater (Stoliker et al. 2011). Phosphate addition had a greater enhancement of U(VI) sorption to the Hanford sediments than to Rifle sediments examined in a previous study, where K_d values were 0.4, 0.6 and 2.2 for 0, 100 and 1000 µM phosphate addition (Mehta et al. 2015). The lower K_d values for

the Rifle sediments resulted from the presence of higher Ca (5 mM) and dissolved inorganic carbon (7.44 mM) in the groundwater, which promoted the formation of soluble uranyl-calcium-carbonate species that decrease the extent of U(VI) retention (Mehta et al. 2014, Stewart et al. 2010).

With low U(VI) loadings (<10 µM, ~3.5 µM was used in column study), increased sorption caused by phosphate could be due to the formation of inner-sphere U(VI)-phosphate ternary surface complexes or adsorption to newly formed Ca-phosphate solids (Fuller et al. 2002, Mehta et al. 2014, Shi et al. 2009). Based on saturation index (Table 2.4) calculations, no precipitation would have been expected with initial U(VI) loading in the low concentration range, and the increased U(VI) uptake was because phosphate enhanced adsorption of U(VI) to the solid phases. The condition used in the column experiments is most similar to that of one of the low U loading conditions used here and is most similar to what would occur at field sites. For higher U(VI) loadings (≥ 25 µM, much higher than experienced in columns), with increasing phosphate concentration, U(VI) uptake in the solids transitioned from adsorption to precipitation. The addition of 100 µM and 1000 µM phosphate led to final solution compositions that are supersaturated with respect to autunite ($Ca(UO_2)_2(PO_4)_2 \cdot 3H_2O$) (Table 2.4). The EXAFS spectra of samples at the highest uranium and phosphate loadings displayed spectra features intermediate between those of U(VI) adsorbed to the sediments in the absence of phosphate and autunite-type U(VI) phosphate minerals (Figure 2.3). These samples correspond to the two shifted points (pointed out by arrows) in the isotherm plots (Figure 2.3a) that are suggestive of precipitation. Linear-combination fitting of the spectra show that

the 100 µM phosphate sample contained 60 ± 4% adsorbed and 40 ± 6% precipitated U(VI) and the 1000 µM phosphate sample contained 22 ± 2% adsorbed and 78 ± 5% precipitated U(VI) (Figure 2.3b). The distribution of U(VI) between adsorbed and precipitated forms has been observed previously for U(VI) adsorption to the smectite clay mineral montmorillonite in the presence of phosphate at a similar water chemistry (Troyer et al. 2016).

Table 2.4. Saturation indices of (SI) of autunite and schoepite for final aqueous solution of batch experiments

SI	Phosphate Initial Addition					
	10 µM		100 µM		1000 µM	
Initial U(VI) (µM)	Autunite	Schoepite	Autunite	Schoepite	Autunite	Schoepite
0.10	-	-	-3.95	-4.47	-4.46	-5.84
0.23	-5.31	-4.06	-3.40	-4.19	-3.87	-5.56
0.46	-4.95	-3.88	-3.04	-4.01	-3.31	-5.27
0.92	-4.43	-3.62	-2.45	-3.72	-2.75	-4.97
2.57	-3.46	-3.14	-1.53	-3.24	-1.71	-4.47
5.13	-2.90	-2.86	-0.96	-2.95	-0.97	-4.10
10.22	-	-	-0.28	-2.62	-0.21	-3.72
24.72	-1.29	-2.01	**0.72**	-2.11	**0.90**	-3.14
49.31	-0.56	-1.63	**0.40**	-2.12	**1.35**	-2.91
98.14	**0.58**	-1.05	**0.35**	-1.78	**0.86**	-3.06

'-' value not determined

2.3.2 Column Experiments

2.3.2.1 Uranium uptake in the absence of phosphate

The profiles of the column effluent concentrations provide information on U(VI) adsorption and its subsequent desorption in the presence and absence of phosphate (Figure 3). During the conditioning phase, the labile portion of U(VI) in the initial sediments was eluted from the columns. After running 36 pore volumes (PVs) of SHGW through the columns, the effluent concentrations had decreased to below 5 µg/L. However, the effluent U(VI) concentration for Col-U-P was still around 70 µg/L which was hypothesized to be caused by higher initial background U(VI) in the sediments of that particular column. During the uptake phase, the effluent U(VI) concentrations for all columns started out low as uranium was adsorbed to the sediments and then approached the influent U(VI) concentration after loading U(VI) for 147 PV. The reason that the measured effluent concentrations do not match the influent concentrations after longer pore volumes in this uptake phase is probably because a portion of the effluent U(VI) precipitated in the outlet fitting or tubing that was downstream of the sediments in the column. At around 102 PV, the U(VI) effluent concentration began decreasing, which was probably caused by U(VI) precipitation in the outlet tubing sections. Such an accumulation is a limitation of these experiments, and the accumulation was confirmed by the release of uranium when the outlet fittings and tubing sections were contacted with strong acid (Table 2). The accumulation probably occurred because the pressure of CO_2 dropped to atmosphere levels at the outlet, and this degassing lowered DIC and thus U(VI) solubility. In order to confirm that with less impact from tubing issues the U(VI) uptake profiles would have been similar and sediments in columns after the uptake phase should have very similar total amounts of U(VI), two additional columns with

the same uptake phase operation were considered and mass balance calculations were performed for those columns (Chapter 3).

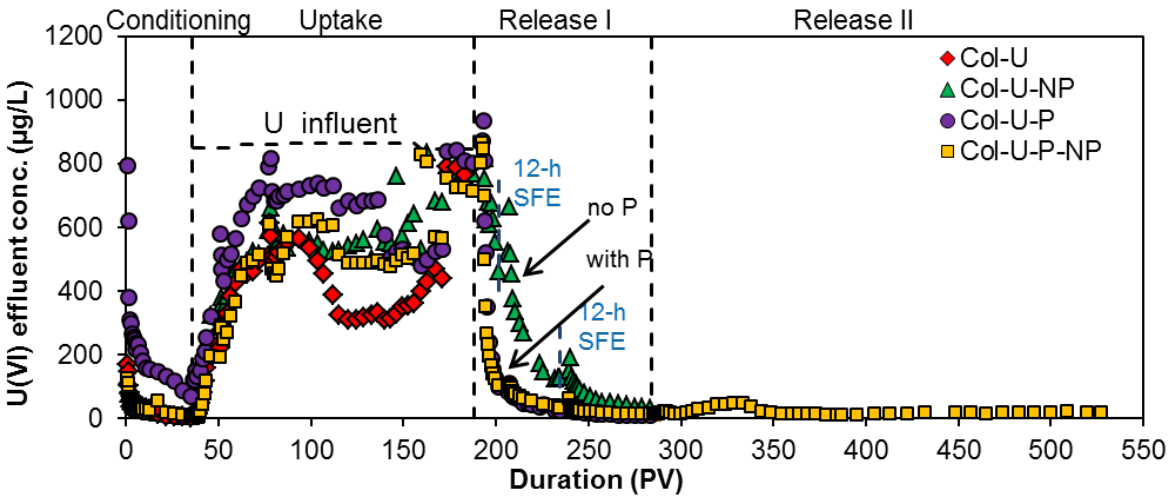

Figure 2.4. Uranium profiles for four columns with different operation phases. Col-U: conditioning phase, uptake phase; Col-U-NP: conditioning phase, uptake phase and release phase I without P; Col-U-P: conditioning phase, uptake phase and release phase I with P; Col-U-P-NP: conditioning phase, uptake phase, release phase I with P and release phase II with P removed. During the uptake phase, the decrease and the low effluent U(VI) concentration from 102 to 171 PV was because part of the effluent U(VI) was lost before being collected (accumulated in the outlet tubing). After replacing new tubing, the U(VI) concentration was closer to the influent concentration.

2.3.2.2 Uranium release in the absence/presence of phosphate

Phosphate enhanced the retention of U(VI) by sediments during the U(VI) release phase. The effluent U(VI) decreased faster for the columns that contained phosphate in the influent (Col-U-P and Col-U-P-NP) than for the one that did not (Col-U-NP). Slower U(VI) release in the presence of phosphate was also observed in a previous

study in which sediments were first equilibrated with phosphate-containing solutions in batch reactors and then placed into columns for desorption (Shi et al. 2009). Phosphate also helped retain U(VI) in columns loaded with Rifle sediments, but the extent of retention was much smaller than that observed for the Hanford sediments (Mehta et al. 2015). Stopped-flow events led to a significant increase of U(VI) concentration in columns without phosphate, which is consistent with observations in previous studies explained by slow release of U(VI) from intra-particle domains (Liu et al. 2009a, Qafoku et al. 2005). When phosphate was present the extent of the increase in U(VI) concentration during the stopped-flow event was much smaller, demonstrating that phosphate enhanced the strength of U(VI) binding to the sediments and also slowed the rate of U(VI) release.

After phosphate treatment, U(VI) was not easily released even when phosphate was no longer present in the influent. When phosphate was removed from the SHGW for Col-U-P-NP, the effluent U(VI) concentration increased slightly to 45 µg/L at around 327 PV before dropping back to 15 µg/L at 349 PV and staying at concentrations lower than the drinking water standard of 30 µg/L for the duration of the experiment. The temporary increase in effluent U(VI) concentrations that occurred following the removal of phosphate from the influent may be associated with mobilization of the most labile U(VI) species adsorbed to the exterior of sediment grains.

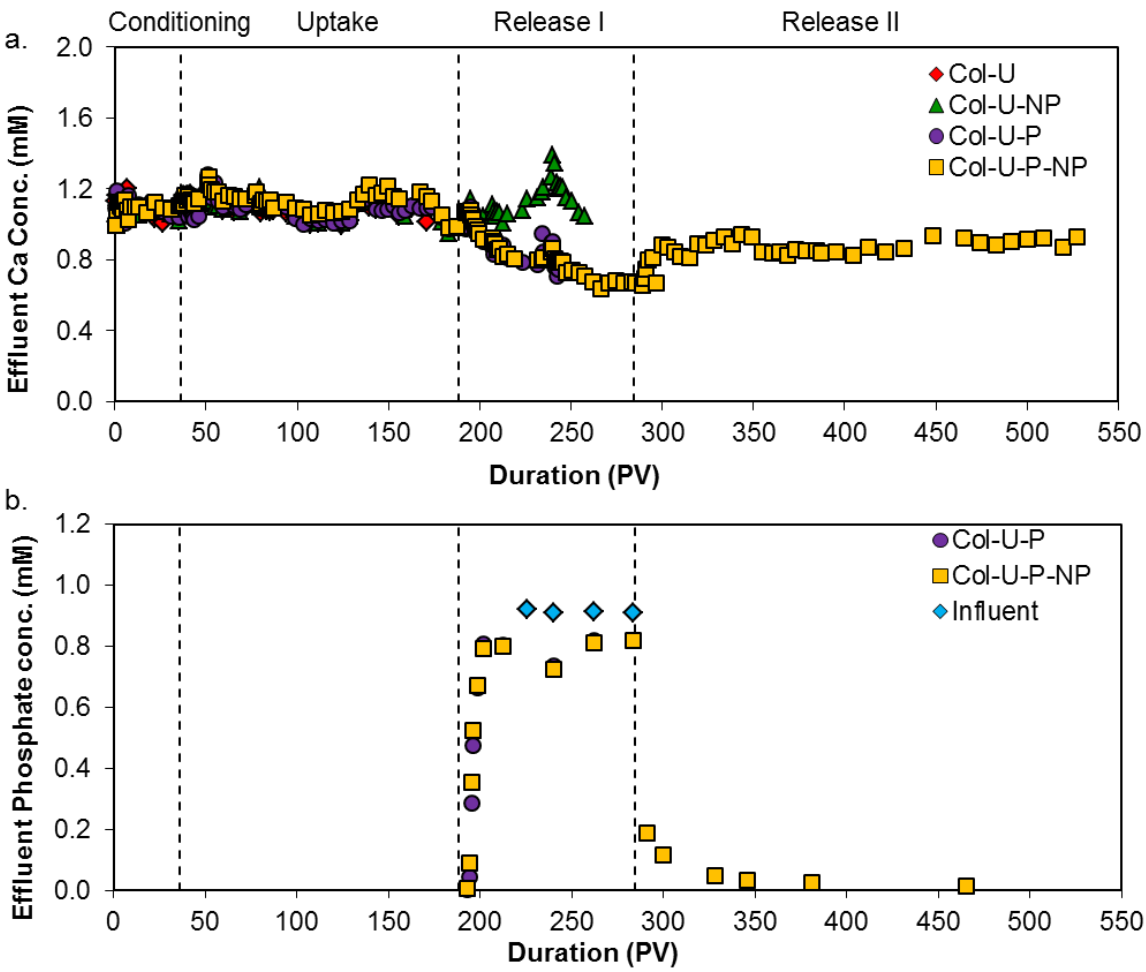

Figure 2.5. (a) Calcium profiles for four columns. The target influent calcium concentration was 1.0 mM. (b) Phosphate effluent concentrations in Col-U-P and Col-U-P-NP and four influent phosphate measurements.

U(VI) phosphates probably did not precipitate in the columns. Saturation index calculations were carried out based on measured elemental concentrations in the effluents to examine the likelihood of U(VI) phosphate precipitation inside the columns. For U(VI) species, the effluents were only supersaturated with respect to autunite with saturation index ranges from 0 to 0.2 for the first 20 PV of Release Phase I when phosphate containing influents were introduced, and the saturation

index then decreased to less than 0 at larger PVs (Table 2.5). Calculations for the effluents indicated that solutions were supersaturated with respect to the calcium phosphates hydroxyapatite ($Ca_5(PO_4)_3OH$) and octacalcium phosphate ($Ca(PO_4)_{0.74}H_{0.22}$), which is a potential precursor to hydroxyapatite (Table 2.5). The calcium in the effluent decreased when phosphate was introduced to the column (Figure 2.5), and phosphate effluent concentrations only reached 0.81 mM and were lower than the influent concentration (~0.90 mM) during the operation period. The difference between influent and effluent concentrations of Ca and P would be consistent with the formation of a calcium phosphate solid with a Ca:P molar ratio of 1.33, which is very close to the ratio of 1.35 in octacalcium phosphate (Mehta et al. 2016). U(VI) adsorption to newly formed calcium phosphate minerals probably contributes to the enhanced retention of U(VI) in the sediments upon phosphate addition. Immobilization of U(VI) by adsorption to calcium phosphate solids is consistent with the findings of our recent batch study in which newly formed calcium phosphate solids led to U(VI) removal by adsorption at pH 7.5 (Mehta et al. 2016).

Table 2.5. Saturation indices (SI) of potential U(VI) and Ca precipitates for effluent samples from Col-U-P and Col-U-P-NP

Phase	Column	Time (PV)	Sch-oepite	Chernik-ovite	Au-tunite	Ruther-fordine	Na-autunite	Uranyl ortho-phosphate	Hydroxy-apatite	Calcite	Octacalcium phosphate
I	Col-U-P	196	-3.38	-5.03	**0.26**	-5.22	-2.81	-10.3	**13.3**	**0.05**	**2.42**
		240	-4.26	-5.71	-1.14	-6.09	-3.68	-12.5	**13.6**	-0.00	**2.52**
	Col-U-P-NP	196	-3.5	-5.11	**0.13**	-5.34	-2.87	-10.6	**13.5**	**0.06**	**2.47**
		240	-4.07	-5.51	-0.75	-5.90	-3.31	-11.9	**13.6**	-0.02	**2.51**
II	Col-U-P-NP	294	-4.31	-6.34	-2.47	-6.14	-5.32	-13.8	**11.6**	-0.07	**2.02**
		465	-4.59	-8.92	-7.54	-6.42	-10.8	-19.3	**5.17**	**0.03**	**0.42**

2.3.2.3 Sequential extractions

The sequential extraction results confirmed the finding that phosphate enhanced the retention of U(VI) (Figure 2.6). The distribution of extracted U(VI) in the different sections (inlet, middle, and outlet) was quite uniform for Col-U-P and Col-U-P-NP. After the conditioning phase, around 1.5 μg U(VI)/g could still be extracted from the sediments, and this recalcitrant uranium baseline would be present in all the sediments from the columns (Table 2.6). Most U(VI) fractions from Col-U were extracted as labile forms in steps 2 and step 3, showing that the majority of U(VI) accumulated as ion exchangeable and weak-acid extractable forms.

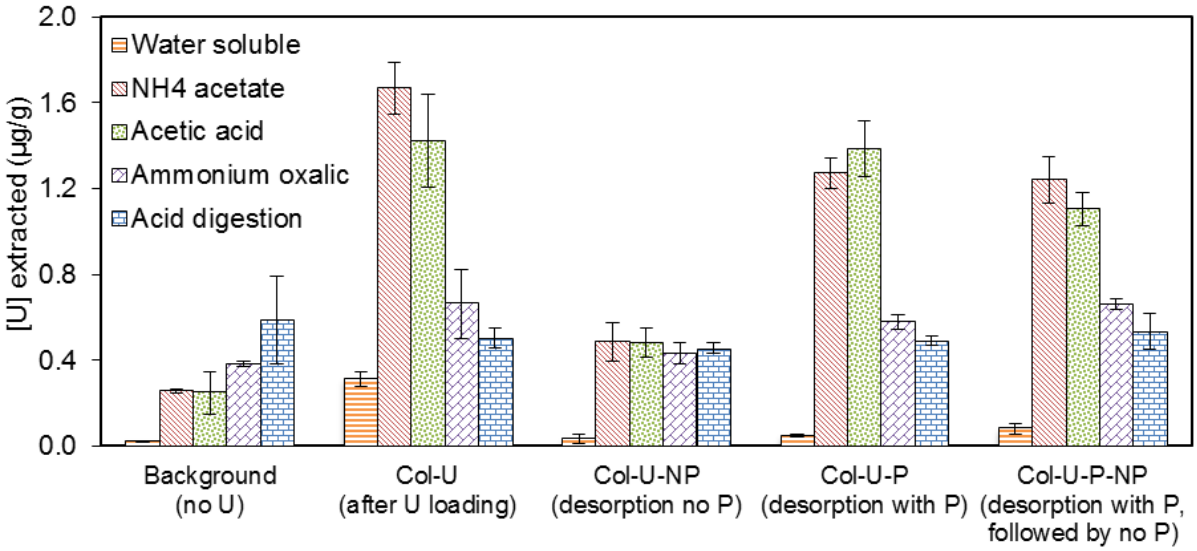

Figure 2.6. Sequential extraction results of extracted U(VI) from column sediments and background sediments. Error bars represent standard errors for the data obtained from samples for each column. The extracted U(VI) for each column is reported as the average amount from three sections.

When U(VI)-free groundwater with no phosphate was introduced to Col-U-NP, 87% of the U(VI) that had accumulated during the uptake phase was washed out of the column. In contrast, when U(VI)-free groundwater with phosphate was introduced to Col-U-P, 26% of the U(VI) that had accumulated during the uptake phase was washed out. Extracted U(VI) in the water soluble form became negligible and a small amount of U(VI) in ion exchangeable forms was lost compared to Col-U. Most retained U(VI) was extracted in steps 2 and 3, which are the same steps in which uranium was extracted from the U-loaded sediments before phosphate treatment (Col-U). The accumulation of U(VI) in ion-exchangeable and weak acid extractable forms is consistent with the U(VI) being present as adsorbed species rather than low solubility U(VI) phosphate precipitates. After stopping phosphate addition in Col-U-P-NP, there was an insignificant decrease in the amount of U(VI) (0.15±0.58 µg/g) from ion exchangeable and weak acid extractable fractions compared to Col-U-P, indicating a lasting impact of phosphate addition. Sequential extractions in a previous study with Rifle sediments showed that only 55% of U(VI) was retained in the column due to the addition of phosphate,(Mehta et al. 2015) but as mentioned earlier the conditions at the site are less favorable for phosphate-induced U(VI) immobilization.

2.3.2.4 LIFS determination of likely U(VI) species present

LIFS spectra of samples from Col-U, Col-U-P and Col-U-P-NP provide further evidence for adsorption as the dominant immobilization process in the columns (Figure 2.7). The U concentrations in the column sediments were too low for EXAFS

analysis. Most LIFS spectra were very similar with bands at ~512 and 534 nm and a weaker band at ~562 nm appearing in spectra for Col-U (all three sections), Col-U-P (inlet and mid sections) and Col-U-P-NP (inlet and mid sections) (Figure 5 a-e, g-h). All spectra are very different from recently reported ones for samples that had U(VI) precipitated as Na-autunite (Figure 5k) in a calcium and phosphate solution (504.0, 526.5 and 550.0 nm) or other crystalline uranyl-phosphate mineral phases which display intense, well-resolved spectra with the first vibronic band appearing between 499.4 nm and 503.8 nm (Wang et al. 2008). Instead, the spectra closely resemble those previously reported U(VI) adsorbed to Hanford 300 area sediments with bands at 498.6, 519.7, 542.1 and 564.5 nm (Figure 5j) (Mehta et al. 2016)'(Wang et al. 2011b). The similarity among the spectra for the different samples from the columns indicates that the differences in U(VI) speciation responsible for the enhanced retention of U(VI) from phosphate addition are subtle and that the general structure of the adsorbed species remains similar. Minor spectral differences such as the better resolved bands at 498, 518, 542 and 565 nm for the outlet section of Col-U-P (Figure 2.7 f) and the poorly resolved spectra of the outlet section of Col-U-P-NP (Figure 2.7 i) likely reflect the heterogeneous nature of the sediments. The broad spectra for all the samples compared to the reference samples were due to the relatively low U(VI) loading in our samples.

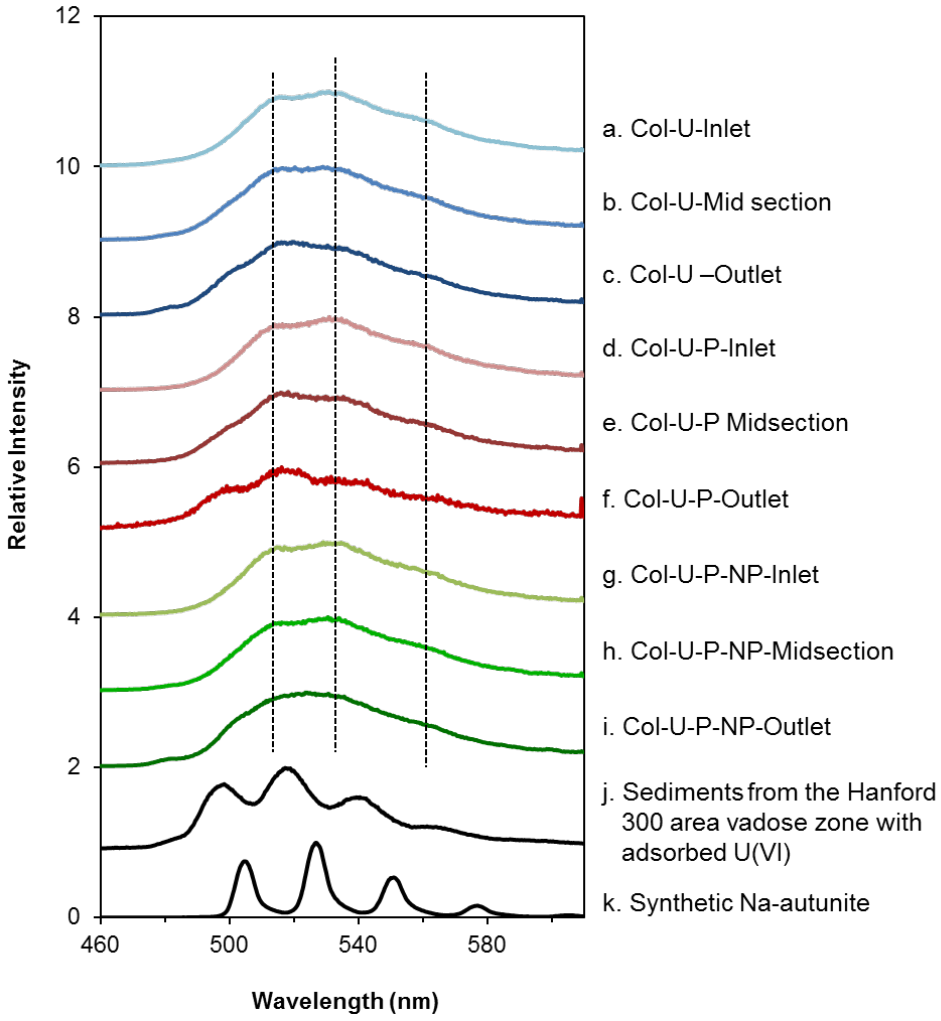

Figure 2.7. Fluorescence spectra of U(VI) sorbed on Hanford sediments from different depths in column experiments and the prepared reference U-species. All spectra were normalized to the same maximum intensity.

2.3.3 Comparison between mass balance calculations and sequential extractions

Mass balance calculations were performed based on the difference between the influent and effluent U(VI) concentration to obtain accumulated and released U(VI) amounts (Equation 2.1).

$$U_{mass}\ uptaken\ \left(\frac{\mu g}{g}\right) = \frac{\sum[(C_{in} - C_{out}) * Q * t]}{m_{sed}} \qquad \text{(Equation 2.1)}$$

where C_{in} and C_{out} represent U(VI) concentrations in the influent and effluent (µg/L), Q is the flow rate (L/h), and t is the time duration between the collection of each effluent sample (h), m_{sed} represents the mass of sediments loaded in each column (g).

For the column study, several problems came up during the operation. During the conditioning phase, higher U(VI) effluent concentrations were observed for one of the columns (Col-U-P). This may have been due to those sediments possibly containing more U(VI) than those used in other columns, despite efforts to homogenize the sediments before loading them into the columns. Although 70 ug/L was high compared to the effluent of the other three columns, it was relatively low compared to the influent concentration during the uptake phase.

During the uptake phase, the long term operation and the drop of CO_2 pressure to atmosphere levels at the outlet led to the precipitation of U(VI) in outlet sections of tubing. In order to consider this portion of U(VI) in the mass balance calculation, strong HNO_3 was added into the tubings to wash the precipitates out, and the concentrations in those known volumes of acid were then measured. The calculated masses of U in the tubing sections were added together and then considered as ones to be excluded from the calculated amount of U(VI) that had been taken up in the sediments based on the influent and effluent concentrations (Table 2.6).

Table 2.6. Released and accumulated amounts of U(VI) from mass balance calculations applied to the U(VI) profile in Figure 3.

	µg U(VI)/g sediments	Col-U	Col-U-NP	Col-U-P	Col-U-P-NP
	Conditioning	0.13	0.11	0.8	0.16
Uptake	U(VI) uptake (Influents - Effluents)*	9.28	6.55	4.63	7.57
	U(VI) precipitated in tubing sections	3.30	1.13	1.25	1.68
	Calculated U(VI) accumulated in sediments*	5.98	5.42	3.38	5.89
Release	Release I	-	2.25	0.71	0.79
	U(VI) precipitated in tubing sections (Release I)	-	0.14	0.05	0.07
	Release II	-	-	-	0.69
	Calculated U(VI) release from columns	-	2.39	0.76	1.55

*: The mass balance calculation for the third row 'U(VI) uptake (Influents – Effluents)' still have high uncertainty (as the tubings were not replaced in time) that also leads to high uncertainty in the row 'Calculated U(VI) accumulated in sediments'.

Table 2.7. Total U(VI) extracted from the sediments after column experiments.

Mass of U(VI) (µg/g)	BG	Col-U	Col-U-NP	Col-U-P	Col-U-P-NP
Sequential Extraction	1.50±0.30	4.57±0.58	1.89±0.24	3.77±0.26	3.62±0.32

After changing the tubing at 171 PV, U(VI) concentrations increased and approached the influent concentration as expected. In Table 2.6, uncertainty still existed in the number for uptake of U(VI) as the tubings issue was observed after significant decrease of U(VI) effluent concentration was observed and because one set of earlier tubing sections was no longer available to be digested. Fortunately, for the two release phases studied, the tubings were changed frequently and the acidification of the tubings showed only small amounts of U in them (Table 2.6), thus interactions with the outlet tubings would not significantly influence the release profile.

For the comparison between sequential extraction with the mass balance calculation, the extracted U(VI) from background sediments should be considered as the part of U(VI) that could not be removed in the column system, thus it was not included in mass balance calculation. For the first four columns, because of the uncertainty that existed in the uptake amount of U(VI), the comparison between the net accumulation from mass balance calculations and sequential extraction was not ideal. Otherwise, most columns had good agreements between the masses of uranium in the sediments determined by sequential extraction and from influent/effluent information from several aspects. From mass balance calculation, 0.76 µg/g (0.71+0.05) of U(VI) was released from Col-U-P during the Release Phase I, while the difference between Col-U and Col-U-P in the sequential extraction was 0.80±0.84 µg/g (Table 2.7). From mass balance calculation, 2.39 µg/g of U(VI) was released from Col-U-NP during the Release Phase I, while the difference between Col-U and Col-U-NP in the sequential extraction was 2.68±0.82 ug/g.

2.4 Implications for Uranium Transport in Subsurface Systems

The study demonstrated the influence of phosphate on U(VI) transport in environmentally relevant sediments. Batch experiments confirmed that both adsorption and precipitation could contribute to U(VI) retention depending on the exact uranium and phosphate concentrations present. The specific concentrations in the column study as well as the high solid:water ratio in the column and occurrence

of advective flow make the results of the column most directly relevant to subsurface environments. Once phosphate is introduced, sorbed U(VI) would be harder to mobilize, which could largely limit the desorption of U(VI) during advective flow and hence decrease the downgradient U(VI) concentrations. Retention of U(VI) following phosphate addition to the Hanford sediments was shown to be due to enhanced adsorption of U(VI) species, including U(VI) adsorption to freshly formed calcium phosphate minerals, instead of formation of U(VI)-phosphate precipitates. The treatment efficiency will depend on the specific subsurface geochemical conditions of contaminated sites. Phosphate addition can be more effective for sites such as the Hanford site (i.e. as opposed to the Rifle site) that have lower dissolved inorganic carbon concentrations. Although not studied here, the pH of the groundwater would play an important role in affecting U(VI) immobilization. At lower pH, various processes would change. First, U(VI) would mainly exists as U(VI)-hydroxide species instead of U(VI)-carbonate species, which affects U(VI) mobility. If carbonate remains the same, then adsorption of U(VI) to sediments decreases when pH is lower than 4 ~5 because of the protonation of the mineral surfaces. The pH would also affect the mechanisms for U(VI) immobilization. It has been reported that U(VI) can precipitate as autunite at low pH (4,6) but will primarily be adsorbed to or incorporated into calcium phosphate solids under similar experiment conditions.(Mehta et al. 2016) After introducing phosphate for a while, the effect on retention could last for a long duration without addition of phosphate, which can limit the costs and possible environmental impacts (e.g., eutrophication) that would be associated with larger and longer additions of phosphate. As slow

U(VI) desorption from sediments may occur after ending phosphate addition, U(VI) release can be slowed and the released concentration may be controlled effectively by optimizing the timing and doses of phosphate addition.

Acknowledgements

This work was supported by the U.S. Department of Energy (DOE) Subsurface Biogeochemical Research program (No. DE-SC0006857). ICP-MS analysis was performed at the Nano Research Facility (NRF) at Washington University. The fluorescence spectroscopy measurements were performed at the Environmental Molecular Sciences Laboratory (EMSL), a national scientific user facility sponsored by the U.S. Department of Energy's Office of Biological and Environmental Research and located at the Pacific Northwest National Laboratory, operated for the Department of Energy by Battelle. EXAFS spectra were collected at the Advanced Photon Source, a U.S. Department of Energy (DOE) Office of Science User Facility operated for the DOE Office of Science by Argonne National Laboratory under Contract No. DE-AC02-06CH11357. Sediments were provided by Dr. John Zachara from Pacific Northwest National Laboratory. We appreciate the comments of Associate Editor David Waite and three anonymous reviewers that helped us improve the presentation and interpretation of our study.

Chapter 3. Modeling Uranium uptake in Hanford sediments and the impact of flow rate

3.1 Introduction

Phosphate addition resulted in enhanced retardation of U(VI) transport through columns loaded with Hanford sediments as discussed in Chapter 2. Both batch and column studies showed enhanced U(VI) adsorption to Hanford sediments. The stopped flow event discussed in Chapter 2 has demonstrated the non-equilibrium U(VI) adsorption process. However, the behavior has not been interpreted with modeling approaches.

Recharge and discharge of U(VI) of the vadose zone occur with the seasonal fluctuation of groundwater. One field-scale uranium transport study reveals that multirate sorption/desorption, surface complexation reactions are important to determine U(VI) migration in the field. One Stoliker's study reveals that adsorption of uranium on Hanford sediments varies with changing water chemistry (Stoliker et al. 2011). A generalized composite surface complexation modeling has been applied for the adsorption to complex compositions of sediments, considering hydrogen ion and carbonate concentrations. The results showed that for specific aqueous

composition, single-reaction one-site (sites with the same binding strength) could approximate the adsorption process.

In the field site, it is possible that the time scale of adsorption could exceed that of transport. As a result, kinetic studies on sorption behavior of U(VI) with Hanford sediments are also an important process to understand the transport of U(VI) and have been believed to be one factor for the plume longevity. The release process was slow in 300 area (Zachara et al. 2013). In the above adsorption batch experiment (Stoliker et al. 2011, Stoliker et al. 2013)), 500 – 1000 h was required to reach adsorption equilibrium, where mineral dissolution changes the chemical conditions of the aqueous equilibrium state. Smith's study (Smith and Szecsody 2011) investigated the effect of contact time on the extraction of U(VI) by using carbonate and acetic acid. The results showed the chemical alternation of uranium-sediment association along with the contact time. In this study, time-dependent extraction and continuous leach by carbonate (pH=9.3) and acetic acid (pH=2.3) solutions were conducted with sediments that has been incubated for different durations. Time-dependent batch extraction showed a rapid initial release followed by a slow increase. The fitting results indicated that the release process was not a simple diffusion or first-order process. In the batch study, a two process model was used, including a rapid desorption process followed by first-order release process, possibly due to dissolution of mineral phases. Both experiments showed an increasing resistance to extraction with longer incubation, which could be caused by an increase in U-mineral adsorption strength (recalcitrant).

Transport models have been set up in many studies. In a kinetic study of short-term U(VI) sorption (Qafoku et al. 2005), CXTFIT was used to determine transport parameters of Br and a one dimensional distributed rate coefficient model was used to describe U behavior. In this 1-D distributed rate coefficient model, first-order rate coefficients for a hypothetical assemblage of reaction site groups were fitted according to a r-distributed statistical model, assuming the first-order rate coefficients followed a gamma probability distribution. The distribution coefficient (K_d) was assumed as a single value for all sorption sites. Long tailing phenomena occurred for columns which indicated sorption-related non-equilibrium conditions.

A long term kinetic study of uranyl desorption was performed with column experiments (Shang et al. 2014). In the reactive transport model, advection dominates the mobile domain and diffusion dominates the immobile domain. Multirate SCM is also applied here in both domains. In addition to the dual domain transport model and multirate SCM, which were also used in previous studies, here an additivity model was applied to incorporated with them. Two types of additivity models were used separately, one considered grain size properties and one considered composite-based properties. The characterization of sediments with different size factions was consistent with previous result, where they had variable surface area and labile U(VI) content.

The objective of the experiments presented here was to (1) quantify U(VI) uptake by sediments in batch system with surface complexation modeling, (2) simulate U(VI) adsorption by a multi-rate first order reaction model, (3) predict U(VI)

transport through column systems under two flow rates and (4) interpret the time-dependent sequential extraction results.

3.2 Materials and Methods

3.2.1 Materials

Sediments used in the kinetic adsorption and column experiments were described in Chapter 2. Synthetic Hanford groundwater (SHGW) with a target pH of 8.05 was prepared to represent the composition of groundwater at the site (Table 2.1) (Zachara et al. 2005).

3.2.2 Kinetic adsorption

Sorption kinetics were examined with triplicate suspensions at an initial U(VI) concentration of 2.65 µM by combining 30 g of sediments with 120 mL of SHGW in polypropylene tubes (250 g/L). The U(VI) concentration was close to the influent U(VI) concentration (~3.5 µM) used in later column experiments. Aliquots (1 mL) of the suspension were taken immediately after mixing and at 0.10, 0.32, 1.0, 3.2, 10, 30, 102, 316, 960, and 2880 min and treated for chemical analysis.

3.2.3 Column experiments

The experiment set up has been demonstrated in Chapter 2. For column experiments, a 3.5 µM $UO_2(NO_3)_2$ solution was used during the uptake of U(VI) by the sediments,

and 1 mM phosphate (0.85 mM $Na_2HPO_4 \cdot 7H_2O$ and 0.15 mM NaH_2PO_4) was used for treatment of U-loaded sediments. Column 5&6 were operated at a flow rate of 8 mL/h and Column 7&8 were operated at 16 mL/h. Column 5 and Column 7 went through the conditioning phase and uptake phase. Column 6 and Column 8 went through the conditioning phase, uptake phase and the release phase with the presence of phosphate.

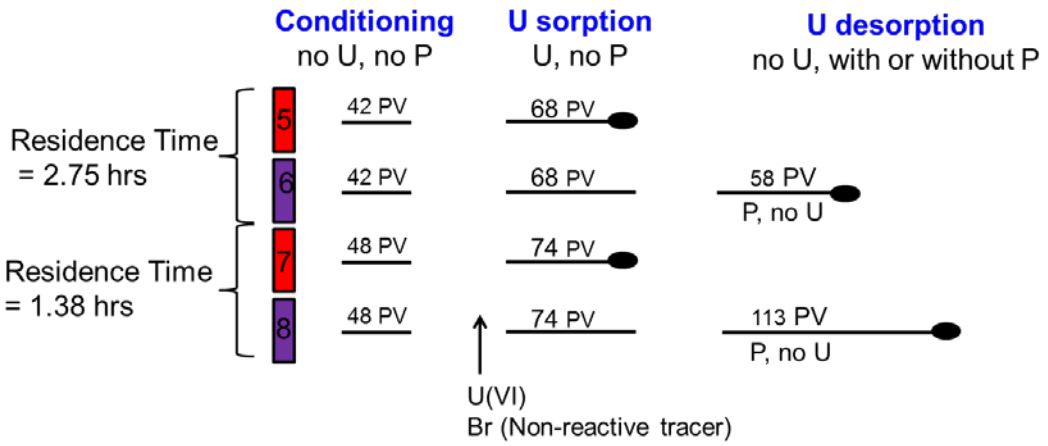

Figure 3.1 Operation phases for Column 5 to 8. Each phase corresponds to an influent composition. The flow rate was such that one pore volume (22 mL) is equivalent to 2.75 h for Column 5 and 6, 1.38 h for Column 7 and 8. Black circles mark the end of the operation for each column.

3.2.4 Time dependent Sequential Extractions

The sequential extraction procedures have been described in Chapter 2. After the end of column experiments (for Col-U, Col-U-P and Col-U-P-NP), 2 g of sediments from each session were collected and extracted to obtain U(VI) in five forms. In order to assess the rate of extraction, a time-dependent sequential extraction was conducted with ammonium acetate (extractant in step 2) and then acetic acid (extractant in step

3). Duplicate samples (8 g each) from each section were mixed with 200 mL of extraction solution. Aliquots of the suspension (1 mL) were collected at 0.10, 0.32, 1.0, 3.2, 10, 30, 60, 100, 316 and 960 min and treated for chemical analysis.

3.3 Results and Discussion

3.3.1 Modeling adsorption experiments in batch system

Adsorption kinetics showed that adsorption was initially very rapid and then had slower continuing uptake (Figure 3.3). The continuing slower adsorption was controlled by either chemical or physical limitations to adsorption. Some previous studies confirmed the presence of fast and slow intra-particle diffusion domains in the sediments.(Bai et al. 2009, Liu et al. 2006) The adsorption process was predicted with a model including an initial period with instantaneous uptake in the first 20 s and a second period with rates described by an established equation for a multi-rate sorption process with a first-order rate coefficient k_i (L/kg-hr) following a log-normal distribution. The ability of the multi-rate sorption model to fit the data is consistent with intra-particle mass transfer process playing a role in the uptake of an adsorbing contaminant by heterogeneous porous media (Bai et al. 2009, Liu et al. 2009a, Qafoku et al. 2005).

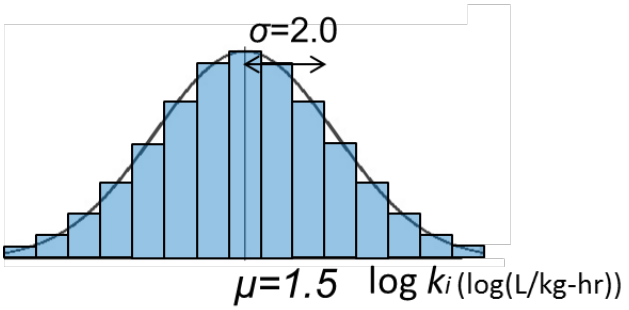

Figure 3.2. Schematic figure of a log-normal distribution for the first-order reaction constant.

The rate of adsorption was initially very rapid and then slower with continuing uptake. The rapid uptake is described as instantaneous uptake for the first 20 s. The period of slower uptake begins at 20 s and with an aqueous U(VI) concentration of 524 μg/L at that time. The slow uptake process is described by a model which has a log-normal distribution of first-order rate coefficients k_i (L/kg-hr) (Figure 3.2). The distribution has a log-normal mean μ (log(L/kg-hr)) and a log-normal standard deviation σ (log(L/kg-hr)). Each k_i is the averaged value in each interval (Bai et al. 2009):

$$\frac{dC_b}{dt} = -SWR \sum_{i=1}^{n} f_i k_i (C_b - C_{p,i}) \qquad \text{(Equation 3.1)}$$

C_b is the bulk [U(VI)] (μg/L), $C_{p,i}$ (μg/L) is [U(VI)] in the intra-particle pore solution for site *i*. The distribution is evenly discretized into *n* sites and 100 was used for *n*.

For each site *i*,

$$\frac{dS_i}{dt} = k_i\left(C_b - C_{p,i}\right) \qquad \text{(Equation 3.2)}$$

$$S_i = K_d \cdot C_{p,i} \qquad \text{(Equation 3.3)}$$

where S_i (µg/kg) represents sorbed U(VI) in site *i*, K_d ((µg/kg)/(µg/L)) is the partition coefficient. The value of K_d for use in the model was taken from the sorption isotherm with no phosphate. The total U(VI) is the sum of the dissolved U(VI) and the total sorbed U(VI) from all sites. The model was numerically solved using a backward-in-time finite difference method. The selected result was chosen when a minimum sum of the square of the residuals was achieved, which is the sum of the difference between experimental data and predicted results.

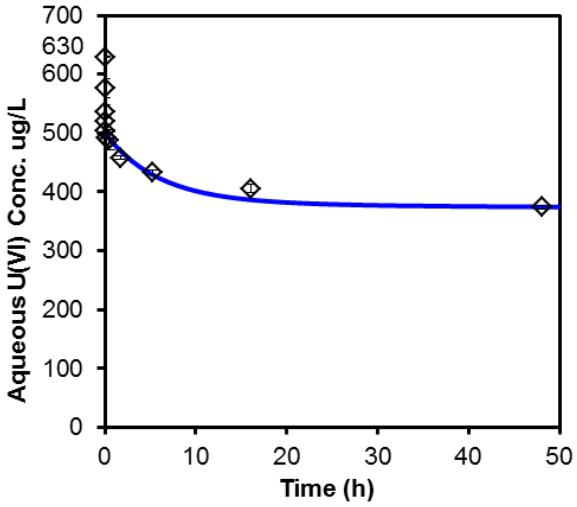

Figure 3.3. Kinetic adsorption with initial U(VI) concentration of 630 µg/L, at pH ~ 8.05 with solid:solution ratio 250 g/L. The multi-rate first order kinetic sorption model was applied beginning at 20 s with a dissolved U(VI) of 524 µg/L at that time. Error bars from duplicate experiments are smaller than the points.

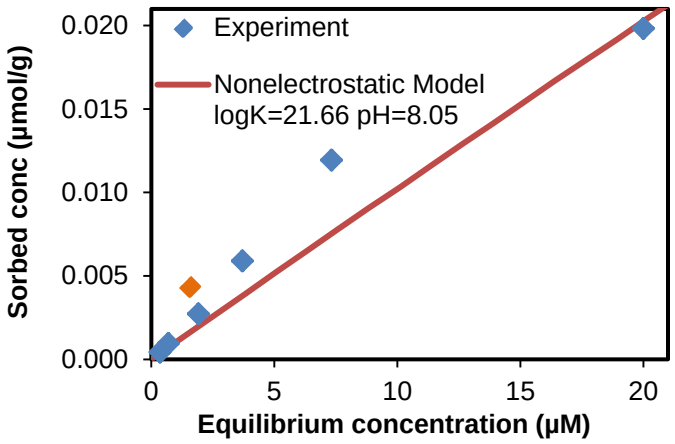

Figure 3.4: SCM for U(VI) adsorption to Hanford sediments at pH ~8.05. Blue points are batch-isotherm experiments data and the yellow point is the equilibrium point from the kinetic study.

The adsorption isotherm with no phosphate has been fitted well by the same reactions and equilibrium constants as were used in a previous study (Figure 3.4) (Stoliker et al. 2011). The successful application of a non-electrostatic model can be due to the complicated composition included in the sediments leading to no change of surface electrostatics over the range of conditions studied. The slightly low estimated result might be because of small difference in groundwater compositions.

3.3.2 Uranium transport under different flow rates and modeling by CXTFIT

U(VI) breakthrough profiles in Column 5 to 8 followed similar features as observed in preciously discussed four columns in Chapter 2, where during the uptake phase, effluent U(VI) concentrations increased slowly and finally reached the influent level. However, the flow rate was observed to affect the U(VI) profile. The U(VI)

concentration in the effluent began to increase after less cumulative water had passed through the columns at the higher flow rate in Columns 7 and 8 compared to Columns 5 and 6 (Figure 3.5). At the higher flow rate, there was less time for U(VI) to diffuse into intragranular pores when the same amount of SHGW had passed through columns. Ultimately less U(VI) was retained in the columns, suggesting that the rate of U(VI) retention is limited by mass transfer from the mobile pore water into immobile water in intragranular pores.

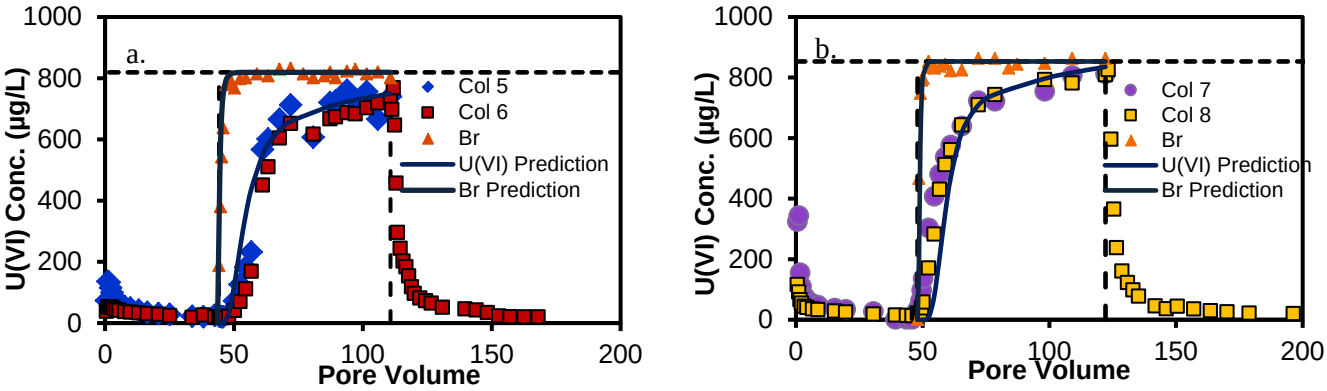

Figure 3.5. U(VI) and Br profiles for Columns 5-8. Symbols represent experiment data and smooth lines are the prediction results from reactive transport model by CXTFIT, with parameters in Appendix (Table 2). Column 5 and 7: conditioning phase, uptake phase; Column 6 and 8: conditioning phase, uptake phase and release phase with P. Br profiles were plotted as C_{eff}/C_{inf} times the influent U(VI) concentration.

In transport reactive modeling, a non-equilibrium model is used to fit Br and U transport behavior in columns based on the assumption that the aqueous phase can be partitioned into mobile and immobile regions, which is called a dual domain reactive transport model (Tang et al. 2009). The dimensionless equation:

$$\beta R \frac{\partial C_m}{\partial T} = \frac{1}{Pe} \frac{\partial^2 C_m}{\partial X^2} - \frac{\partial C_m}{\partial X} - \omega(C_m - C_{im}) \qquad \text{Equation 3.4}$$

$$(1-\beta)R\frac{\partial C_{im}}{\partial T} = \omega(C_m - C_{im}) \qquad \text{Equation 3.5}$$

where *m* and *im* indicate the mobile and immobilize zones respectively, R=1+ $\rho_b k_d/\theta$, ρ_b is the bulk density (kg/m^3), $Pe=vL/D_L=L/\lambda$, and $C=c/c_o$, where λ is the dispersity, k_d is partition coefficient and θ is the porosity, ω is dimensionless mass transfer coefficient

$$\omega = \frac{\alpha L}{\theta v} \qquad \text{Equation 3.6}$$

$$\beta = \frac{\theta_m + f\rho_b K_d}{\theta + \rho_b K_d} \qquad \text{Equation 3.7}$$

where α is the first-order mass transfer coefficient (s^{-1}) between the mobile and immobile liquid regions, θ_m as the mobile pore water content and *f* is the fraction of adsorption sites that equilibrates with the mobile liquid phase.

In the modeling practice, *Pe*, β(Br), β(U) and ω (ω =ηD$_o$, Do as molecular diffusion coefficient in water) would be needed in non-equilibrium equation (MIM). Using these variables in the MIM equation could give predicted C/Co. The objective function SSR is the sum of the difference between experimental C/Co and predicted C/Co. The above formula input data are calculated based on *R*, λ (different for Br and U), $\theta m/\theta$, *f* and η (geometric factor). While retardation fact R is a guessed value, other variables are estimated based on 'Solver' to achieve a minimum SSR.

Columns 5, 6 (duplicates, set 1) were operated with flow velocity of 130 cm/day while columns 7 and 8 (duplicates, set 2) were operated with 260 cm/day. From uranium profile, it can be observed that under high flow rate, the time needed for effluent uranium concentration to reach half of influent concentration decreased

significantly, which indicates that uranium was not retained as efficiently as in columns with low flow rate. Based on operation conditions for four columns, several constraints should be achieved in CXTFIT if this model works. Col 5, 6 or Col 7, 8 should be fitted with the same set of parameters R, (β(Br), β(U) and ω) except that they would have different peclet numbers, *Pe*. The model should give different dispersivities for two sets of columns because of different velocities. For example, λ(Br, Col 5, 6) should be close to twice of λ(Br, Col 7, 8) and λ(U, Col 5, 6) would be close to twice of λ(U, Col 7, 8). In the same set of columns, there is also a relationship between λ(Br) and λ(U) as despersivity is related to molecular weight. As each parameter could be fitted individually, Br profiles were fitted first and the above relations among λ(Br) for four columns were achieved by slightly changing λ manually. Then U profiles were fitted with Br profiles simultaneously. CXTFIT could predict each column very well separately with different parameters. In order to obtain relations between λ(Br) and λ(U) in same column and λ(U) in different columns as described above, λ were slightly changed manually and same set $\theta m/\theta$, f and η values were used. As a consequence, best fits were not achieved (Table 3.1).

For Col 5 and Col 6, CXTFIT over predicted effluent uranium concentration at the beginning time period (Figure 3.6a and 3.6b) while for Col 7 and Col 8, there was an under prediction for similar beginning time period (Figure 3.6c and 3.6d). It can be concluded that this simplified non-equilibrium transport modeling has limitations to fit uranium transport behavior under different flow rates with the assumption that only adsorption accounts for the retardation and reaction rate is a constant. If adsorption was the only mechanism, the process could still be mass-

transfer rate limited as the time scale of adsorption may be longer than the residence time. As a result, when flow rate increases, less uranium would be adsorbed and contributed to the earlier breakthrough of uranium.

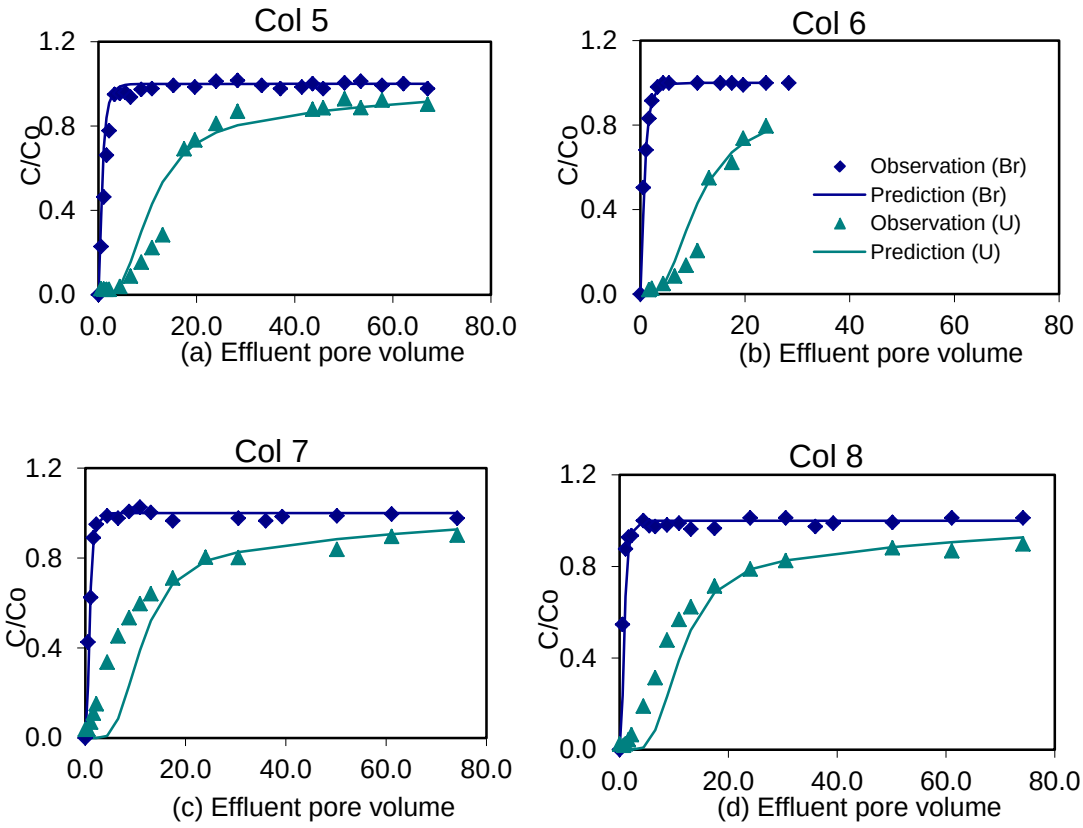

Figure 3.6. Effluent Concentration (C): Influent Concentration (C_0) profile of Br and U in flow-through column experiments (symbols) and non-equilibrium transport model fits (lines).

In order to get a better prediction for uranium transport behavior, it would be likely that more zones (a third zone) could be added which exhibits properties between mobile zone and immobile zone, with mass transfer between two nearby zones. More distributed zones might be able to take account the over predicted part in low flow rate columns and under predicted part in high flow rate columns. Also a

multi-rate adsorption could be considered with the change of surface complexed uranium on mass-transfer sites. Adsorption rate would not be a constant because of increased amount of uranium retained in the sediment rather it would be a function of aqueous chemical components, such as surface area and site density of adsorption-sites. In many reported articles, a multi-rate surface complexation model was used where rates of adsorption were calculated by considering mass transfer rates and equilibrium aqueous chemistry along with the operation time. The mass transfer coefficients were described by a lognormal probability distribution but would be calculated as a finite number (Qafoku et al. 2005, Shang et al. 2014, Stoliker et al. 2013). In conclusion, both more zones and multi-rate surface complexation would be helpful for non-equilibrium modeling to better fit uranium transport under various flow rates.

Table 3.1. Transport parameters for column experiments

Column	Peclet number for Br	Peclet number for U	Retardation factor R	Mobile water fraction for U	Dimensionless mass transfer coefficient ω
5	2.36	6.00	24.3	0.52	0.27
6	2.36	6.00	24.3	0.52	0.27
7	4.99	10.12	24.3	0.51	0.27
8	4.99	10.12	24.3	0.51	0.27

3.3.3 Sequential extractions and comparison to the mass balance calculations

The sequential extraction results showed that after the release phase with the presence of phosphate, most U(VI) was retained in sediments and the lost amount of U(VI) was from the most labile forms (Figure 3.7). The distribution of U(VI) from the column did not have significant decreasing trend, which is consistent with the column behavior described in Chapter 2. Due to the accumulation of U(VI) in first four columns, the comparison between mass balance calculation and sequential extraction showed differences and the accumulation has been largely avoided in Column 5 to 8. As a result, a more precise match could be obtained between mass balance calculation and sequential extraction.

For Column 5 and Column 6, they were consistent with each other from the profile and the net uptake were 2.05 and 2.19 μg/g from mass balance calculation (Table 3.2). The calculated net accumulation for Column 5 and Column 6 were 2.05 and 1.53 μg/g at the time that the sediments were removed for sequential extractions (Table 3.3). Those sequential extractions yielded concentrations of 1.65±0.63 μg/g of accumulated U for Column 5 and 1.19±0.63 μg/g for Column 6, which was within 80% and 78% of mass balance estimate, respectively. Sequential extraction gives more reliable results as it directly measures the U(VI) associated with the sediments.

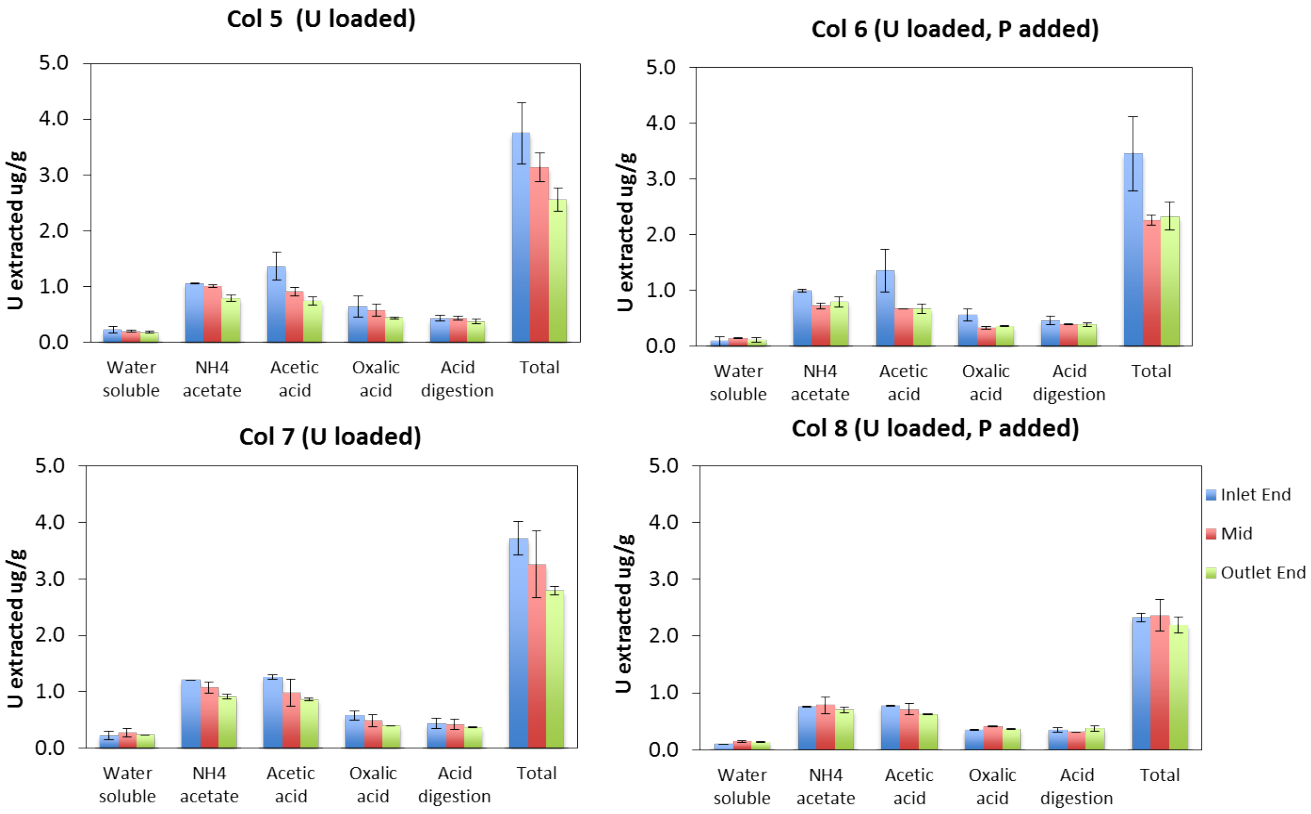

Figure 3.7. Sequential extraction results for U(VI) extracted from sediments removed in three sections from (a) Col-U, (b) Col-U-NP, (c) Col-U-P, and (d) Col-U-P-NP. Error bars represent the standard error for the data obtained from duplicate samples. Blue: inlet sections, red: mid sections, green: outlet sections of each column.

Table 3.2. Released/accumulated amount of U(VI) from mass balance calculation from U(VI) profile in Figure 3.5.

µg U/g sediments	Column 5	Column 6
Sediments (g)	150	149
Conditioning (µg/g)	0.24	0.18
U(VI) (Influents - Effluents) (µg/g)	2.27	2.53
U(VI) precipitated in tubing sections (µg/g)	0.22	0.34
Calculated U(VI) accumulated in sediments(µg/g)	2.05	2.19
Mass Released (µg/g)	-	0.66
Net accumulation (µg/g)	2.05	1.53

Table 3.3. Total U(VI) extracted from the sediments for additional two columns.

Mass of U(VI) (µg/g)	BG	Column 5	Column 6
Sequential Extraction	1.50±0.30	3.15±0.33	2.69±0.33

3.3.3 Time-dependent sequential extractions

Sediments after column experiments from Col-U, Col-U-P and Col-U-P-NP went through the time-dependent sequential extraction process. The extraction rate experiment showed a rapid initial release followed by a slow release process for all samples (Figure 3.8). This biphasic release was observed with two different extractants. The slow desorption was possibly due to the diffusion of U(VI) from intra-particle pores to bulk solution, which was consistent with the adsorption rate experiments that also had a slow mass transfer period that was probably due to intraparticle diffusion. Equation (S5) was used to approximate the release process, where the final concentration (C_T) (µg/g) was considered as the total U(VI) in sediments at the beginning, *C(t=0)* represents an instantaneous release and *C(t) – C(t=0)* represents U(VI) released from a slow process with the time.

$$C(t) = C_T - A \cdot e^{-k \cdot t} \qquad \text{Equation 3.8}$$

Approximately 30 to 39% of U(VI) was released instantaneously, which is close to the fraction of adsorption (36%) that could be considered to be instantaneous. The reaction rate coefficients were in the same magnitude and the percentages of instantaneous release along the desorption process were similar for all samples with and without phosphate treatment (Table 3.4 and 3.5). The immobilized U(VI) still has similar mobility by the same extraction solutions before and after phosphate treatment. This could be because the differences in the strength of U(VI) binding to

the sediments are smaller than the differences that would be detectable by the different extraction processes. In addition, the phosphate is not affecting the intra-particle mass transfer processes that are probably responsible for the rate-limited adsorption and the rate-limited extraction, which has also been excluded as a mechanism for the inhibition of U(VI) desorption (Shi et al. 2009).

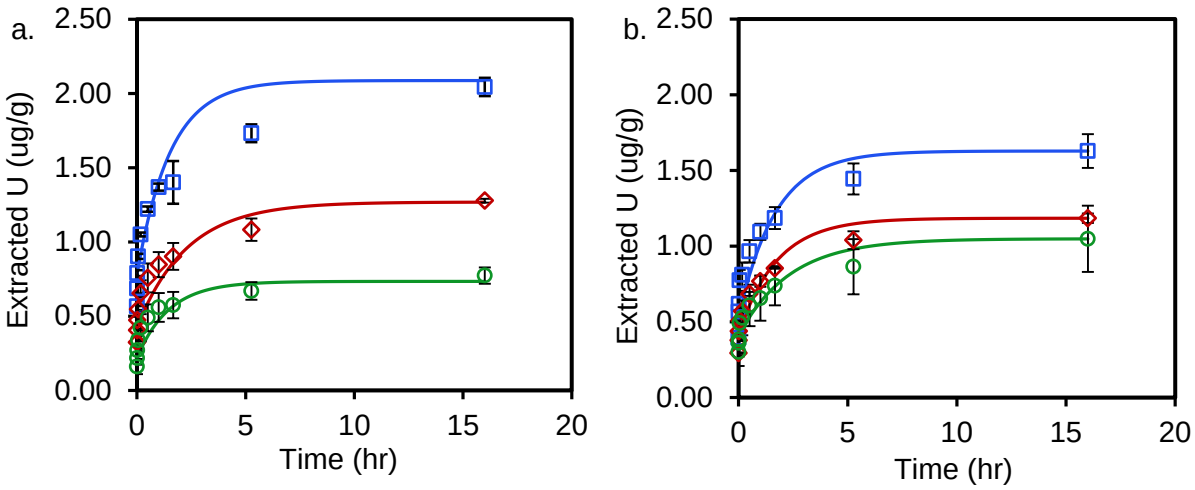

Figure 3.8. Kinetic desorption of U(VI) associated sediments from Col-U (□), Col-U-P (◊) and Col-U-P-NP (○) by (a) ammonium acetate and then (b) acetic acid for 16 hours. Error bars represent standard errors from triplicate experiments. Lines are the output of the simulations for interpreting the process using equation S2.

Table 3.4. Kinetic extraction of U(VI) included a rapid process (regarded as instantaneous release) followed by a slow release.

		A (μg/g)	k (hr^{-1})
Step 2 (Ammonium Acetate)	Col-U	1.31±0.17	0.65±0.45
	Col-U-P	0.84±0.10	0.44±0.23
	Col-U-P-NP	0.52±0.07	0.68±0.37
Step 3 (Acetic Acid)	Col-U	1.10±0.12	0.59±0.31
	Col-U-P	0.77±0.08	0.57±0.25
	Col-U-P-NP	0.64±0.08	0.43±0.23

Table 3.5. Extent of Instantaneous release in time-dependent extraction experiments. The extent (percentage, %) of instantaneous release U(VI) was calculated as *C(t=0)/C(t)*, where *C(t=0)* is the initial U(VI) concentration in solution.

	Step 2			Step 3		
Time	Col-U	Col-U-P	Col-U-P-NP	Col-U	Col-U-P	Col-U-P-NP
6 s	100	100	100	100	100	100
19 s	99	100	99	99	99	100
1 min	98	99	97	98	98	99
3 min 10 s	95	96	92	94	95	97
10 min	85	88	80	84	86	90
30 min	68	72	59	65	69	77
1 h	55	59	46	52	56	65
1 h 40 min	48	49	38	43	47	55
5 h 16 min	39	36	30	33	36	42
16 h	37	33	30	32	35	39

3.4 Conclusions

This chapter has described the application of modeling approaches to batch adsorption experiments, kinetic adsorption and column behavior under different flow rates. The kinetic adsorption revealed an intra-particle diffusion process controlling the adsorption of U(VI) by sediments. The surface complexation modeling could successfully being applied to describe the U(VI) adsorption by sediments with no phosphate. An additional four columns have been described here that indicated the impact of flow rate and the behavior could be simulated by a simplified one-dimensional reactive transport model, although a small discrepancy existed between the experiment data and the modeling results. In Appendix B, a surface complexation model was developed for enhanced U(VI) adsorption with the addition of phosphate. As being indicated in many previous studies, the U(VI) uptake in a column would be largely affected by the water chemistry, an advanced reactive transport model was

being developed to include the impact of the advective flow, surface complexation reactions, kinetically controlled mineral dissolution processes.

Chapter 4. Measurement and Surface Complexation Modeling of U(VI) Adsorption to Engineered Iron Oxide Nanoparticles

Results of this Chapter have been submitted to *Environmental Science & Technology* and the manuscript is currently under review.

Graphic Abstract

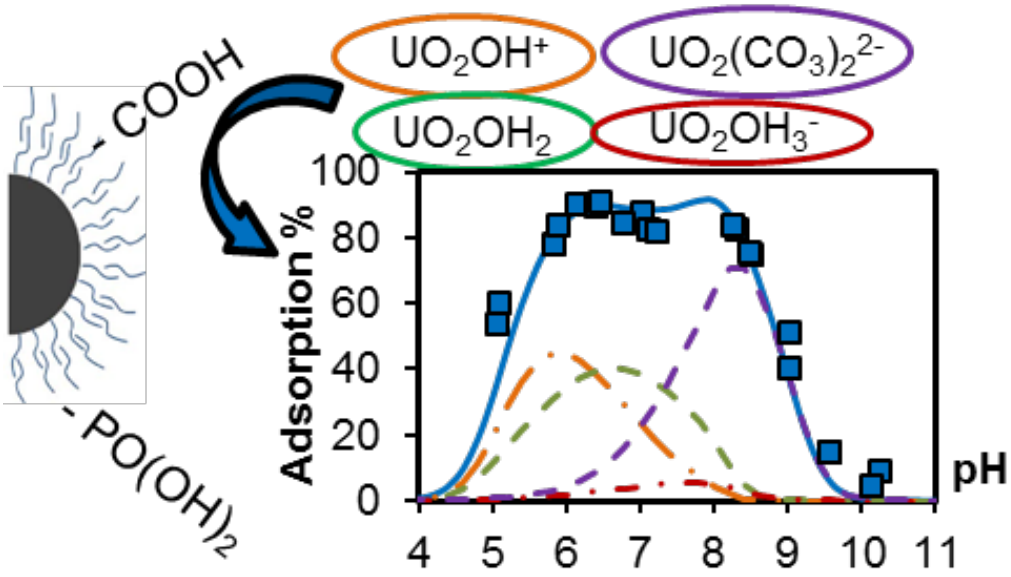

Abstract

Surface-functionalized magnetite nanoparticles have high capacity for U(VI) adsorption and can be easily separated from the aqueous phase by applying a magnetic field. A surface-engineered bilayer structure enables the stabilization of nanoparticles in aqueous solution. Functional groups in stearic acid (SA), oleic acid (OA) and octadecylphosphonic acid (ODP) coatings led to different adsorption extents (SA≈ OA > ODP) under the same conditions. The adsorption of U(VI) to OA-coated nanoparticles was examined as a function of initial loading of U(VI) (5-15 μM), pH (4.5 to 10), and the presence or absence of carbonate. A surface complexation model was developed to interpret the adsorption behavior. With a small set of adsorption reactions for uranyl hydroxide and uranyl carbonate complexes to surface sites, the model can successfully simulate the entire adsorption dataset over all uranium loadings, pH values, and dissolved inorganic carbon concentrations. The results show that the adsorption behavior was related to the changing U(VI) species and properties of surface coatings on nanoparticles. The model could also predict pH-dependent surface potential values that are consistent with measured zeta potentials.

4.1 Introduction

Uranium contamination of the environment has resulted from activities associated with past weapons production and mining processes as well as natural processes (Pan et al. 2016b). The U.S. drinking water standard for uranium is 30 ug/L. Uranium mainly exists in oxidation states of U(IV) and U(VI), and U(IV) is a less soluble form and is only found in relatively reducing environments. U(VI) can exist as the uranyl ion (UO_2^{2+}) and different aqueous complexes of uranyl with hydroxide and carbonate, and the exact speciation can affect the ability to remove U(VI) from water.

Iron oxide-based materials are attractive sorbents for the removal of heavy metals from water due to their high surface area and reactivity (Wang et al. 2012, Xu et al. 2012, Zeng et al. 2008). Adsorption of metal contaminants (e.g., U, Cr, As) by nanoscale iron oxides have been extensively studied. Research has examined the impact of particle size and of water chemistry parameters such as pH, ionic strength and carbonate concentrations on U(VI) adsorption behavior (Singer et al. 2012a, Wang et al. 2011a, Zeng et al. 2009). Solution pH affects the surface charge of many sorbents and the speciation of U(VI) complexes, thus affecting the adsorption affinity. The presence of carbonate results in U(VI)-carbonate complexes being the dominant species at neutral pH and above, and these generally have lower adsorption affinity to adsorbents (Pan et al. 2016b, Wang et al. 2012, Wazne et al. 2003). Although a number of iron oxide materials have been demonstrated as effective adsorbents, aggregation of bare iron oxide nanoparticles can limit their application in real water treatment systems.

The surface of iron oxide nanoparticles can be modified to be coated with a diverse range of materials, including humic acid, polymers and fatty acids (Bruce and Sen 2005, Ge et al. 2015, Jiang et al. 2014, Li et al. 2016a) that can prevent aggregation (Jiang et al. 2014, Li et al. 2016a). Superparamagnetic engineered nanoparticles have high potential for water treatment due to the ease of separation from the aqueous phase by applying a relatively low magnetic field (Li et al. 2016c, Yavuz et al. 2006). Humic acid-covered magnetite particles effectively removed the metal contaminants Hg(II), Pb(II), Cd(II) and Cu(II) from tap water and natural waters at pH from 2 to 9 (Liu et al. 2008). Functional groups of humic acid were also reported to be responsible for the reduction of Cr(VI) to non-toxic Cr(III) (Jiang et al. 2014). Chitosan (polysaccharide)-bound magnetic nanoparticles were prepared for removal of Cu(II) ions (Chang and Chen 2005). Manganese ferrite/magnetite nanoparticles coated with fatty acids have been applied for U(VI) sorption (Li et al. 2016c, Zhang 2003). However, the impact of water chemistry on the adsorption of U(VI) to magnetite coated with fatty acids has not been thoroughly investigated in terms of pH, U(VI) loadings and the presence or absence of dissolved inorganic carbon.

Surface complexation modeling (SCM) is a quantitative tool for predicting metal adsorption in a reaction-based framework that accounts for the full aqueous speciation, surface chemical reactions, and the impacts of surface potential on the adsorption of charged species (Payne et al. 2013, Wang et al. 2012, Xie et al. 2016). SCM accounts for the impact of water chemistry on aqueous and surface speciation in predicting adsorption over a broad range of conditions with a set of reactions and

corresponding reaction constants (Wang and Giammar 2013). In most previous studies that used SCM to interpret U(VI) adsorption to a material, the adsorption sites were the hydroxyl groups at the surface of inorganic solids (e.g., iron oxides, aluminum oxides, or clay minerals) (Xu et al. 2006, Zeng et al. 2009). Some studies have included adsorption sites of carboxyl groups, hydroxyl groups, and carbonyl/epoxy groups and have simulated U(VI) adsorption onto carbonaceous nanofibers (Sun et al. 2016, Zhang et al. 2015). However, the ability to apply SCM to understand the binding of adsorbates to functional groups of organic compounds that are coated on the surface of an inorganic solid has not been unexplored. Whether or not modeling metal adsorption to such functionalized metal oxide sorbents must still consider electrostatic contributions to adsorption in addition to the chemical binding to the functional groups remained an open question when we designed our experiments.

In our previous study we reported on the synthesis and characterization of a set of nanoparticles with controlled size and coated with various organic acids (Li et al. 2016a). Due to high monodispersivity, precisely controlled surface chemistry, and extensive characterization, these materials were chosen for the present study on the effects of water chemistry on the adsorption of U(VI) to surface functionalized nanoparticles. The objectives of the present study were to (1) identify the impact of surface coatings on U(VI) adsorption by engineered iron oxide nanoparticles over a wide range of pH conditions, (2) investigate the effect of water chemistry on U(VI) adsorption to OA-coated nanoparticles, and (3) develop an equilibrium adsorption model to simulate U(VI) adsorption over various conditions.

4.2 Materials and Methods

4.2.1 Materials

Iron oxide (Iron III, hydrated, catalyst grade), 1-octadecene (technical grade, 90%), oleic acid (OA, 99.0%), steric acid (SA, 99.0%), octadecylphosphonic acid (ODP, 99.0%), sodium hydroxide (ACS reagent, 99.0%) and nitric acid (trace metal grade) were purchased from Sigma-Aldrich. Reagent grade hexane, acetone, and ethanol were also purchased from Sigma-Aldrich and used without purification.

4.2.2 Nanoparticle Synthesis and Phase Transfer

Iron oxide nanoparticles were prepared according to a published thermal decomposition method (Li et al. 2016a, Li et al. 2016b). The details of the procedure are presented elsewhere, and they involved synthesis and purification steps that resulted in an iron oxide suspension in hexane (Li et al. 2016a). Iron oxide nanoparticles in hexane were characterized by transmission electron microscopy (TEM, FEI Tecnai G2 Spirit) by preparing the TEM specimens using carbon support film on 300 mesh copper grids.

The iron oxide nanoparticles in hexane were transferred to ultrapure water by forming a bilayer structure through a ligand addition method. Various amounts of organic acids were dissolved in ultrapure water (resistivity > 18.2 MΩ-cm) to obtain 5 mM oleic acid (OA), 5 mM stearic acid (SA) and 10 mM octadecylphosphonic acid (ODP) solutions. Nanoparticles in hexane (1~2 mL) were added to a glass vial

containing 8 mL of aqueous solution with the organic acid. The mixture was placed under a probe sonicator (UP 50H, Dr. Hielscher, GMHB) under 70% amplitude for 5 min. After sonication, the residual hexane was evaporated from the suspension over 24 hours. The suspensions were purified by three steps of membrane filtration (ultrafiltration cellulose membranes, 100 kDa MWCO) and filtration through a syringe filter (pore size of 0.2 um, Millipore). The final products were collected in amber glass vials for storage prior to use in experiments.

4.2.3 U(VI) Adsorption

U(VI) adsorption to nanoparticles coated with three different organic acids was studied. After studying the three types of particles, U(VI) adsorption to OA-coated nanoparticles was further investigated to determine the impact of pH, initial U(VI) loading and the presence or absence of dissolved inorganic carbon on adsorption. For each set of batch experiments, nanoparticle stock suspension was diluted into a 200-mL beaker with air being bubbled into the suspension for more than 20 minutes. A different approach was used for carbonate-free experiments that will be discussed later. U(VI) stock solution was added to the nanoparticle suspension to achieve a nanoparticle dose of 28 mg/L as Fe_3O_4 and one of three target initial U(VI) loadings (4.6, 9.4 and 17 μM). SA- and ODP-coated nanoparticles were only tested with the middle U(VI) loading. The suspension was distributed into 15-mL test tubes and pH was adjusted to target values (4 to 10) by addition of 0.1 M NaOH and 0.1 N HNO_3 with air being bubbled continuously to achieve equilibrium exchange with atmospheric CO_2. For adsorption experiments with OA-coated nanoparticles at

different U(VI) loadings, initial suspensions (12 mL) were prepared in individual test tubes with target concentrations of nanoparticles and U(VI). In order to reach carbonate equilibrium conditions at pH higher than 9, aliquots of sodium carbonate/sodium bicarbonate solutions were added before adding the U(VI) to obtain dissolved inorganic carbon concentrations at the target pH values that were already close to equilibrium with atmospheric CO_2 before bubbling the tubes with air to achieve full equilibration. The suspensions were mixed by end-over-end rotation for 24 hours and pH was measured and readjusted periodically. Control experiments were conducted through the same steps with either no U(VI) added or without nanoparticles. After 24 hours nanoparticles were separated from the suspension by ultracentrifugation at 45,000 rpm for 2 hours. The supernatants were collected and preserved in 1% HNO_3 for elemental analysis. Dissolved U and Fe concentrations were analyzed by ICP-MS (PerkinElmer); the absence of Fe in the supernatants was an indication that ultracentrifugation effectively separated the nanoparticles from the suspension. Carbonate-free adsorption experiments (OA-coated nanoparticles) were carried out in a glove box (Coy Laboratory Products Inc., MI) in which the gas in the chamber was pumped through a bed of $Ca(OH)_2$ and NaOH (Shimadzu soda lime CO_2 scrubber) to remove CO_2. For all batch experiments, a sample of the initial mixed suspension was digested in hot concentrated nitric acid to dissolve the nanoparticles, and the digested solution was diluted and then analyzed to determine the exact initial U(VI) and Fe concentrations.

4.2.4 Surface Complexation Modeling (SCM)

SCM was performed to quantitatively evaluate the impacts of pH and DIC on U(VI) adsorption to surface-functionalized nanoparticles and the relationships between U(VI) loadings and the available surface adsorption sites. The modeling was performed for adsorption experiments with OA-coated nanoparticles by using MINEQL+ V5.0 with the diffuse double-layer model. The SCM includes a full set of relevant aqueous reactions (Table S1 in the supporting information) in addition to surface acid−base and U(VI) adsorption reactions.

4.3 Results and Discussion

4.3.1 Synthesized Nanoparticles

As-synthesized nanoparticles have an average size of 8 nm as determined from TEM (Figure 4.1a). Our previous studies confirmed that these materials are magnetite based on X-ray powder diffraction (XRD) analysis (Li et al. 2016c). Surface passivation was achieved via an organic bi-layer structure with oleic acid as the first layer and various organic acids as the second, outer facing, layer (Figure4.1b) (Li et al. 2016a, Prakash et al. 2009). As the solution pH was adjusted from 4.5 to 10.5, all suspensions remained stable and monodispersed.

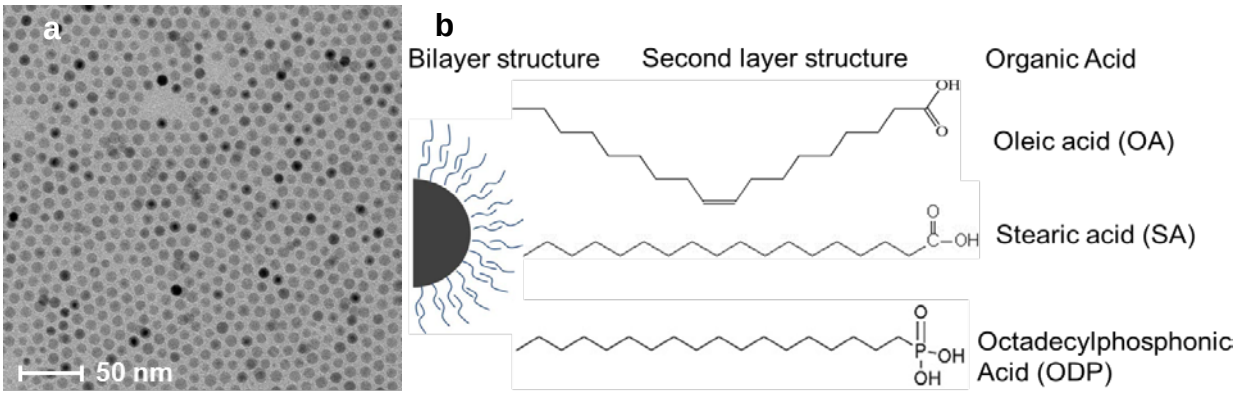

Figure 4.1. (a) TEM image for synthesized one layer coated-nanoparticles in hexane solution; (b) Bilayer-structure of surface coated nanoparticles with oleic acid as the first layer and different organic acids as the second layer.

4.3.2 Equilibrium Adsorption Experiments

4.3.2.1 U(VI) adsorption to nanoparticles with three types of surface coatings

The adsorption of U(VI) to OA-, SA- and ODP-coated nanoparticles was investigated over the pH range from 4.5 to 10.5 with a U(VI) loading of 9.4 μM. From the shapes of the adsorption edges for nanoparticles with each coating, the extent of adsorption increased from pH 5 to 6, reaching a maximum within the pH range from 6 to 7, and then decreased from pH 8 on (Figure 4.2). These observations follow a general trend of U(VI) adsorption for many sorbent systems (Waite et al. 1994). For example, the adsorption edge of U(VI) to manganese oxides has increasing adsorption starting at pH 2, a maximum from pH 4 to 8, and a decrease above pH 8 when carbonate is present (Wang et al. 2012). U(VI) adsorption loadings did not reach more than 90%, indicating that there might be limited

adsorption sites or that the affinity of the functional groups on the nanoparticles results in dissolved U(VI) persisting even with excess binding sites. OA- and SA-coated nanoparticles have similar extents of adsorption, with the highest adsorption densities of 103 and 97 ug/g when equilibrated in suspensions with a total U(VI) concentration of 9.4 µM at pH of 6 to 7. These are both higher than the adsorption densities on ODP-coated nanoparticles (82 ug/g) at the same conditions. The double bond in the OA structure versus the structure of SA with only single bonds did not affect adsorption.

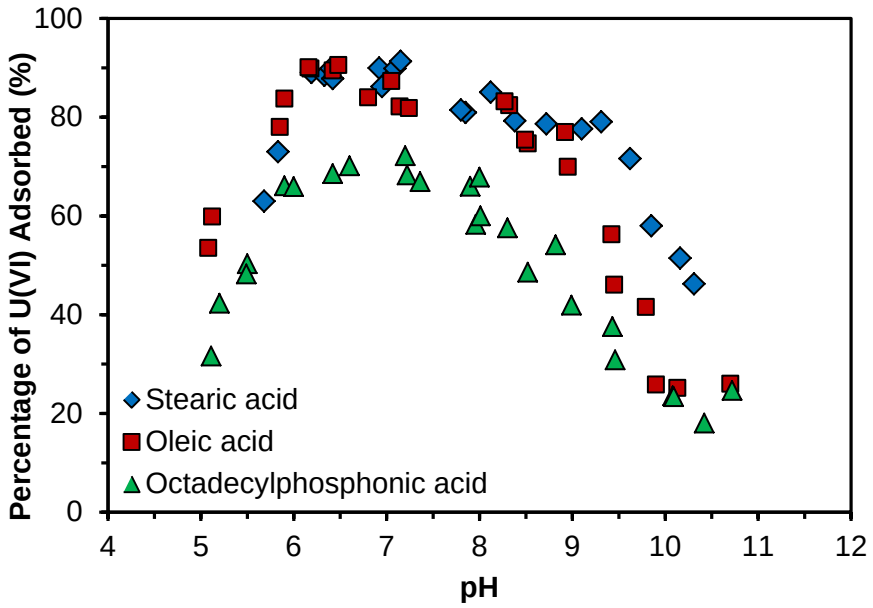

Figure 4.2. Percentage of total U(VI) that is adsorbed to stearic acid-, oleic acid- and octadecylphosphonic acid-coated iron oxide nanoparticles (28 mg/L as Fe_3O_4) in suspensions that are open to the atmosphere. The initial U(VI) loading was 9.4 µM. Ionic strength was 0.01 M.

Low adsorption at high pH (>9) was probably from the formation of U(VI)-carbonate complexes that stabilize U(VI) in water (Hsi and Langmuir 1985, Wazne et al. 2003). For all surface coatings evaluated, zeta potential values decreased with increasing pH as the surface became relatively more negatively charged, (Li et al. 2016a) which also further inhibited the adsorption of negative uranyl-carbonate species. High U(VI) adsorption capacity has been observed to SA-, OA-, ODP- and oleyl phosphate- (OP, unsaturated carbon chain) coated manganese oxide nanoparticles, due to binding of U(VI) to the phosphonate group ($PO(OH)_2$) and carboxyl group (COOH) (Lee et al. 2015a). Manganese oxide nanoparticles coated with OP and ODP had higher adsorption capacity than nanoparticles coated with SA and OA on the basis of q_{max} values when studied at much higher total U(VI) loadings than examined in the present study. This difference in adsorption capacity might result from stronger complexation of U(VI) by phosphate functional groups than by carboxyl groups (Lee et al. 2015a, Lee et al. 2015b). For our study, which was conducted at relatively low total U(VI) loadings, the adsorption densities are likely below the maximum capacity of the nanoparticles and differences in maximum capacities among different materials thus cannot be distinguished.

4.3.2.2 U(VI) adsorption to OA-nanoparticles and the impact of carbonate

The U(VI) adsorption to OA-, SA- and ODP-coated nanoparticles shown in Figure 4.2 was for conditions that did not reach complete air-water equilibrium, especially

at the highest pH values studied, as bubbling air could not bring the pH to target values. Consequently, the data shown in Figure 4.2 are defined as being partially air-water equilibrated. For the more in-depth study of U(VI) adsorption to OA-coated nanoparticles, fully carbonate-equilibrated experiments were performed with the addition of $NaHCO_3/Na_2CO_3$ (Figure 4.3). For OA-coated nanoparticles equilibrated with the atmosphere, the adsorption percentage decreased with increasing initial U loadings, yet it still did not approach 100% adsorption at the lowest initial U(VI) loadings (Figure 3).

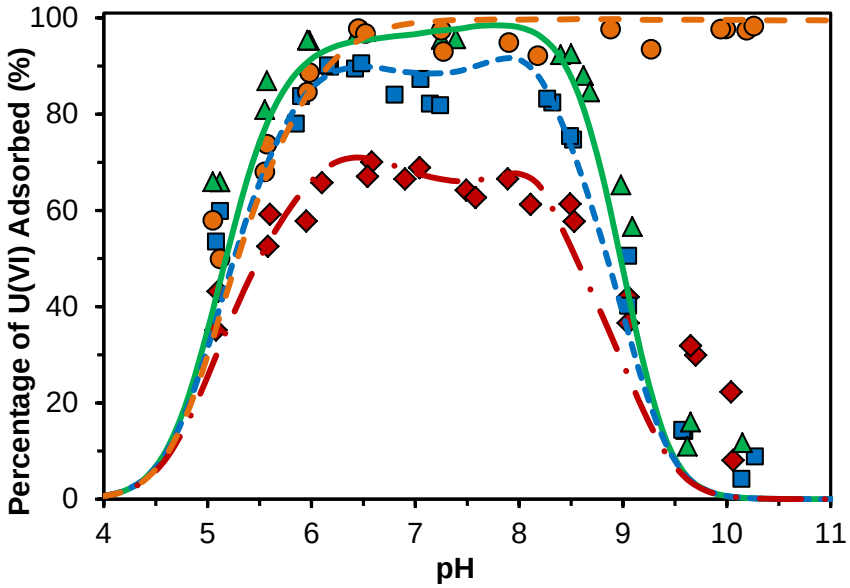

Figure 4.3. Percentage of U(VI) adsorbed to OA-coated iron oxide nanoparticles (28 mg/L as Fe_3O_4). Points are experiment data and lines are predicted results. ◊, —: 17 μM total U(VI) open to the atmosphere; □,- - : 9.4 μM total U(VI) open to the atmosphere; △, — • —: 4.6 μM total U(VI) open to the atmosphere; ○, — —: 9.4 μM total U(VI) in CO_2-free system. Ionic strength was 0.01 M. Lines are the predicted values from surface complexation modeling.

Carbonate significantly impacted U(VI) adsorption for the high pH conditions. For the same U(VI) loading (9.4 μM), the increase of dissolved inorganic carbon lowered the adsorption percentages. In carbonate free systems, more than 95% of U(VI) adsorbed at pH 9 (Figure 4.3, CO_2 free), but 70% adsorbed for the partially equilibrated system (Figure 4.2, OA) and only 40-50% for the fully equilibrated condition (Figure 4.3, 9.4 μM). A direct comparison of three adsorption edges at these different air equilibration conditions is included in the SI. The inhibition of adsorption by dissolved inorganic carbon was due primarily to the complexation of U(VI) by carbonate in solution that decreases the concentration of available UO_2^{2+} in solution.

Many previous studies have revealed that U(VI) has strong interactions with organic functional groups (Kazy et al. 2009, Lee et al. 2015a, Wang et al. 2006, Zeng et al. 2016). FTIR spectra before and after U(VI) adsorption to bacterial biomass, to OA and ODP-coated manganese oxide all had changes in the COO^- and PO_2^- vibrations due to the attachment of U(VI) to those functional groups on the surface of the adsorbents (Kazy et al. 2009, Lee et al. 2015a). The adsorption of U(VI) to gram-positive soil bacteria has also been modeled with UO_2^{2+} forming surface complexes with carboxyl and phosphate functional groups on the bacterial cell wall (Fowle et al. 2000). While it is theoretically possible that U(VI) was chemically reduced by the magnetite surface (Singer et al. 2012a, b), this is probably not the case for our experiments with surface-coated magnetite nanoparticles. Previous studies with OA-coated magnetite and oleyl phosphate coated manganese oxide nanoparticles only observed U(VI) reduction at high U(VI) loadings (400 μM U(VI)

for OA-coated magnetite) (Lee et al. 2015a, Li et al. 2016c). At the lower loadings of this study, U(VI) probably cannot diffuse through the two-layer OA-covered surface to be adsorbed on or reduced by the surface of the magnetite. Based on these observations, adsorption to surface functional groups was considered to be the dominant mechanism to account for U(VI) uptake in this modeling frame work.

4.3.3 Surface complexation modeling

4.3.3.1 Properties of nanocomposite surface and its corresponding modeling

In order to simulate the adsorption edges under different conditions, a SCM was established to first simulate the surface properties of nanoparticles (surface acid-base equilibrium constants and site density). Titration of nanoparticle suspensions was carried out in a glove box with CO_2 being scrubbed by a commercial CO_2 absorber. While the pK_a of the carboxylic group in aqueous solution is around 4.8, titration curves revealed that the nanoparticle suspensions provided effective buffering from pH 6 to 8 (Figure 4.4), which is consistent with the reported apparent pK_a values (between 6 and 8) in a previous study (Salentinig et al. 2010). There is a distinction between an intrinsic constant and an apparent constant for surface reactions that is accounted for in the double layer model, which considers the chemical energetics of the reaction as well as the energetics of ions approaching or leaving a charged surface. When the double-layer model is implemented for minerals (such as goethite

and ferrihydrite), an amphoteric surface hydroxyl is used to represent the surface site as ≡SOH with the possibility of forming both $\equiv SOH_2^+$ and

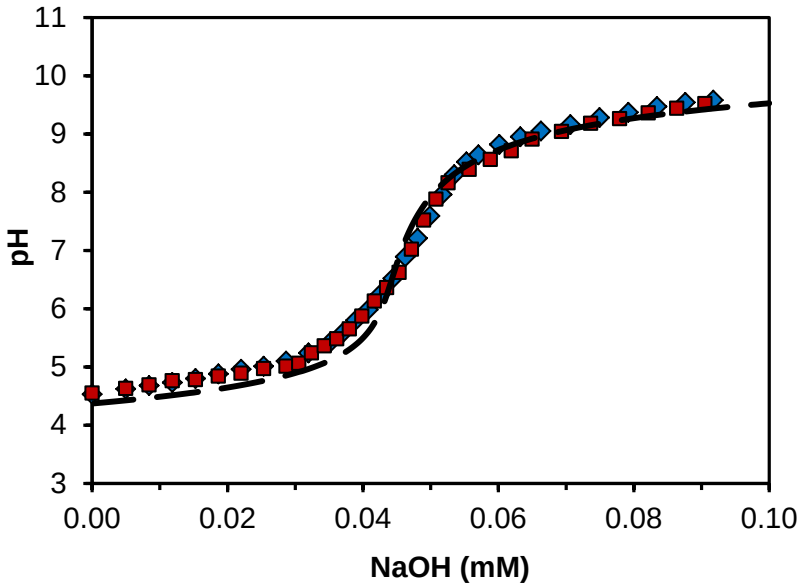

Figure 4.4. Titration curves for nanoparticle suspensions (adjusted to low pH at the beginning). Points are shown for two duplicate titrations and the dashed line is the predicted titration curves obtained from applying the surface complexation model to the conditions of a suspension with 21 mg/L of nanoparticles as Fe_3O_4.

$\equiv SO^-$ species. In contrast, the OA-coated nanoparticles used in this study can only be neutral or deprotonated; consequently, we chose to use HCSITE to represent the neutral form of exposed functional groups at the nanomaterial surface and $CSITE^-$ for the negative deprotonated form. For inclusion in the SCM approach, the solid concentration was represented as the Fe_3O_4 in the nanoparticles. Surface site concentrations were calculated from surface area and site density, while both of these values along with the pK_a of HCSITE were determined by optimizing the fit of the model outputs to the experimentally determined titration curves (Figure 4.4). The best fit was determined as the one with the minimum sum of the squares of the

residuals between experimental and predicted data. The best fit value of pK_a for HCSITE was 5.2 (Reaction 1, Table 4.1). The calculated maximum oleic acid exposed functional group concentrations for 28 mg/L nanoparticles (as Fe_3O_4, used for adsorption experiments) was 78 μM from Li's calculated density of 1.32 mol of outer layer/mol Fe_3O_4, based on the assumption that the first layer and the second layer interacted with a 1:1 ratio (Li et al. 2016a). The surface site concentration obtained from optimizing the surface complexation model was determined on the optimized site density value and was 32 μM, which is lower than the calculated 78 μM for same amount of nanoparticles. This is probably because the ratio of the outer layer to the first layer on the nanoparticles was less than one; the exact ratio of the two layers remains imprecisely known.

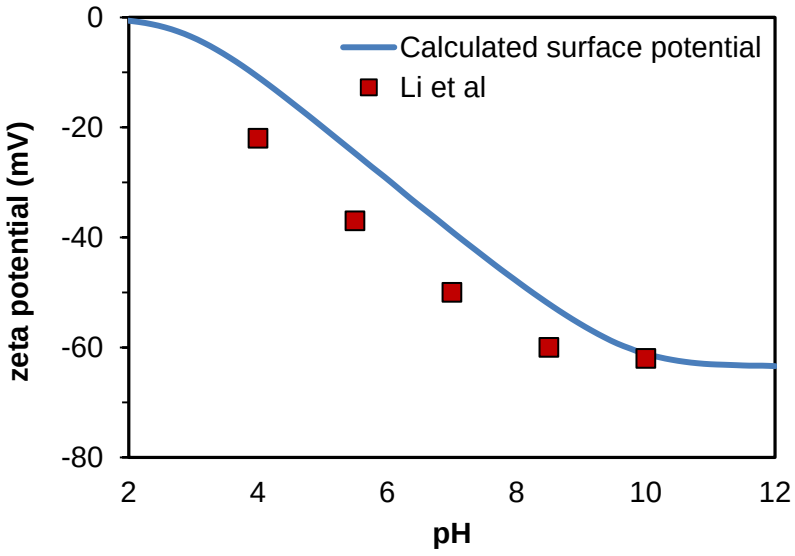

Figure 4.5. Points are the measured zeta potential data from Li. et al (2015)(Li et al. 2016a) and the line is the calculated surface potential when using the diffuse double layer model. The calculated potential was obtained by determining the equivalent charge density from SCM simulation and then applying the Gouy-Chapman equation (SI) to determine the surface potential. Parameters in the model are listed in Table 4.1.

Modeling parameters for the surface properties were furthered tested by comparing the calculated surface potential with the measured zeta potential of OA-coated nanoparticles. OA-coated nanoparticles were always negatively charged, and they become more negatively charged with increasing pH. An equivalent surface charge density could be obtained from the surface complexation model, which can then give the electrical potential in the diffuse plane (ψ_d) based on the Gouy-Chapman theory (see additional discussion in the Supporting Information). The trend with pH and the values of the calculated potentials were remarkably consistent with the zeta potentials that were measured for OA-coated nanoparticles over the pH range from 4 to 12 in a previous study (Figure 4.5) (Li et al. 2016a).

4.3.3.2 Surface complexation modeling for U(VI) adsorptions

Based on the estimated nanoparticle surface properties, the SCM can successfully simulate the adsorption edge data for U(VI) adsorption to OA-coated nanoparticles over a wide range of pH and total U(VI) concentrations under open or closed atmospheric conditions (Figure 4.3). The model development started with HCSITE concentration and the associated deprotonation constant determined from the acid-based titrations (Reaction 1). The next step was addition of reactions and optimization of their constants to fit the adsorption edge for data from experiments with no carbonate in the system. Three different surface complexation reactions (Reactions 2-4) were considered in this step. The model showed that combinations of either Reactions 2 and 4, Reactions 3 and 4 or Reactions 2, 3 and 4 could all fit the

carbonate-free experimental data well with different sets of log K values. As a result, initial estimates of log K values were obtained.

Table 4.1. Adsorption reactions with surface sites (HCSITE) (other aqueous reactions are included in the supporting information) and parameters in the surface complexation modeling were obtained from the optimal fitting result.

Reactions and Parameters		
Specific surface area: 180 m^2/g		
Site density: 3.82 sites/nm^2		
$HCSITE = CSITE^- + H^+$	$\log K_1$ = -5.20	Reaction 1
$UO_2^{2+} + H_2O - 2H^+ + HCSITE = CSITEUO_2OH$	$\log K_2$ = -5.65	Reaction 2
$UO_2^{2+} + 2H_2O - 3H^+ + HCSITE = CSITEUO_2OH_2^-$	$\log K_3$ = -9.35	Reaction 3
$UO_2^{2+} + 3H_2O - 4H^+ + HCSITE = CSITEUO_2OH_3^{2-}$	$\log K_4$ = -14.30	Reaction 4
$UO_2^{2+} + 2CO_3^{2-} - H^+ + HCSITE = CSITEUO_2(CO_3)_2^{3-}$	$\log K_5$ = 25.60	Reaction 5

The optimal set of reaction constants was then obtained by applying reactions to model the system that was equilibrated with the atmosphere with three U(VI) loadings as well as the carbonate-free system. The application of the first two combinations of reactions (Reactions 2 and 4 or Reactions 3 and 4) led to either overestimation or underestimation of adsorption at low or high pH conditions, respectively. Consequently, the implementation of all three reactions together could balance this situation but would again predict a decrease of adsorption at pH above approximately 8 that was much more dramatic than the actual observed decrease in adsorption. In order to account for more adsorption at higher pH, formation of a uranyl-carbonate ternary surface complex was included as Reaction 5; such a ternary surface complex has been found to be important to interpreting U(VI) adsorption to

other materials as well (Waite et al. 1994, Wang et al. 2012). When these four reactions were considered to fit four adsorption edges (three U(VI) loadings for open systems and one loading for a closed system), the optimal values for the reaction constants for Reactions 2, 3 4, and 5 were determined. The resulting optimal set of constants gives the minimum value of the sum of the square of the residuals between experimental and predicted data (Table 4.1), and the adsorption percentage for each of the four surface complexes is shown in Figure S2.2 (Supporting Information). With no carbonate in the system, the model predicts increased adsorption from pH 5 that remains at nearly 100% adsorption, even at higher pH values. For systems equilibrated with the atmosphere, the model predicts increasing U(VI) adsorption from pH 4.5 to 6, an adsorption plateau from pH 6 to 8.5 during which there was a slight decrease of adsorption percentage, and finally decreasing adsorption when pH was higher than 8.5.

The SCM was also used to predict the adsorption of U(VI) with increasing total U loadings at a fixed pH. Such an equilibrium relationship between adsorbed and dissolved uranium at a fixed pH and with increasing total U loadings is commonly interpreted using adsorption isotherm equations (e.g., Langmuir or Freundlich), but this behavior can also be predicted using an SCM. Data for comparison of the model predictions come from a recent study (see discussion in the Supporting Information) (Li et al. 2017). The model only agreed well with the data at the lowest U(VI) equilibrium concentrations (< 2 mg/L), which was only a small part of the total conditions examined in the previous study. With increasing U(VI) loadings, the difference between the experimental and predicted adsorption densities

began to increase. Potential causes for the difference could include U(VI) precipitation and U(VI) reduction in the previous study that increase the solid-associated uranium concentration but are not technically the result of U(VI) adsorption. At the high dissolved U(VI) concentrations in the previous study, the solution can become supersaturated with respect to U(VI) precipitates. In the previous experimental study, XANES spectra indicated partial U(VI) reduction to U(IV) at higher initial U(VI) loadings (6.1 μmol of U(VI)/mg of Fe_3O_4) than those in the experiments of this study (0.2 – 0.6 μmol of U(VI)/mg of Fe_3O_4) (Li et al. 2016c). As a result, with increasing U(VI) concentration, U(VI) reduction increasingly affects the uptake of U(VI) from solution to the nanoparticles.

4.4 Implications for U(VI) Separation using Engineered Nanoparticles

Engineered iron oxide nanoparticles are a promising material platform to separate U(VI) from the aqueous phase with easy application of relatively low magnetic fields. The modification of nanoparticle surfaces not only enables particle stability, but it also allows for enhanced adsorption capacity and affinity towards U(VI) as well as many other contaminants. The studied OA-, SA- and ODP-coated nanoparticles all possess high adsorption affinity for U(VI) over a wide pH range. The surface complexation modeling approach that has commonly been applied to interpret U(VI) adsorption to minerals can also be used to interpret U(VI) adsorption to engineered sorbents. The model framework developed in this study enables the implementation

of a double-layer model with a new type of surface site that corresponds to exposed functional groups on the engineered nanoparticles. The model represents the properties of surface coated nanoparticles (acid-base behavior and zeta potential) and can simulate U(VI) adsorption under various, environmentally relevant aqueous conditions. Predictable adsorption behavior is a key step towards optimized design and operation of material-based treatment processes and conditions for U(VI) removal. Both experimental and modeling work provide insight into the adsorption process that benefit the application of engineered nanoparticles for metal removal from water.

Acknowledgements

This work was supported by the National Science Foundation (NSF) (CBET, Award #1437820). TEM, DLS, ultracentrifugation, and ICP-MS measurements were performed in the Nano Research Facility (NRF) at Washington University in St. Louis, a member of the National Nanotechnology Infrastructure Network (NNIN), which is supported by the NSF (#ECS-0335765).

Chapter 4. Supporting Information

Supporting information contains aqueous reactions considered in the surface complexation modeling, surface charge density calculation, comparison of U(VI) adsorption when closed, partially and completely equilibrated with atmosphere, simulation of adsorption isotherm with OA-coated nanoparticles by surface complexation modeling and adsorption percentage of each surface associated U(VI) species in the surface complexation model in one adsorption edge. The supporting information also includes the results of a set of U(VI) adsorption experiments with CTAB-coated magnetite nanoparticles.

Surface charge density calculation and the Gouy-Chapman equation.

$$\sigma_d = \frac{[Coul]\cdot F}{S\cdot SA} \qquad \text{Equation S1}$$

$$\sigma_d = -0.1174 {C_s}^{0.5} sinh \frac{zF\psi_d}{2RT} \qquad \text{Equation S2}$$

Symbol	Meaning
σ_d	equivalent charge density (C/m^2)
[Coul]	coul concentration from the model simulation (mol/L)
F	Faraday constant (C/mol)
S	solid concentration (g/L)
SA	Specific surface area (m^2/g)
C_s	electrolyte concentration (mol/L)
z	absolute value of the ionic charge number of the electrolyte ions
ψ_d	electrical potential in the d plane (V)
R	gas constant (J/mol-K)
T	temperature (K)

Comparison of U(VI) Adsorption among CO_2-free Conditions, Partially Air-equilibrated and Fully Air-equilibrated Systems

For adsorption experiments in Figure 2 of the main manuscript, adsorption reactors (test tubes) were opened and bubbled with air for approximately 20 minutes, and the adsorption percentage at high pH conditions were shown as red squares in Figure 2 of the main manuscript and Figure S1 below. For high pH conditions, it was hard to reach the target pH values by air-bubbling alone. As a result, in order to make sure the system completely reached air-water equilibrium, $NaHCO_3/Na_2CO_3$ was added as described in the Methods section. In these systems, the results at these more fully equilibrated conditions are those presented in Figure 3 of the main manuscript. Adsorption with same initial loadings of U(VI) to OA-coated nanoparticles and different extents of equilibration with atmospheric CO_2 are compared in Figure S4.1. The comparison illustrates that with less inorganic carbon in the system, more U(VI) adsorption occurred, especially for pH higher than 8.

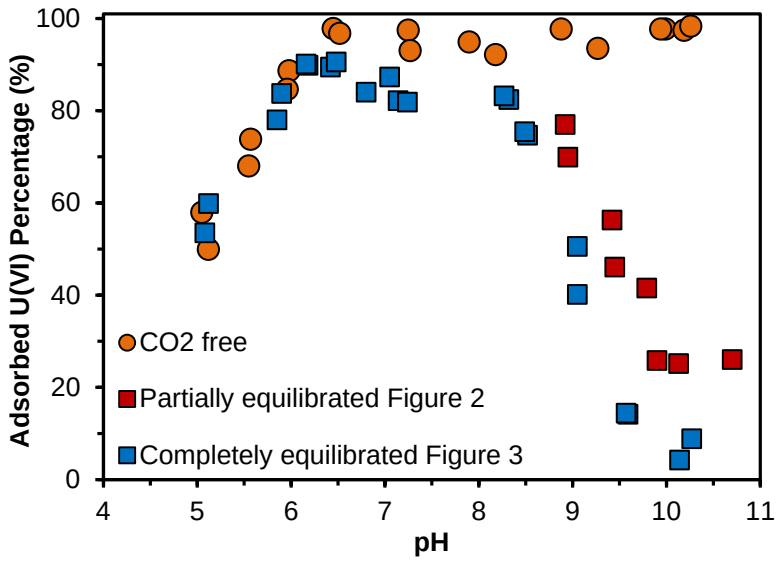

Figure S4.1. Percentage of U(VI) adsorbed to OA-coated iron oxide nanoparticles (9.4 μM total U(VI), 28 mg/L as Fe_3O_4). ○ in orange: U(VI) in CO_2 free system (Figure 3 in the manuscript); □ in red: open to the atmosphere (Figure 2 in the manuscript); □ in blue: open to the atmosphere (Figure 3 in the manuscript).

Comparison of Surface Complexation Model Results to U(VI) Adsorption Isotherm for 8 nm Oleic Acid-coated Nanoparticles

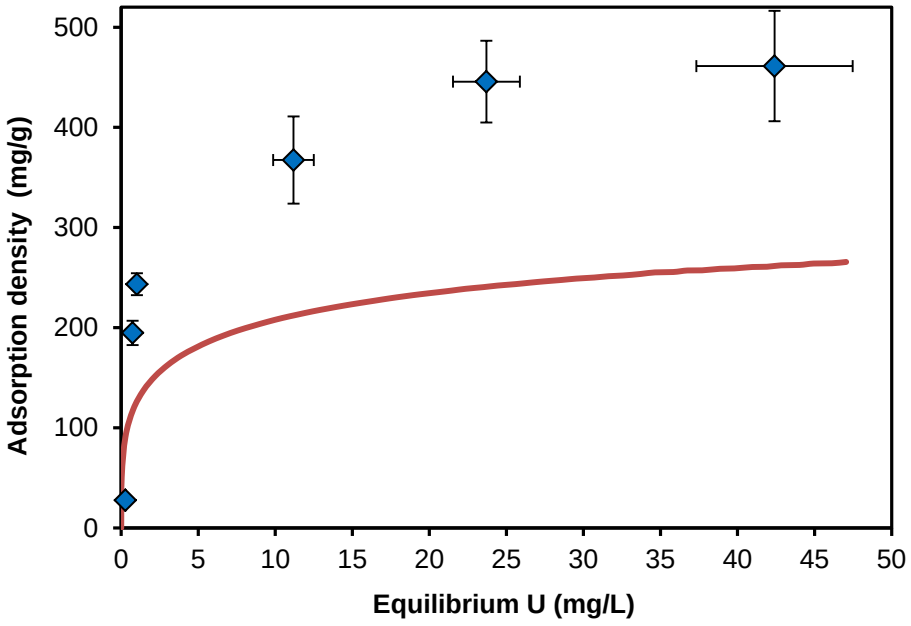

Figure S4.2. Relationship between equilibrium adsorbed and dissolved U(VI) at pH 7. ◊: experimental data from previous study to 8 nm oleic acid-coated nanoparticles;(Li et al. 2017) —: output of surface complexation model developed in this study. The model was developed by examining the pH dependence of U(VI) adsorption at relatively low total U(VI) loadings relative to the experimental data presented here.

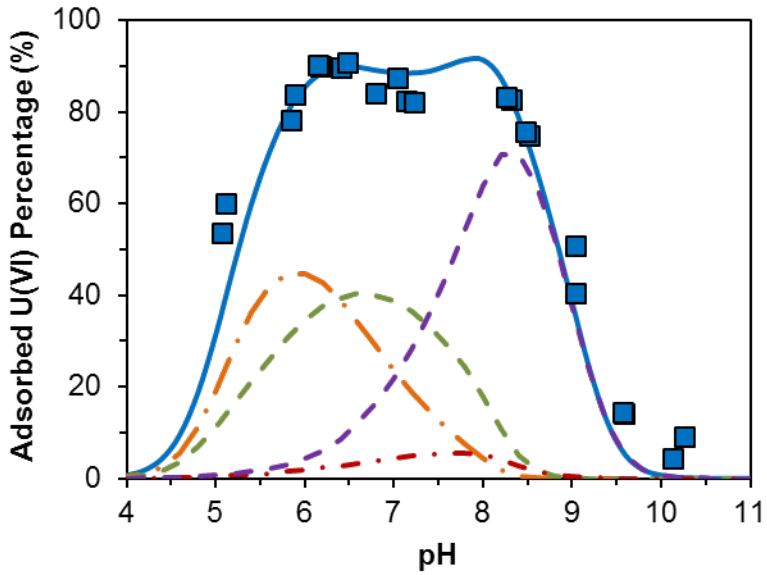

Figure S4.3. Modeled speciation of surface complexes using the surface complexation model for mid-U(VI) loadings for the system equilibrated with the atmosphere. Dashed lines represent percentages of U(VI) present in individual surface complexes. —· (orange): $CSITEUO_2OH$, — — (green): $CSITEUO_2OH_2^-$, — · — (red): $CSITEUO_2OH_3^{2-}$, — — (purple): $CSITEUO_2(CO_3)_2^{3-}$. The solid line is the summation of the four individual surface complexes and represents the total U(VI) that is adsorbed.

U(VI) Adsorption to CTAB-coated Magnetite Nanoparticles.

Trimethyloctadecylammonium bromide (CTAB) coated magnetite nanoparticles have a surface that is positively charged. Adsorption affinity to either positively charged or negatively charged nanoparticles depends on the dominant aqueous U(VI) species over certain pH range. Adsorption percentages of U(VI) adsorption to CTAB-coated nanoparticles were surprisingly identical to that have been observed for OA-coated nanoparticles. Less adsorption was observed at lower pH range (pH 5~6) because the uranyl hydroxide species are the dominant forms and would have more adsorption on negatively charged OA-coated nanoparticles. Due to the observed aggregation at pH higher than 7.0, adsorption experiments for CTAB-coated nanoparticles were only performed at low pH conditions (5.0 to 7.0).

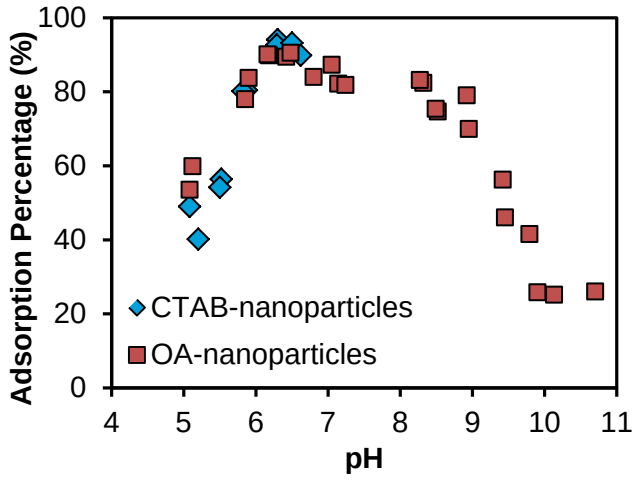

Figure S4.4. Percentage of U(VI) adsorbed to CTAB- and OA-coated iron oxide nanoparticles (9.4 μM total U(VI), 28 mg/L as Fe_3O_4).

Chapter 5. Cr(VI) Adsorption to Engineered Iron Oxide Nanoparticles: Impact of Water Chemistry and Surface Complexation Modeling

Results of this Chapter are in preparation for submission to *Environmental Science: Nano.*

Abstract

Surface-functionalized magnetite nanoparticles are promising adsorbents due to the large surface area and the ease of separation after contamination removal. Amine-functionalized nanoparticles (trimethyloctadecylammonium bromide, CTAB) possess higher Cr(VI) adsorption affinity than nanoparticles with carboxyl groups (Stearic acid, SA), due to the strong electrostatic interactions between opposite charges. The adsorption of Cr(VI) by CTAB- and SA-coated nanoparticles decreased with increasing pH values (4.5 to 10). For CTAB-coated nanoparticles, an increase of initial Cr(VI) loadings led to lower adsorption percentages. A surface complexation model could successfully simulate Cr(VI) adsorption in $NaNO_3$ solutions over a broad range of pH and Cr(VI) loadings with a small set of

adsorption reactions. The application of nanoparticles was tested with the presence of two drinking water supplies, and decreases in Cr(VI) adsorption were associated with the presence of Ca^{2+}. When the Ca^{2+} concentration increased from 0 to 3.3 mM, adsorption decreased. Because only slight aggregation was associated with Ca^{2+} and an observed increase in zeta potential with Ca^{2+} addition should actually enhance Cr(VI) adsorption, the causes of inhibition of Cr(VI) by Ca^{2+} are not associated with particle size or surface charge. Instead it is likely that Ca^{2+} influences the structure of the organic bilayer on the nanoparticle surfaces in a way that decreased the availability of surface sites.

5.1 Introduction

The presence of chromium(VI) in the environment is a serious public health concern (Langrrd 1990, Peterson-Roth et al. 2005). In the two oxidation states of chromium, Cr(VI) is soluble and has toxic and carcinogenic effects while Cr(III) is less toxic and less soluble. The current U.S. drinking water standard for total chromium is 100 μg/L (U.S. 1985). However, California has a new regulation specifically for Cr(VI) with a maximum contaminant level (MCL) of 10 μg/L (2016). Cr(VI) removal from aqueous phases has been studied through many chemical and physical treatment processes and the removal efficiency can be largely affected by the pH-dependence of chromium speciation (Olazabal et al. 1997, Pan et al. 2016a, Zachara et al. 1987).

Iron oxide-based materials have received high attention for the removal of heavy metals from aqueous phase due to their high surface area and reactivity (Johnston and Chrysochoou 2012, Zachara et al. 1987, Zeng et al. 2008). Nanoscale iron oxides have been applied to investigate the adsorption of many types of heavy metals (Xu et al. 2012, Zeng et al. 2009). Although high adsorption capacities have been reported, the aggregation of these bare nanoparticles remains as an issue that disturbs the stability of nanoparticles in aqueous phases and reduces their effective surface area and reactivity (Wang et al. 2013). Iron-oxide nanoparticles surfaces can be modified with a variety of materials (humic acid, polymers and fatty acids) (Ge et al. 2015, Jiang et al. 2014) that can stabilize nanoparticles while maintaining the ability to remove metal contaminants (U(VI), Cu(VI) and Cr(VI)) (Hao et al. 2010, Lee et al. 2015a, Li et al. 2016a, Wang et al. 2015). U(VI) removal has been widely studied by fatty acids coated magnetite nanoparticles from a same synthesis process.

Humic-acid coated magnetite can adsorb Cr(VI), and the humic acid was also responsible for Cr(VI) reduction to Cr(III) (Jiang et al. 2014). Bare magnetite has been studied for Cr(VI) removal and significant of Cr(VI) reduction was observed. However, the extent to which this reduction will occur for surface-modified nanoparticles has not been explored. The application of superparamagnetic engineered nanoparticles enables the separation by magnetic field after adsorbing metals (Singh et al. 2011, Yavuz et al. 2006). NH_2-functionalized nanomagnetic polymer adsorbents (NH_2-NMPs) have been studied for Cr(VI) removal that had adsorption mechanisms as electrostatic attraction, ion exchange and coordination interactions (Zhao et al. 2010).

Cr(VI) adsorption to engineered magnetite nanoparticles coated with organic acids have not previously been evaluated with respect to systematic variation in the water chemistry. Such an evaluation can consider the impact of water chemistry on particle stability and surface properties, and it can be integrated with an equilibrium adsorption modeling approach. For metal adsorption to inorganic solids, surface complexation modeling (SCM) has successfully simulated adsorption by considering the relevant interfacial interactions, including a set of aqueous and surface reactions and the consideration of electrostatic interactions between solutes and surfaces, to predict adsorption over a broad range of conditions. Many SCMs have been developed to simulate metal adsorption to various adsorbents. Cr(VI) adsorption to $MnFe_2O_4$ has been modeled by introducing $\equiv MeOH_2^+$ as the hydroxylated surface site for pH from 2 to 6.5, as the surface site only remained positively charged below the pH_{pzc} (Hu et al. 2005). In other adsorption systems such as carbonaceous

nanofibers and multiwalled carbon nanotubes, carboxyl and hydroxyl groups were considered as the dominant two adsorption sites towards U(VI) and Cr(VI) (Hu et al. 2009, Zhang et al. 2015).

While developing novel materials for metal removal, the stability and treatment efficiency of the material needs to be tested in real water systems. Of particular concern is the potential for nanoparticle suspensions to become destabilized and for nanoparticles to aggregate such that their effective surface area is greatly reduced. Aggregation of oleic acid-coated nanoparticles by Na^{+} and Ca^{2+} has been reported with critical coagulation concentrations at 710 mM and 10.6 mM at pH 7.2, (Li et al. 2014) which are high concentrations relative to those that will be encountered in drinking water treatment. Ca^{2+} has a bridging effect that can bind two adjacent carboxyl groups, which affect nanoparticle behavior (Chowdhury et al. 2014, Li et al. 2014). In a previous study with a natural water with dissolved Ca^{2+} and Mg^{2+}, these solutes did not influence Cu^{2+} removal by MNP-NH_2 (Hao et al. 2010). However, the impact of cations/anions on Cr(VI) adsorption to CTAB-coated nanoparticles remains unknown as Cr(VI) is present as anionic forms that may respond differently.

Nanoparticles coated with various organic acids have been synthesized through ligand addition methods with controlled size. In this study, SA and CTAB-coated nanoparticles were chosen to investigate the impact of water chemistry on Cr(VI) from the aqueous phase. The objectives of the present study were to (1) identify the impact of water chemistry on Cr(VI) adsorption to nanoparticles coated with two types of surface organic acids, (2) develop a reaction-based model that

could interpret the observed effects of water chemistry, and (3) evaluate nanoparticle adsorption performance with two more complex and realistic drinking water sources.

5.2 Experimental

5.2.1 Materials

Iron oxide (Iron III, hydrated, catalyst grade), 1-octadecene (technical grade, 90%), oleic acid (OA, 99.0%), stearic acid (SA, 99.0%), trimethyloctadecylammonium bromide (CTAB, 99.0%), sodium hydroxide (ACS reagent, 99.0%) and nitric acid (trace metal grade) were purchased from Sigma-Aldrich. Synthetic groundwater with a target pH of 7.50 was prepared according to a previous study to represent the composition of in Glendale, California, where researches have evaluated other Cr(VI) removal technologies (SI) (Pan et al. 2016a). Reagent grade hexane, acetone, and ethanol were also purchased from Sigma-Aldrich and used without purification.

5.2.2 Nanoparticle Synthesis and Phase Transfer

We used a thermal decomposition method to synthesize iron oxide nanoparticles and purify nanoparticle suspensions to obtain the stock suspensions of nanoparticles in hexane (Li et al. 2016a). After the thermal decomposition process, the carboxylic functional group of oleic acid reacted onto the surface of the magnetite nanoparticles, exposing the hydrophobic tail that enables nanoparticles to be dispersed in hexane. These iron oxide nanoparticles are monodispersed with an average size of 8 nm

according to imaging by transmission electron microscopy (TEM, FEI Tecnai G2 Spirit).

Nanoparticles in hexane solution needs to be phase transferred into the aqueous phase by attaching a second layer of desired functional groups for assessing Cr(VI) adsorption and the phase transfer procedure was described in previous studies (Li et al. 2016a, Li et al. 2016b). The addition of a second layer of organic acids led to surface passivation, with the hydrophilic tail of the second layer exposed to the water, which allows the nanoparticles to be transferred from hexane to water. Stearic acid (SA) and trimethyloctadecylammonium bromide (CTAB) were used as the second layer organic acids. Nanoparticles in hexane (1~2 mL) were mixed with 8 mL of SA (5 mM) or CTAB (10 mM) solutions in ultrapure water (resistivity > 18.2 MΩ-cm). The probe of a sonicator (UP 50H, Dr. Hielscher, GMHB) was placed between the two phases, and the mixture was sonicated under 70-75% amplitude for 5 min to introduce nanoparticles from hexane to the water. As a result, the surface of bi-layer nanoparticles were either negatively charged or positively charged, due to the different surface functional groups exposing outwards. Suspensions with transformed nanoparticles were washed by ultrapure water through ultrafiltration cellulose membranes (100 kDa MWCO) five times and filtered through a syringe filter (pore size of 0.2 μm, Millipore) to obtain the stock suspensions of nanoparticles for use in adsorption experiments.

5.2.3 Cr(VI) Adsorption Experiments

Batch experiments of Cr(VI) adsorption to surface functionalized nanoparticles were studied with various water chemistry. A Cr(VI) stock solution of 500 mg/L (9.62 mM) were prepared by dissolving 0.142 g of potassium dichromate ($K_2Cr_2O_7$) solids in 100 mL ultrapure water. Nanoparticle stock suspensions and Cr(VI) stock solution were added into a 200-mL beaker to achieve a nanoparticle dose of 28 mg/L as Fe_3O_4 and target initial Cr(VI) loadings (5.8, 10.5 and 16.5 μM). The suspensions were bubbled by air for 5 min to equilibrate them with air before being distributed into separate reactors to be adjusted to target pH values by 0.1 M NaOH and 0.1 N HNO_3. The ionic strength was controlled to be close to 0.01 M. Application of CTAB-coated nanoparticles was also tested in St. Louis tap water with pH adjusted to 6 and 9 and Glendale groundwater at pH 7.5 with 10.5 μM Cr(VI). In order to study the impact of Ca^{2+} on Cr(VI) adsorption, mixture suspensions were prepared in 3.3 mM $Ca(NO_3)_2$ solutions from pH 4.5 to 9. The impact of Ca^{2+} was also investigated by increasing Ca^{2+} concentration from 0.03 mM to 3.3 mM at pH ~7.50. All suspensions were mixed by end-over-end rotation for 24 hours, and the pH was periodically monitored and readjusted to be close to target values. After this 24-equilibration period, nanoparticles were separated from the suspension by ultracentrifugation at 45,000 rpm for 2 hours. The supernatants were collected and preserved in 1% HNO_3 for elemental analysis. Adsorption kinetics were examined with duplicate suspensions at an initial Cr(VI) concentration of 10.5 μM with 28 mg/L of nanoparticles as Fe_3O_4. Aliquots (8 mL) of the suspension were taken after 0.5, 2.5, 4.5, 8 and 24 hours and then immediately separated by ultracentrifugation for chemical analysis.

5.2.4 Nanoparticle characterization and dissolved Cr(VI) measurement

Hydrodynamic diameters of CTAB-coated nanoparticles with the addition of various Ca^{2+} concentrations at pH 7.5 and surface charges of CTAB-coated nanoparticles from pH 5 to 10 were measured by dynamic light scattering (Zetasizer, Malvern Nano ZS, UK) of duplicate samples. For hydrodynamic diameter measurement, a certain amount of nanoparticle stock suspension was added into ultrapure water in a test tube and the pH was adjusted to 7.5 ± 0.2. Then 1 mL suspension was transferred into a vial, followed by addition of small amounts of concentrated $Ca(NO_3)_2$ solution. These additions created a suspension with 1 mg/L (as Fe_3O_4) of nanoparticles and Ca^{2+} concentrations at target levels that correspond the values in adsorption experiments. For zeta potential measurement, nanoparticle suspensions were prepared with the pH being adjusted and immediately placed in the DLS measurement chamber after a short time of vortex-mixing.

Dissolved Cr and Fe concentrations in supernatants were analyzed by ICP-MS (PerkinElmer). A control experiment in a previous study indicated that ultracentrifugation effectively separated the nanoparticles from the suspension and no Fe was detected in supernatants. Duplicate samples (200 µL) of the initial suspension (nanoparticles and Cr mixture) in adsorption experiments were digested in hot concentrated nitric acid, and the resulting Cr(VI) concentration and

nanoparticle loadings (Fe) were in excellent agreement with the expected initial loadings.

5.2.5 Surface Complexation Modeling (SCM)

SCM was applied to simulate Cr(VI) adsorption to CTAB-coated nanoparticles over a wide range of pH and with three different initial Cr(VI) loadings. The modeling was developed in MINEQL+ V5.0 with a diffuse double-layer model being implemented. All aqueous reactions were considered as shown in the supporting information.

5.3 Results and Discussion

5.3.1 Batch Adsorption Experiments

Cr(VI) adsorption to SA- and CTAB-coated nanoparticles demonstrated different features over wide pH conditions. Over all pH conditions, Cr(VI) adsorption more to CTAB-coated nanoparticles than to SA-coated nanoparticles (Figure 5.1), which is consistent with expectations based on surface charges. The CTAB-coated nanoparticles are positively charged due to the amine functional groups (Figure 5.3) and SA-coated nanoparticles were negatively charged because of carboxylic groups. As Cr(VI) exists as the anions $HCrO_4^-$ and CrO_4^{2-} over the studied pH conditions, its adsorption was more favorable to CTAB-coated nanoparticles. For a given initial Cr(VI) loading, the extent of Cr(VI) adsorption to CTAB-coated nanoparticles

decreased with increasing pH. This trend is because the surface of CTAB-coated nanoparticles became less positively charged with increasing pH, leading to less adsorption affinity towards Cr(VI) species (Figure 5.3). Measured zeta potential decreased with increasing pH, which were consistent with a trend and in the same range of values as in a previous study (Li et al. 2016a). For SA-coated nanoparticles, there was also a trend of decreasing adsorption with increasing pH. It has been observed that Cr(VI) adsorption to $MnFe_2O_4$ decreased from pH 2 to pH 10 due to a more negatively-charged surface with increasing pH as the deprotonation of surface hydroxyl groups (Hu et al. 2005). Cr(VI) adsorption to surface functionalized nanoparticles (TEPA and NH_2 as the surface coatings) also showed decreased adsorption affinity when pH increased (Zhao et al. 2010). With increasing initial Cr(VI) loading, the percent of Cr(VI) adsorbed at equilibrium for a given pH decreased. The decrease was larger when pH was higher than 7.

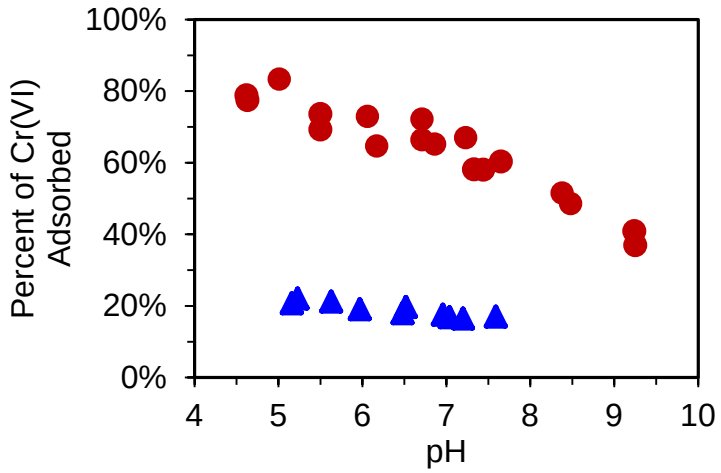

Figure 5.1. Percentage of Cr(VI) adsorbed to SA- (Δ) and CTAB- (○) coated NPs (28 mg/L as Fe_3O_4) with Cr(VI) initial loadings of 10.5 µM after 24 hours of equilibration in 0.01 M $NaNO_3$ solution.

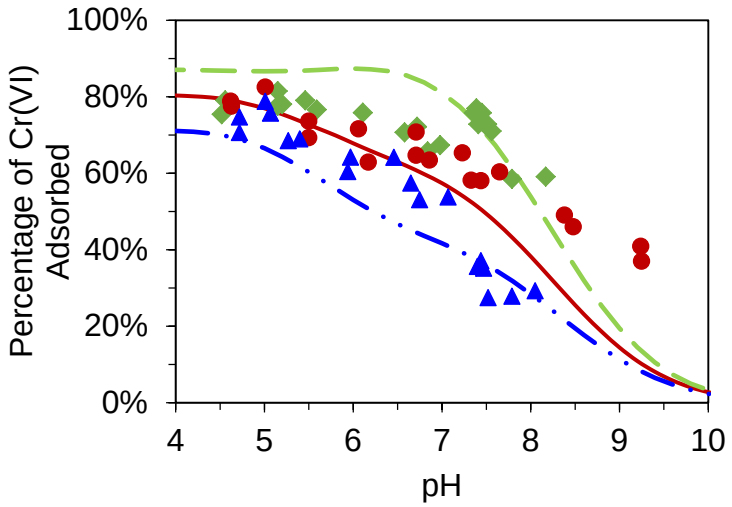

Figure 5.2. Percentage of Cr(VI) adsorbed to CTAB-coated NPs (28 mg/L as Fe_3O_4) with Cr(VI) initial loadings of 5.8 (◊), 10.5 (○) and 16.5 (Δ) μM in 0.01 M $NaNO_3$ solution after 24 hours. Points are the experiment results and smooth lines are the simulation results from SCM.

Adsorption was considered as the main mechanism for Cr(VI) uptake by fatty acids coated magnetite nanoparticles. The interaction between Cr(VI) and nanoparticles was mainly considered as chemical binding as amino and carboxyl groups have been reported to chelate with heavy metals (Singh et al. 2011, Zhang et al. 2012). Cr(VI) has been studied to be adsorbed by humic-acid coated nanoparticles. The reduction of Cr(VI) to Cr(III) occurred by the humic acid, and Cr(VI) could not diffuse through the humic acid layer to reach the surface of the magnetite core (Jiang et al. 2014). At low Cr(VI) loadings, most Cr(VI) was adsorbed to surface functional groups and would not be able to diffuse through organic layers and be reduced by magnetite core. After adsorption experiments, Cr-contained nanoparticles were dried and characterized by XPS (spectra not shown here). However, due to the noisy background signal from organic coatings from the spectra, no reduction was able to

be detected at low Cr loadings. As a result, reduction was not considered to occur by either the surface coatings or the magnetite cores. Adsorption was considered as the dominant mechanism to account for Cr(VI) removal.

5.3.2 Surface Complexation Model

A SCM was developed for Cr(VI) adsorption to CTAB-coated nanoparticles with the consideration of water chemistry. In most SCMs, an amphoteric surface hydroxyl (≡SOH) is usually used to represent the surface site for a double-layer model to predict interactions between metals and mineral surfaces (such as goethite and ferrihydrite). For the CTAB-coated nanoparticles, the functional group can be either positive or neutral but not negative, so the component CTABOH was introduced into the model to represent the neutral form of the surface functional groups while $CTAB^+$ represents the positively charged surface site. The development of SCM started by simulating surface properties (surface potential) as a function of pH. The pK_a values for organic acids with amine groups have been reported to vary from 9.8 to 10.7, based on the number of hydrogens of ammonia that are replaced by organic groups (Bauld 2005) and 24 tertiary amine absorbents have been screened, most of which have pK_a values from 9 to 10 (Chowdhury et al. 2013). The pK_a of 9.8 was used as the protonation constant for Reaction 1 in the model (Table 5.1). An additional two parameters, specific surface area and surface site density, need to be obtained for determining the total surface site concentrations.

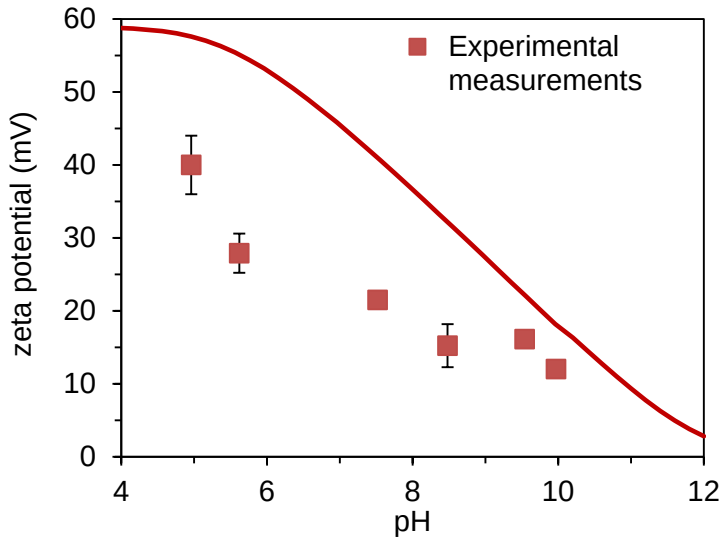

Figure 5.3. Measured zeta potential (points) compared with the calculated surface potential. The calculated potential was obtained by calculating the equivalent charge density from SCM simulation and using the Gouy-Champ equation to determine the surface potential.

From the surface complexation model, an equivalent surface charge density could be obtained that can be used to calculate the electrical potential in the diffuse plane (ψ_d) based on the Gouy-Chapman theory (Equation 1, SI). Optimization of both parameters was based on fitting of the model simulation to zeta potential measurements to achieve the minimum square difference of between the modeling results and the experiment data (Table 5.1). Based on a previous study, the concentration of surface organic acids have been calculated as mol of organic acids/mol of Fe. The surface site concentration in our study was in the range of this number. The difference was due to the unclear about the exact connections between the first and second layers. In a previous study, zeta potentials of oleic acid-coated nanoparticles from pH 4 to 10 have been well-predicted by a surface complexation model. The modeling result in this study was not in fully agreement with the

experimental data but it could predict the decreasing trend of the surface charge when pH increased (Figure 5.3).

Table 5.1. Adsorption reactions with surface sites (CTABOH) and parameters in the surface complexation modeling were obtained from the optimal fitting result. (other aqueous reactions are included in the supporting information)

Reactions and Parameters		
Specific surface area: 147 m^2/g		
Site density: 3.66 sites/nm^2		
$CTABOH + H^+ = CTAB^+ + H_2O$	$\log K_1 = 9.8$	Reaction 1
$CTABOH + 2H^+ + CrO_4^{2-} = CTABHCrO_4 + H_2O$	$\log K_2 = 18.3$	Reaction 2
$CTABOH + H^+ + CrO_4^{2-} = CTABCrO_4^- + H_2O$	$\log K_3 = 9.2$	Reaction 3
$CTABOH + CrO_4^{2-} = CTABOHCrO_4^{2-}$	$\log K_3 = 1.1$	Reaction 4

Three adsorption reactions added to the model to successfully simulated adsorption at three Cr(VI) initial loadings for pH from 4.5 to 10. $HCrO_4^-$ and CrO_4^{2-} are usually included as the adsorbed species because they are the dominant Cr(VI) aqueous forms (Hu et al. 2005, Zachara et al. 1987). Adsorption reactions for $HCrO_4^-$ and CrO_4^{2-} to $CTAB^+$ were implemented in a preliminary model, but did not describe the experiment results well, especially at high pH conditions. As a result, CrO_4^{2-} adsorption to $CTAB^+$ was added into the modeling. Equilibrium constants for adsorption reactions were determined based on the fitting to the experimental data, and the optimal set leads to the minimum summation of the square of the residuals between experimental and predicted data (Table 1). The model could capture most adsorption features over all of the studied pH conditions.

5.3.3 Impact of Tap water and Glendale Water

In addition to the pH and Cr(VI) loadings, the application of nanoparticles was found to be affected by the presence of Ca^{2+} in the aqueous phase. The first indication of an effect of Ca^{2+} came in experiments with more complex water sources to which Cr(VI) was added to the same concentrations as in the experiments with simpler $NaNO_3$ solutions. For pH 9 Cr(VI) adsorption was 40% in a simple solution and 10% in St. Louis tap water, and at pH 6.5 adsorption was 70% in the simple solution and 40% in the tap water. The Cr(VI) adsorption percentage in Glendale groundwater was 20% at pH 7.5, which was again lower than the value of 60% in the simple solution at the same pH.

Because Ca^{2+} was a major constituent in the St. Louis tap water and Glendale water that was not present in the simpler solutions, we tested for its impact on Cr(VI) adsorption. A $Ca(NO_3)_2$ solution of 3.3 mM was added into the system, it had the same ionic strength as the simple system with 0.01 M $NaNO_3$, and achieved the same hardness as in Glendale groundwater. The addition of $Ca(NO_3)_2$ significantly decreased the adsorption to 5-20% over the whole pH range. Previous studies have demonstrated that Ca^{2+} can induce the aggregation of surface-functionalized nanoparticles that have negatively charged surfaces from coatings with lauric acid, oleic acid and sodium dodecyl sulfate (Li et al. 2016a, Li et al. 2014). The aggregation of nanoparticles would reduce the exposed surface sites and inhibit adsorption. However, the impact of cations on the aggregation of positively charged nanoparticles like the CTAB-coated ones studied here would not be expected to be

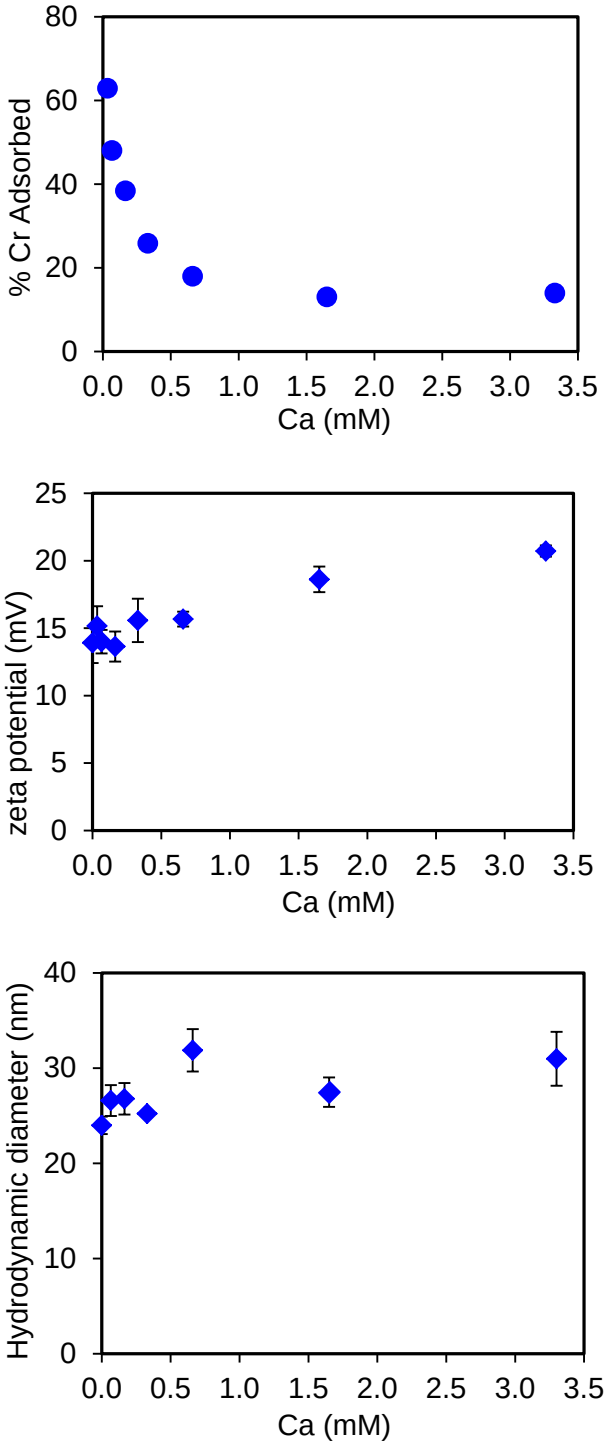

Figure 5.4. Adsorption of Cr(VI) to CTAB-coated NPs with increasing Ca addition (Cr(VI) initial loadings of 10.5 µM); Measurement of the zeta potential of the nanoparticles with certain Ca addition.

significant. The anions in these experiments were NO_3^-, which did not affect the adsorption of Cr(VI) according to the results from the addition of 0.01 M $NaNO_3$. The inhibition of $Ca(NO_3)_2$ on Cr(VI) adsorption was due to the presence of Ca^{2+} and not just to the increase in ionic strength A negligible effect of Ca^{2+} (up to 50 mg/L) has been reported on chromium removal by ferrous iron.(Dong et al. 2011) The co-occurrence of Ca^{2+} and Mg^{2+} had no effect on Cu^{2+} removal by 1,6-hexadiamine functionalized Fe_3O_4 nanoparticles (Hao et al. 2010).

With increasing Ca^{2+} concentrations from to 0.03 to 3.3 mM at pH 7.5, (Cr(VI) adsorption decreased (Figure 5.4). The adsorption percentage was ~63% for the lowest Ca^{2+} addition and was close to ~58% in simple system. The surface properties of the nanoparticles did not change significantly in terms of the surface charge and hydrodynamic diameter. The zeta potential of nanoparticle suspensions at pH 7.5 increased from 14 to 20 mV and the hydrodynamic diameter increased from 24 to 30 nm, with Ca^{2+}. After adsorption experiments, nanoparticle suspensions with the presence of Cr(VI) and Ca^{2+} were measured for the hydrodynamic diameter, which remained at ~30 nm. This was consistent with previous studies where no significant impact was observed for Ca^{2+} on positively charged nanoparticles at this level of concentrations since the Ca^{2+} CCC is 11.1 mM for C_{12}TAB-coated nanoparticles. CTAB in this study has 18 carbons in the long chain, which might yield a slightly different CCC. According to the zeta potential and hydrodynamic diameter measurements, decreasing adsorption would not be due to the decreased available surface sites resulted from aggregation. A previous study found that the presence of Ca^{2+} might lead to the formation of passivating $CaCO_3$, which could

result in a decreased Cr(VI) adsorption capacity by zero-valent iron (Liu et al. 2009b). The formation of $CaCO_3$ precipitation could probably block surface sites and affect the adsorption process. However, precipitation of $CaCO_3$ was excluded in this system. Based on the assumption that inorganic carbonate was equilibrated with the atmosphere, the solubility of Ca^{2+} in terms of $CaCO_3$ is shown in SI of this chapter. Ca^{2+} concentrations in the supernatant after adsorption experiments were measured and remained identical to the initial concentrations. All concentrations were far away from saturation conditions, indicating the low possibility of $CaCO_3$ precipitation.

The observations just discussed indicate that the effect of Ca^{2+} on Cr(VI) adsorption is not due to induced aggregation, modified surface charge, or coating by a $CaCO_3$ precipitate. In the absence of these phenomena affecting Cr(VI) adsorption, the exact cause remains unclear. One possibility that could warrant further investigation is that the Ca^{2+} could have influenced the structure of the CTAB organic coating in a way that altered the availability of functional groups that could adsorb Cr(VI).

5.4 Conclusions

CTAB-coated NPs can be effective adsorbents for anionic contaminants that include As(V) and Se(VI) in addition to Cr(VI) due to favorable electrostatic interactions between positively charged adsorbates and negatively charged aqueous species. Surface complexation models can be developed to predict the trend of surface charges under different pH conditions and simulate Cr(VI) adsorption with a

relatively simple set of aqueous reactions. Predictable adsorption behavior benefits future application of nanoparticles in the water treatment system because adsorption performance can be assessed with the model over broader ranges than could be experimentally evaluated. However, the application of the material-based treatment processes needs more consideration of its stability and treatment performance in real water resources. The performance of nanoparticles was inhibited by the Ca^{2+} in St. Louis tap water and Glendale groundwater. Although there are remaining questions about mechanisms of the impact from Ca^{2+}, the inhibition of Cr(VI) adsorption to the CTAB-coated nanoparticles occurs without causing nanoparticle aggregation, carbonate precipitate coating, or reversal of surface charge.

Acknowledgements

This work was supported by the National Science Foundation (NSF) (CBET, Award #1437820). The analysis of nanoparticles, including DLS, ultracentrifugation, and ICP-MS measurements were performed in the Nano Research Facility (NRF) at Washington University in St. Louis, a member of the National Nanotechnology Infrastructure Network (NNIN) that was supported by the NSF. XPS was conducted in the Institute of Materials Science & Engineering at Washington University in St. Louis.

Chapter 5. Supporting Information

Supporting information contains the Glendale groundwater composition, aqueous reactions in the surface complexation modeling, surface charge density calculation, and Ca solubility and concentration measurements.

Table S5.1. Glendale groundwater composition (Pan et al. 2016a).

Component	Concentration
alkalinity	215 mg/L as $CaCO_3$
chloride	68 mg/L
conductivity	885 µS/cm
hardness	326 mg/L as $CaCO_3$
nitrate	5.3 mg/L as N
pH	7.5
phosphate	0.25 mg/L as PO_4
silicate	27 mg/L as SiO_2
sulfate	220 mg/L as SO_4

Table S5.2. Aqueous Reactions Considered in the Surface Complexation Model

Reaction	log K*
$H_2O \rightleftharpoons H^+ + OH^-$	-14.00
$2CrO_4^{2-} + 2H^+ = Cr_2O_7^{2-} + H_2O$	14.56
$CrO_4^{2-} + H^+ = HCrO_4^-$	6.51
$CrO_4^{2-} + 2H^+ = H_2CrO_4$	6.419
$CrO_4^{2-} + Na^+ = NaCrO_4^-$	0.6960
$H^+ + {CO_3}^{2-} \rightleftharpoons {HCO_3}^-$	10.33
$2H^+ + {CO_3}^{2-} \rightleftharpoons H_2CO_3$	16.68
$Na^+ + H^+ + {CO_3}^{2-} \rightleftharpoons NaHCO_3$	10.079
$Na^+ + {CO_3}^{2-} \rightleftharpoons {NaCO_3}^-$	1.270
$Ca^{2+} + H_2O \rightleftharpoons CaOH^+ + H^+$	-12.697
$Ca^{2+} + H^+ + {CO_3}^{2-} \rightleftharpoons {CaHCO_3}^+$	11.599
$Ca^{2+} + {CO_3}^{2-} \rightleftharpoons CaCO_3(aq)$	3.2

* Source: MINEQL5.0 Database.

Surface charge density calculation and the Gouy-Chapman equation.(Benjamin 2014)

$$\sigma_d = \frac{[Coul]\cdot F}{S\cdot SA} \qquad \text{Equation S1}$$

$$\sigma_d = -0.1174 {C_s}^{0.5} sinh \frac{zF\psi_d}{2RT} \qquad \text{Equation S2}$$

Symbol	Meaning
σ_d	equivalent charge density (C/m^2)
[Coul]	coul concentration from the model simulation (mol/L)
F	Faraday constant (C/mol)
S	solid concentration (g/L)
SA	Specific surface area (m^2/g)
C_s	electrolyte concentration (mol/L)
z	absolute value of the ionic charge number of the electrolyte ions
ψ_d	electrical potential in the d plane (V)
R	gas constant (J/mol-K)
T	temperature (K)

The surface complexation model could predict the coul concentrations, which can be used to calculate σ_d from Equation S1. Substitute σ_d into the Equation S2 and ψ_d can be obtained, which represent the electrical potential in the d plane, and can be roughly considered as the zeta potential on the surface of solids.

Ca solubility and Ca concentration measurements

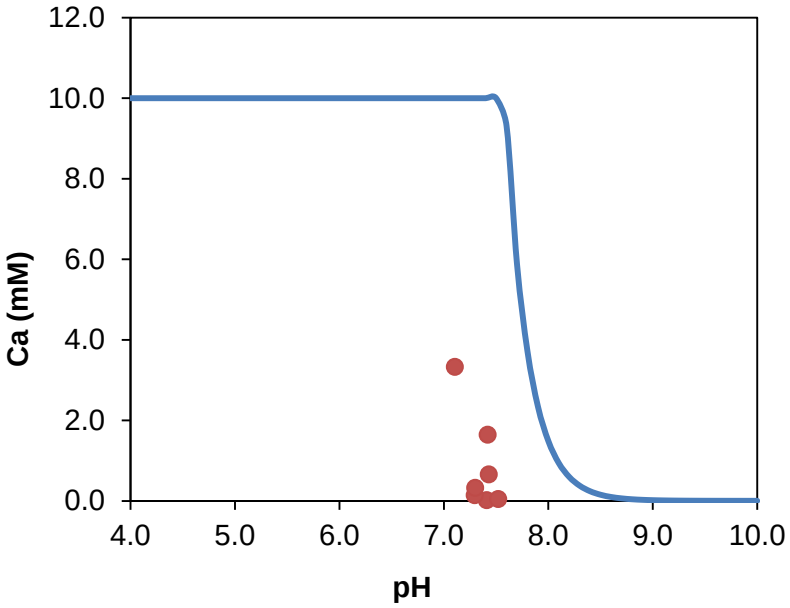

Figure S5.1. ─: Ca solubility in terms of $CaCO_3$ with the assumption that the system was open to the atmosphere. ○: Measured Ca concentrations after the adsorption experiments.

Chapter 6. Conclusions and Recommendations for Future Work

6.1 Conclusions

This doctoral thesis research explored metal behavior in both sediments and in aqueous suspensions of engineered nanoparticles. The work investigated the dominant mechanisms of uranium-phosphate and metal-nanoparticle interactions and examined their implications for field remediation and water treatment. Information about both systems was gained from using different experimental configurations, spectroscopy, microscopy, speciation calculations and modeling approaches. Specific conclusions from each task are described below.

Subtask 1A: Phosphate-induced immobilization of U(VI) in Hanford sediments

In the first task, batch and column studies demonstrated the influence of phosphate on U(VI) transport in environmentally relevant sediments. Batch experiments confirmed that both adsorption and precipitation could contribute to U(VI) retention, depending on the exact uranium and phosphate concentrations present. The specific concentrations in the column study as well as the high solid:water ratio in the column and occurrence of advective flow make the results of the column most directly relevant to subsurface environments. Once phosphate is introduced, sorbed U(VI)

would be harder to mobilize, which could largely limit the desorption of U(VI) during advective flow and hence decrease the downgradient U(VI) concentrations. Retention of U(VI) following phosphate addition to the Hanford sediments was shown to be due to enhanced adsorption of U(VI) species, including U(VI) adsorption to freshly formed calcium phosphate minerals, instead of formation of U(VI)-phosphate precipitates. After ceasing phosphate treatment, the effect on retention could last for a long duration without addition of phosphate, which can limit the costs and possible environmental impacts (e.g., eutrophication) that would be associated with larger and longer additions of phosphate. As slow U(VI) desorption from sediments may occur after ending phosphate addition, U(VI) release can be slowed and the released concentration may be controlled effectively by optimizing the timing and doses of phosphate addition, which can be beneficial for successful *in situ* uranium immobilization.

Subtask 1B: Modeling U(VI) sorption in Hanford sediments and the impact of phosphate addition

A multi-rate first order kinetic adsorption model was applied to fit U(VI) adsorption in batch system. The model descirbed the U(VI) adsorption with a rapid initial process followed by a slow adsorption, where the U(VI) transferred into the intraparticle pores. A one-dimensional non-equilibrium CDE model was used to fit uranium and bromide profiles, which yielded a retardation factor of 24.3 for U(VI), which showed higher adsorption to Hanford sediments than to previously studied Rifle sediments. As the CDE model only considered U(VI) transport in columns by

adsorption process with no consideration for the change of the water chemistry, an advanced reactive transport model was developed with the implementation of advective flow, surface complexation modeling, kinetically controlled mineral dissolution and full consideration of aqueous speciation. From simulating results in both batch and column systems, models revealed that with the addition of phosphate, U(VI) adsorption was enhanced by forming sediment-U(VI)-phophate ternary complexes that have higher adsorption affinity than U(VI)-carbonate complexes. In addition, the precipitation of Ca-P solids decreased Ca concentrations, yielding more U(VI) being adsorbed to the surface, instead of existing as poorly adsorbed Ca-U(VI)-carbonate complexes. Modeling approaches improved the understanding towards U(VI) behavior under complex geochemical conditions.

Task 2: Impact of water chemistry on U(VI) and Cr(VI) removal by various engineered magnetite nanoparticles and development of surface complexation modeling

Task 2 investigated the impact of water chemistry on U(VI) and Cr(VI) removal by engineered magnetite nanoparticles. Batch adsorption studies were performed to probe adsorption edges under various conditions (pH, DIC and initial loadings). The results provided information on U(VI) and Cr(VI) adsorption to nanoparticles coated with several types of organic acids that have different surface functions groups. Functional groups in stearic acid (SA), oleic acid (OA) and octadecylphosphonic acid (ODP) coatings led to different adsorption extents (SA$\approx$ OA > ODP) of U(VI) adsorption under the same conditions. The adsorption of U(VI) to OA-coated

nanoparticles decreased with initial U(VI) loadings due to the limited surface site. The largely inhibitory effect of dissolved inorganic carbon was caused by the formation of aqueous U(VI)-carbonate species that have lower adsorption affinity. While the highest U(VI) adsorption to SA, OA and ODP-coated nanoparticles happened at pH 6 to 7, Cr(VI) adsorption to CTAB-coated nanoparticles decreased when pH increased from 5 to 10, due to the change of electrostatic interactions between opposite charges. Surface complexation models were developed and predicted pH-dependent surface potential values that are consistent with measured zeta potentials. With a small set of adsorption reactions, the model can successfully simulate the entire adsorption dataset over all studied conditions. Predictable adsorption behavior benefits future application of nanoparticles in the water treatment system because adsorption performance can be assessed with the model over broader ranges than could be experimentally evaluated. The application of nanoparticles was observed to be affected with the presence of two drinking water supplies, and decreases in Cr(VI) adsorption were associated with the presence of Ca^{2+}. Because only slight aggregation was associated with Ca^{2+} and an observed increase in zeta potential with Ca^{2+} addition should actually enhance Cr(VI) adsorption, the causes of inhibition of Cr(VI) by Ca^{2+} are not associated with particle size or surface charge. Instead it is likely that Ca^{2+} influences the structure of the organic bilayer on the nanoparticle surfaces in a way that decreased the availability of surface sites. The application of the engineered adsorbents in treatment processes needs more consideration of their stability and treatment performance in real water resources.

6.2 Recommendations for Future Work

The information gained from this research project provided insights and advanced our understanding of metal behavior during interfacial interactions. Recommended future work includes but is not limited to (1) investigating the impact of changing water chemistry on U(VI) release from Hanford sediments; (2) investigating the impact of microbial activity on U(VI) retention; (3) testing the regeneration and reuse of nanoparticles and (4) performing column experiments with engineered nanoparticle-coated substrates deposited on substrate particles as the porous media to investigate metal removal under advective flow conditions.

The present results involved experiments with sediments from the vadose zone of Hanford site, Washington, where the water table is influenced by the water stage in the nearby Columbia River. The influent used in this study was synthesized according to the groundwater composition in Hanford site. However, interactions of groundwater and surface water may happen and change the water chemistry. It would be interesting to see uranium uptake behavior when groundwater and surface water interact with each other. In addition, this study has demonstrated a lasting benefit of phosphate addition on U(VI) immobilization. When phosphate was removed in the influent, small amount of U(VI) was released from sediments. It would be particularly interesting to see whether and how the change of water chemistry would affect the stability of immobilized U(VI) in the sediments. In addition to the impact of pH, dissolved inorganic carbon and other aqueous ions, the presence of organic matter might affect the U(VI) behavior in subsurface

environments, which would then affect the efficiency of phosphate-induced immobilization. As organic matter can also be strongly related to bioactivity, it would affect the immobilization pathway as a biotic reduction process to reduce U(VI) to less soluble U(IV) species. As a result, it would be interesting to study the effect of phosphate-induced immobilization with concurrent microbial activity in sediments.

The impact of Ca^{2+} on Cr(VI) adsorption to CTAB-coated magnetite nanoparticles remains unclear and it would be interesting to explore whether it was the Ca specifically or just the divalent positive charges of this type of cation. As a result, future Cr(VI) adsorption experiments with the addition of Mg could be a starting point to investigate this process. Metal adsorption by engineered magnetite nanoparticles were conducted in batch systems and investigated the impact of water chemistry on adsorption behavior. It would be interesting to study desorption of metals from nanoparticles that can benefit the reuse of the material. Studying the separation of nanoparticles by magnetic field and controlling the water chemistry to wash all the contaminants from nanoparticles would be important for the regeneration and reuse of the nanoparticles. In addition, to achieve high removal efficiency in real water treatment processes, nanoparticles need to be integrated into packed beds for long-term operation with continuous flow, which requires that the packed bed have high porosity and permeability. As a result, it would be essential to study the removal efficiency of metals by nanoparticles deposited on substrate, and quartz would be an easily accessible material. It would be interesting to study metal adsorption by nanoparticles deposited sand and how the availability of the surface

sites will change due to the deposition. By conducting adsorption in a continuous flow reactor, it would be interesting to test the overall performance, which might be affected by adsorption affinity of the sorbents, reaction kinetics, and advective and diffusive transport processes. Ideally the integration of these processes could be interpreted using a reactive transport modeling. After nanoparticles have been used for metal removal, it is necessary to test the possibility of regenerating used sorbent media for reuse or disposal in a column system.

Appendix A. Advanced Modeling of U(VI) Transport in Hanford Sediments and the Impact of Phosphate on the Transport Behavior

Appendix A is an expansion of my thesis research on U(VI) transport behavior in subsurface environment and the impact of phosphate, applying a more advanced modeling tool to predict U(VI) behavior in column studies under different flow rates with the introduction of phosphate. The modeling work was built upon the experimental data of Columns 5-8, which had their experimental data and a more rudimentary model presented in Chapters 2 and 3. I worked closely with Wen Hang, a Ph.D. student from Dr. Li Li's group at Pennsylvania State University in this modeling effort. I provided my conceptual model of the processes, detailed information on the column operation, and data from influent and effluent analyses, sequential extractions, and mass balance calculations. We worked together in the model development in order to understand U(VI) transport behavior and capture the impact of phosphate in the modeling approach. The actual modeling work was performed by Wen Hang, and the following simulation results were provided by him. We are preparing a co-authored a manuscript on this modeling work. Appendix A also includes all the aqueous reactions that were used in the surface complexation modeling that was used in Chapter 2 as well as in the modeling done in collaboration with the group at Pennsylvania State University..

Background

The previous modeling work simulated by CXTFIT (Chapter 3) was based on the assumptions that the aqueous phase can be partitioned into mobile and immobile regions, which is called a dual domain reactive transport model. Also in the CXTFIT modeling, only adsorption accounts for the retardation and the reaction rate is a constant, which would not be the real case. Adsorption is parameterized in CXTFIT just as a retardation factor that would only apply at one water chemistry conditions and without any consideration of the overall aqueous geochemistry. As a result, we collaborated with Dr. Li Li's group to develop a more advanced reactive model, which can consider all the aspects that could influence U(VI) transport through sediments-packed columns.

Modeling the adsorption in a batch system

Surface complexation modeling for batch systems without the presence of phosphate needed to be modeled in order to obtain equilibrium constants that can be used in in Phreeqc (software) to account for adsorption. As experimental conditions have been described in the main manuscript, here only the equation and the fitting result are presented. The logK_{eq} was adjusted but was still close to the value used in Stoliker's modeling, which was 21.66 ± 0.23. The model showed that the dominant U(VI) species in the solution were $Ca_2(UO_2)(CO_3)_{3(aq)}$ (60.5%), $Ca(UO_2)(CO_3)_3^{2-}$ (38.1%), $UO2(CO_3)_3^{4-}$ (0.7%), $UO2(CO_3)_2^{2-}$ (0.4%), $Mg(UO_2)(CO_3)_3^{2-}$ (0.1%) and others (< 0.1%).

$$\equiv SOH + UO_2^{2+} + 2CO_3^{2-} \rightleftharpoons SOUO_2\left(CO_3HCO_3\right)^{2-} \qquad \log K_{eq} = 20.6$$

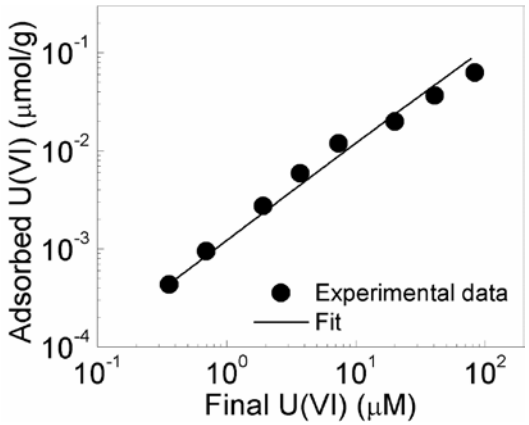

Figure A1. Modeling result for U(VI) adsorption to Hanford sediments with no phosphate addition. Batch adsorption experiment was conducted for 48 h to reach equilibrium with initial U(VI) loadings from 0 ~ 100 μM at a solid:water ratio of 250 g/L.

The modeling work was developed in order to investigate the impact of phosphate on U(VI) transport behavior during the desorption phase. In addition to the previously developed surface complexation reactions, additional reactions related to phosphate were introduced into the model. The surface adsorption of U(VI) with the presence of phosphate was described by the following reaction with the equilibrium constant obtained from the fitting results.

$$\equiv SOH + {UO_2}^{2+} + {PO_4}^{3-} \rightleftharpoons SOUO_2{PO_4}^{2-} + H^+ \quad log\, K_{eq} = 10.1$$

A.

$$Ca(UO_2)_2(PO_4)_2(s) \rightleftharpoons 2{UO_2}^{2+} + Ca^{2+} + 2{PO_4}^{3-} \qquad log\, K = -48.36$$

$$\mathrm{Na_2(UO_2)_2(PO_4)_2(s) \rightleftharpoons 2UO_2^{2+} + 2Na^+ + 2PO_4^{3-}} \quad \log \mathrm{K} = -47.41$$

B.

$$Ca(PO_4)_{0.74}H_{0.22}(s) \rightleftharpoons Ca^{2+} + 0.22H^+ + 0.74{PO_4}^{3-} \quad \log K = -13.10$$

$$Ca_5(PO_4)_3OH(s) + H^+ \rightleftharpoons 5Ca^{2+} + 3{PO_4}^{3-} + H_2O \quad \log K = -44.33$$

Two sets of solid dissolution-precipitation reactions were considered and are listed above as A and B. These dissolution-precipitation reactions affected the aqueous speciation of U(VI), Ca/Na and phosphate. While these logK values represent the thermodynami equilibrium conditions (Mehta et al, 2013), the process can be controlled kinetically and the precipitation reactions may not actually occur during the experiment operation period. For reaction set A, lower the *Keq* values led to better fitting results. Otherwise, uranium-phosphate precipitation occurs in the conditions with low initial U (< 25 μM when P = 1000 μM), which is not constant with experimental observations (Pan et al, 2017). Reaction set B was not useded because the final PO_4 concentration would be much lower than the experimental measurements. It further confirms that U-Ca/Na precipitation is kinetically controlled. Based on the selection of Reaction Set A, the reaction framework was simplified by not considering negligible reactions and the modeling results were shown in Figure A2.

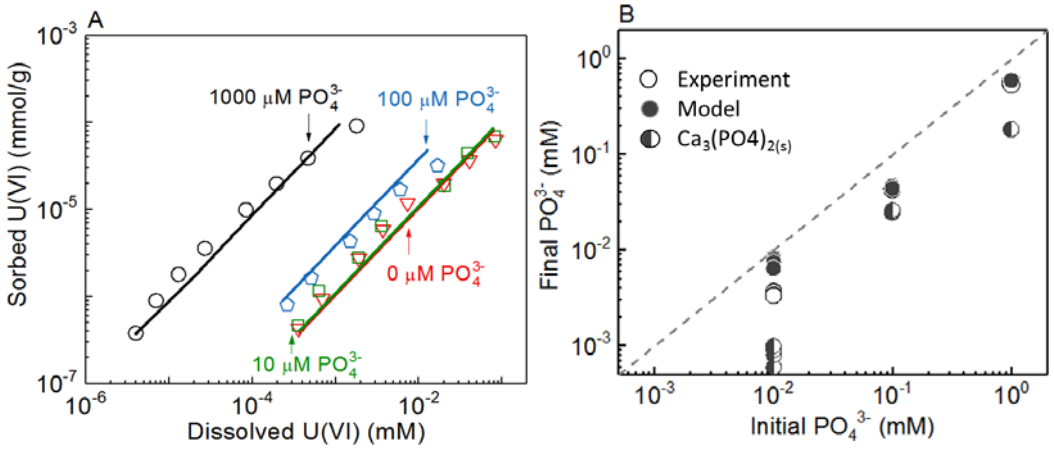

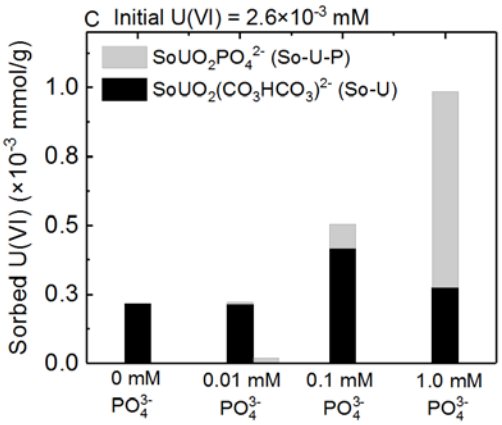

Figure A2. A. Modeling results of U(VI) adsorption to Hanford sediments with phosphate addition at 10, 100 and 1000 μM. The comparison of modeling results to the experiment data; B. Comparison of the PO_4^{3-} concentrations to the experiment measurement and the predicted Ca-P precipitates; C. Predicted amount of adsorbed U(VI) as So-U and So-U-P forms.

Different levels of precipitation of solid $Ca_3(PO_4)_2(s)$ were predicted to occur under conditions with initial PO_4 concentrations of 10 μM to 1000 μM (Figure A2). However, other forms of calcium phosphate solids were observed to be formed that might be the precursor of $Ca_3(PO4)_2(s)$ (Mehta et al. 2014). As a result, this reaction was considered in the model to phenomenologically account for the importance of the Ca-P precipitation. The $Ca_3(PO4)_2(s)$ precipitation lowers the Ca^{2+} concentration in the solution and therefore reduces the concentrations of aqueous complexes $Ca_2(UO_2)(CO_3)_3(aq)$ and $Ca(UO_2)(CO_3)_3^{2-}$. More UO_2^{2+} is adsorbed onto the solids. Under conditions with low initial PO_4^{3-} concentration (10 μM and 100 μM), over 90% of adsorbed UO_2 is in the form of the surface complex $\equiv SOUO_2(CO_3HCO_3)^{2-}$, being the dominant species (Figure A2). Under conditions with high initial PO_4^{3-} concentration (1000 μM), the surface complex $\equiv SOUO_2PO_4^{2-}$ dominates, with over

60% of adsorbed UO_2 being in the form of $\equiv SOUO_2PO_4^{2-}$. The finding was consistent with previous interpretations that with no uranium-phosphate precipitation, U(VI) adsorption can be promoted by phosphate, forming the ternary surface complex $\equiv SOUO_2PO_4^{2-}$. The modeling results also indicate that the effect of phosphate on U(VI) sorption highly depends on the geochemical aqueous conditions, including phosphate and calcium concentration.

For column experiments, two flow rates were applied with one for Columns 5 and 6 and a value twice as high for Columns 7 and 8. A homogeneous domain was first applied to try to fit all four experiments, but it could not describe the adsorption behavior. As a result, a heterogeneous domain with mobile and immobile zones was applied, and there was a first-order rate expression for diffusive exchange between mobile and immobile zones. The sphere radius of immobile zones and the corresponding shape factor were taken from Van Genuchten, 1985.

$$\frac{dM_{im}}{dt} = \alpha\left(C_m - C_{im}\right)$$

$$\alpha = \frac{D\theta_{im}}{\left(rf_{s\to 1}\right)^2}$$

M_{im} : moles of chemical in the immobile zone,

θ_{im}: immobile zone porosity,

C_m *and* C_{im}: concentrations in mobile and immobile zone (mol/kgw),

t : time (s),

α : the exchange factor (s^{-1}).

D : the diffusion coefficient (m^2/s),

R : the sphere radius of immobile zones,

$f_{s\to 1}$: shape factor for sphere-to-first-order-model conversion.

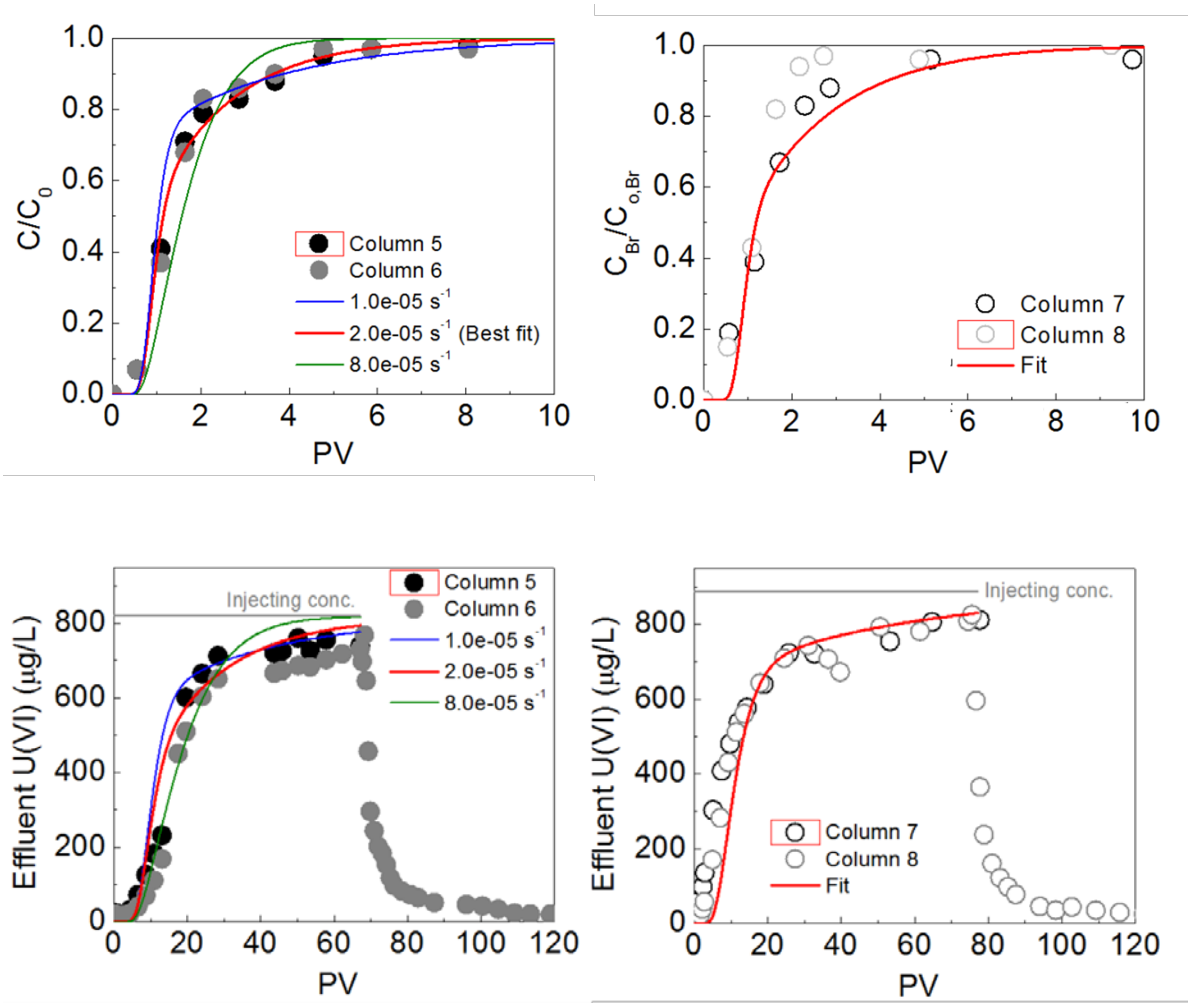

Figure A3. Simulation results by a two-domain model for breakthrough profiles of trace metal (upper two) and U(VI) (lower two). For Column 5 and 6, the flow rate was and 1 PV equaled to 2.75 hours. For Column 7 and 8, the flow rate was and 1 PV equaled to 1.38 hours. Green, red and blue lines were simulations obtained with three diffusive exchange factors as indicated in the figure, among which the red lines in both U(VI) and Br figures had the best fitting results.

The residence times for Columns 5 and 6 and 7 and 8 were 2.75 hours and 1.31 hours, respectively, and the breakthrough curves were plotted as a function of pore volume (PV). The model was developed from simulating column physical

properties, according to the breakthrough profile of trace metal Br (Figure A3). Modeling was performed with numerous tests with changing the diffusive exchange factors, which led to changes of the output profiles. The best fitting results with diffusive exchange factors of 2.0e-05 s^{-1} and 1.5e-05 s^{-1} for each set of columns are reasonable according to a Phreeqc example that has a diffusive exchange factor of 6.8e-06 s^{-1} under similar physical conditions. Immobile zones in Columns 5 and 6 and Columns 7 and 8 may have different shapes. Small diffusive exchange factors leads to early starts and long tails in breakthrough curves.

During the simulation for U(VI) adsorption in columns, all parameters of equilibrium adsorption constants and other physical properties are directly from the batch reactor and breakthrough curves. The same value of diffusive exchange factor that achieved the best fit for Br also led to a good fit for U(VI) breakthrough curves. The effect of diffusive exchange factor on U(VI) adsorption follows the same trends with nonreactive Br. In the case with high diffusive exchange factor, U(VI) can be transported into the immobile zones more easily, resulting in more U(VI) on solids and less U(VI) in the effluent solution. With time, more sorption sites are occupied and less U(VI) can be adsorbed onto solids.

U(VI) concentrations of Columns 5 and 6 in aqueous and solid phases were plotted as a function of length, which both showed decreasing trend along the column length (Figure A4). For both phases, differences between mobile and immobile zones are significant at the early period (10 PV > 20 PV > 67 PV) and became more identical after later period. The significant differences at the early period were due to the limitation of diffusion exchange.

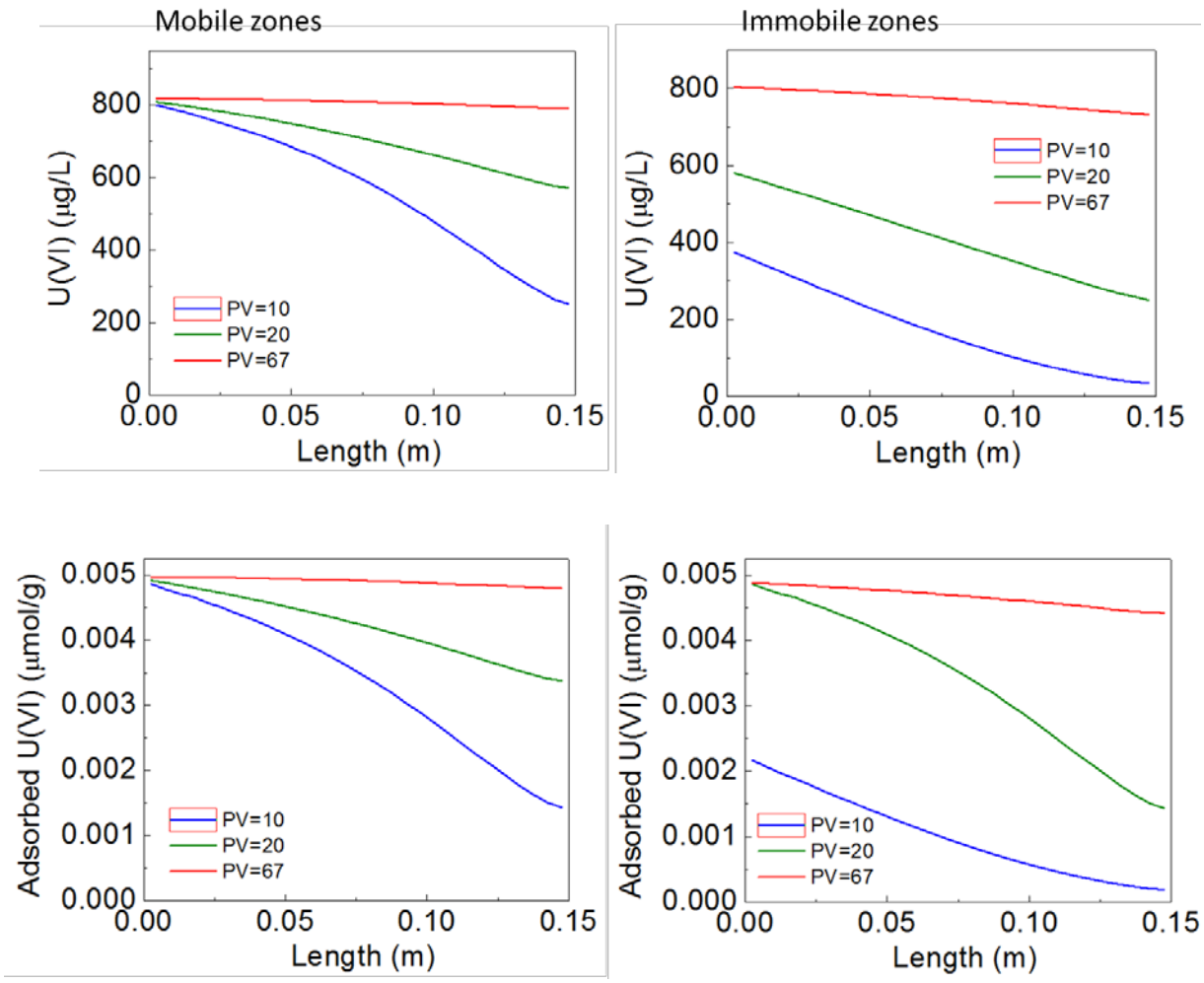

Figure A4. U(VI) in mobile zone and immobile zone as a function of length in Column 5&6. Upper two: U(VI) concentration in aqueous phase; Lower two: U(VI) concentration in solid phase.

Sensitivity analysis tested the effects of porosity, dispersivity, influent velocity and the influent concentration on simulated effluent profiles (Figure A5). Porosity and dispersivity did not affect the shape of the breakthrough curves and there was only a slight change after 20 PV (porosity) and the beginning stages (dispersivity). However, the change of the flow rate caused significant differences,

confirming the hypothesis that U(VI) adsorption process was a non-equilibrium process and was controlled by its intraparticle diffusive process.

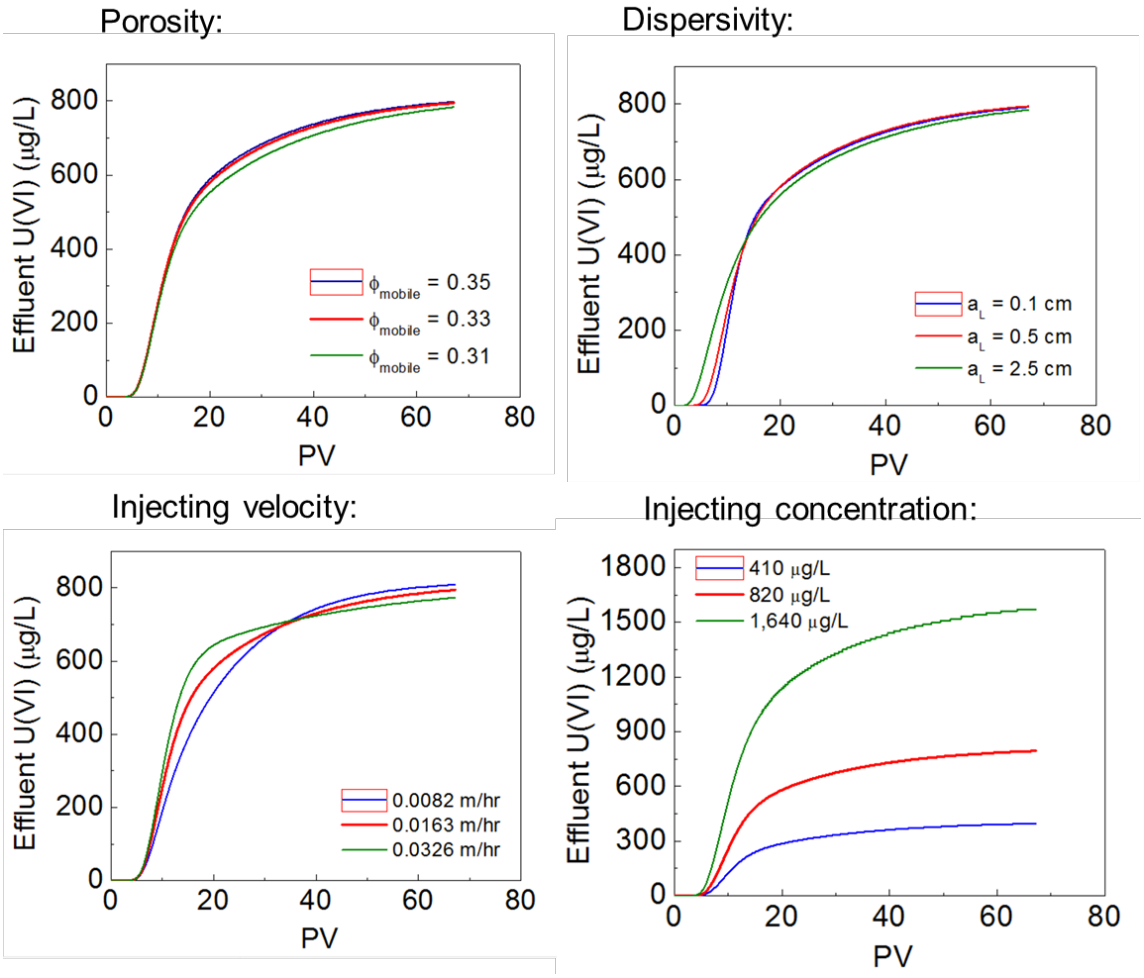

Figure A5. Sensitivity analysis of porosity, despersivity, injecting velocity and injecting concentration on U(VI) breakthrough curves.

Modeling the Batch and Columns with Phosphate

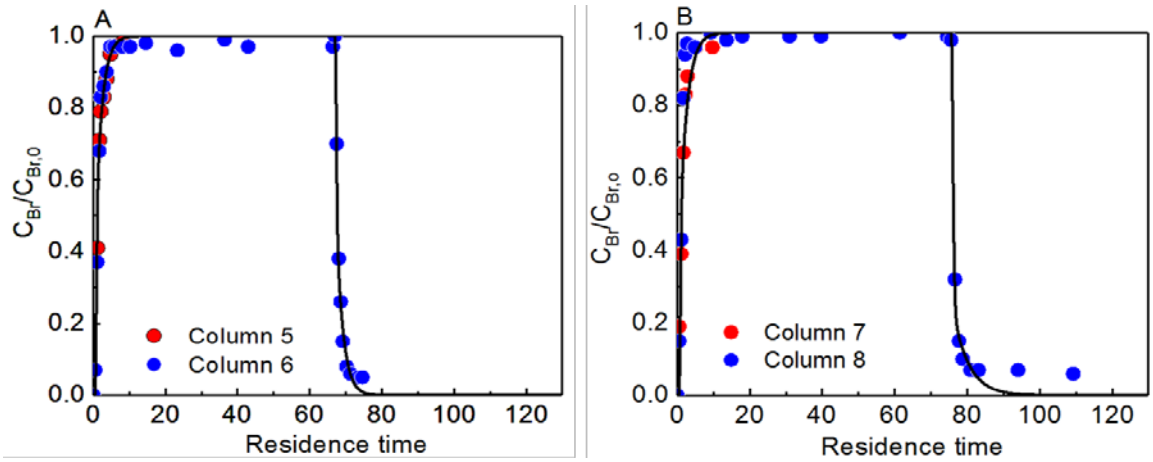

Figure A6. Breakthrough curves of nonreactive tracer Br in the whole process and the modeling results.

The surface complexation reactions were again included in the reactive transport model for column study. The behavior of the Br tracer in Columns 5-6 and Columns 7-8 could be successfully predicted with the same parameters used for modeling the adsorption phase (Figure A6). The model could predict the fast decrease of effluent U(VI) concentrations (Figure A7). Different scenarios have been tested: (1) no phosphate added into the injecting fluid; (2) phosphate added but no $Ca_3(PO_4)_{2(S)}$ precipitation; (3) phosphate added and the thermodynamic precipitation of $Ca_3(PO_4)_{2(S)}$ and (4) phosphate added and the kinetic-controlled precipitation of $Ca_3(PO_4)_{2(S)}$. Among four scenarios, the last one led to the best fit to the U(VI), PO_4^{3-} and Ca effluent profiles during the desorption phase at the same time. It was observed that Ca concentration played a significant role in controlling the U(VI) retention (Figure A8).

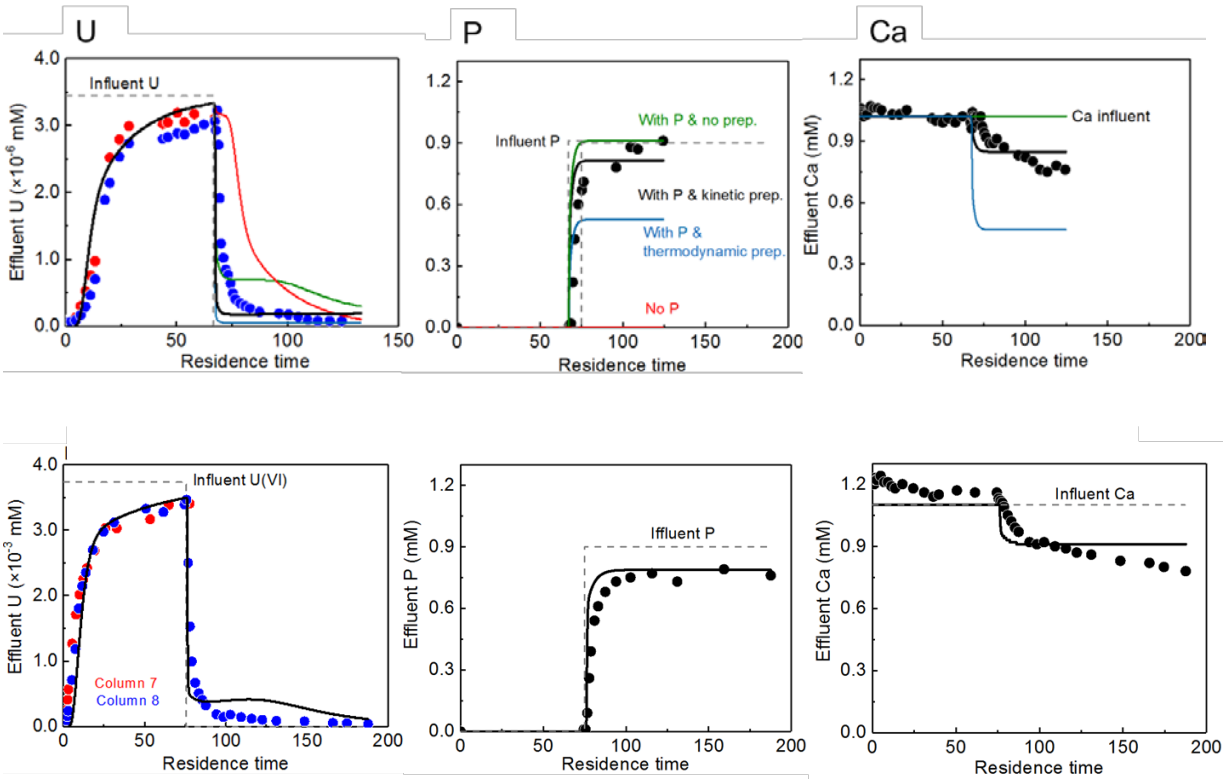

Figure A7. Modeling the breakthrough curves of U(VI), P and Ca effluents under four scenarios for Column 5 and 6 (upper three), Column 7 and 8 (lower three).

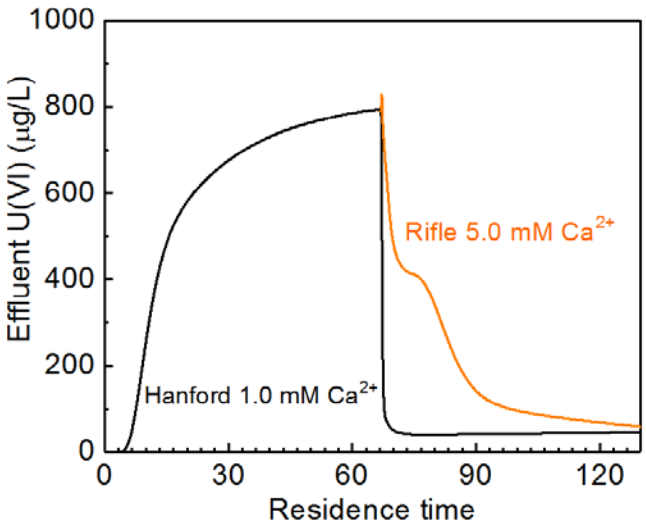

Figure A8. Modeling results for U(VI) profiles with two Ca^{2+} concentrations in the influent for the release phase with 1 mM PO_4^{3-}.

According to the modeling result, with higher Ca^{2+} loading, less U(VI) can be retained in the column. The formation of more stable Ca-U-P ternary complexes would inhibit the adsorption of U(VI) onto sediments. This is also consistent with the previous findings that phosphate addition is less effective for U(VI) immobilization in Rifle site, where the groundwater has much higher Ca^{2+} concentration (~5.0 mM).

U(VI) distribution along the column has been presented in both aqueous and solid phases, under different scenarios. If no phosphate was in the influent, then the U(VI) desorbs from solids gradually. For Scenario Four, the Ca-P precipitation reduces the Ca^{2+} concentration in the aqueous phase, leading to more desorbed U(VI) in the form of UO_2^{2+} that could be able to form uranly carbonate and uranyl hydroxide complexes, rather than Ca-U aqueous complexes. Therefore more U(VI) can be re-absorbed onto the solids. It results in differences of findings from the literature regarding to the impact of Ca. Comarmond16 found that due to no Ca^{2+} in the solution, no significant increase in U(VI) uptake in presence of phosphate (< 100 μm).

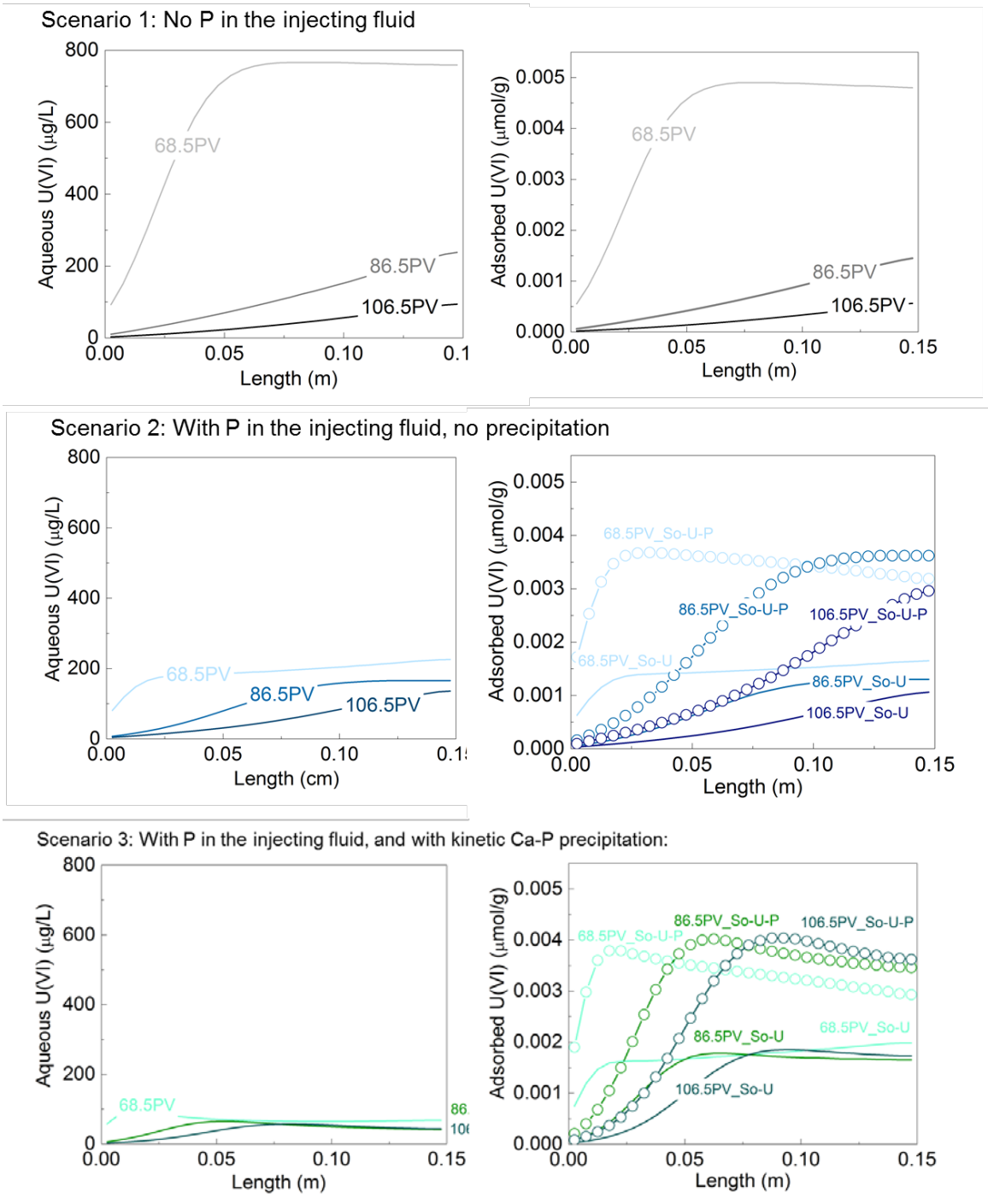

Figure A9. Modeling of U(VI) concentrations (left: aqueous concentrations in µg/L; right: solid concentrations in µmol/L) at three times during the release phase (68.5, 86.5 and 106.5 PV) along the column length for Column 5 and Column 6 under three scenarios. With the presence of phosphate and for U(VI) concentrations in solid phases, the concentrations of U(VI) in the form of So-U and So-U-P was plotted.

Several major findings can be drawn from the modeling work. Phosphate addition enhances U(VI) sorption through two mechanisms in both batch reactors and columns: (1) Ca-P precipitation, lowering the formation of poorly adsorbed Ca-U(VI)-carbonate species due to decreased Ca concentration and (2) the formation of ternary surface complex So-U-P. Therefore phosphate addition helps retain more U(VI) in the sediments. Under low initial phosphate condition, mechanism (1) is more dominant. With phosphate addition, the Ca^{2+} concentration plays a critical role in U(VI) sorption. Low Ca^{2+} helps retain more uranium in the system.

Advective flow and intraparticle diffusive transport affect the U(VI) sorption in heterogeneous media. The immobile zones inhibit the U(VI) sorption due to the slow transport rates. And the fast overall flow velocity lowers the mass of adsorbed uranium on solids. The reactive transport model in this work helps better understand the impact of phosphate addition on uranium sorption in natural systems.

Appendix B. Heavy Metal Concentrations, Bioaccessibility and the Potential for Human Exposure in Urban Community Gardens: A Study in St. Louis, Missouri

Appendix B is about the measurement of metal levels and Pb bioaccessibility in soils from urban community gardens in St. Louis City and neighboring St. Louis County. I participated in processing both soil and tomato leaf samples and acid digestions. I was in charge of the sample analysis to obtain elemental compositions for all soil samples. I participated in the data analysis process and project discussions for the interpretations of the results. The text below is an excerpt from a manuscript that has been submitted to Journal of Environmental Quality, 'Heavy metal concentrations, bioaccessibility and the potential for human exposure in urban community gardens: A study in St. Louis, Missouri', the authors are Manvitha Marni, Roger Wong, Leah Gable, Zezhen Pan, Zorimar Rivera-Núñez, Daniel E. Giammar.

Introduction

Community gardening is a popular activity throughout the United States, with the American Community Gardening Association estimating that there are approximately 18,000 community gardens throughout the U.S. and Canada (American Community Gardening Association, 2017). Common reasons for participating in community gardening include "to consume fresh foods" and "to improve health among members," indicating that gardeners perceive that community gardening offers health benefits (Guitart et al., 2012). Gardeners, however, are also aware of potential environmental health concerns associated with community

gardens. Community garden soils are subject to federal standards that specify the permissible amounts of Pb, As, and other toxic elements in soils used for specific purposes. These elements can be absorbed by humans through ingestion of soil and produce grown in the soil. Furthermore, in humans, metal internal dose has been shown to be associated to soil metal levels (Yankel et al., 1977).

Lead is a contaminant of particular concern in urban soils. A survey of Baltimore gardeners showed that 11 percent of respondents were concerned about toxic metals and other trace elements as soil contaminants, with Pb the foremost of those concerns (Kim et al., 2014). Particularly in urban areas, historical industrial activities have often resulted in metal contamination of the surrounding soils. In Oakland, California soil lead concentrations at potential urban agriculture sites had spatial variations associated with past land use (McClintock, 2012). A study of gardens south of Boston identified the two primary sources of Pb in the gardens as leaded gasoline and paint containing Pb (Clark et al., 2006). For this study some gardens had clean fill soil from outside sources that would ideally be less contaminated than in-ground soil. However, a later study by Clark et al. (2008) showed that raised beds containing clean fill soil showed an increase in average Pb over four years, indicating the potential for accumulation of contaminants in soils under modern and not legacy industrial conditions.

Lead contamination of soils is an important environmental issue in Missouri, which is the context in which the present study was performed. The current federal standard limits Pb to 1200 µg/g in residential areas not frequented by children (US EPA, 2001). Soil located near a former lead smelter in southwest Missouri far

exceeded this concentration, containing 4361 µg/g of Pb. Those living near the smelter had elevated blood lead levels (Yang et al., 2001), which is the standard biomarker to assess Pb exposure. In Herculaneum, which was home to an active lead smelter through 2013 and is less than 50 miles south of St. Louis, residential soil was found to contain Pb levels as high as 33,100 µg/g (Kuster et al., 2004). Some residents' blood also contained elevated Pb levels, with 28 percent of children under 3 years old having levels higher than 10 µg/dL (Minor et al., 2002). Herculaneum's soil also contained up to 82 µg/g As and 240 µg/g Cd (Missouri DNR, 2002). A study in East St. Louis, Illinois, located across the Mississippi River from St. Louis, found that the western half of the city had an average Pb concentration of 427 µg/g; this study specifically indicated gardening in the studied soils as a potential health concern (Kaminski and Landsberger, 2000).

Objectives

The objectives of the current study were to examine the potential risk for toxic metals in urban soils to affect human health from community gardening. To that end, samples of soil and tomato leaves were collected from St. Louis community gardens and the levels of major and trace elements in those samples were measured. These concentrations were analyzed to determine potential sources of contamination and routes of exposure. In addition, surveys were administered to gardeners to assess typical gardening practices.

Materials and Methods

Gardens Studied.

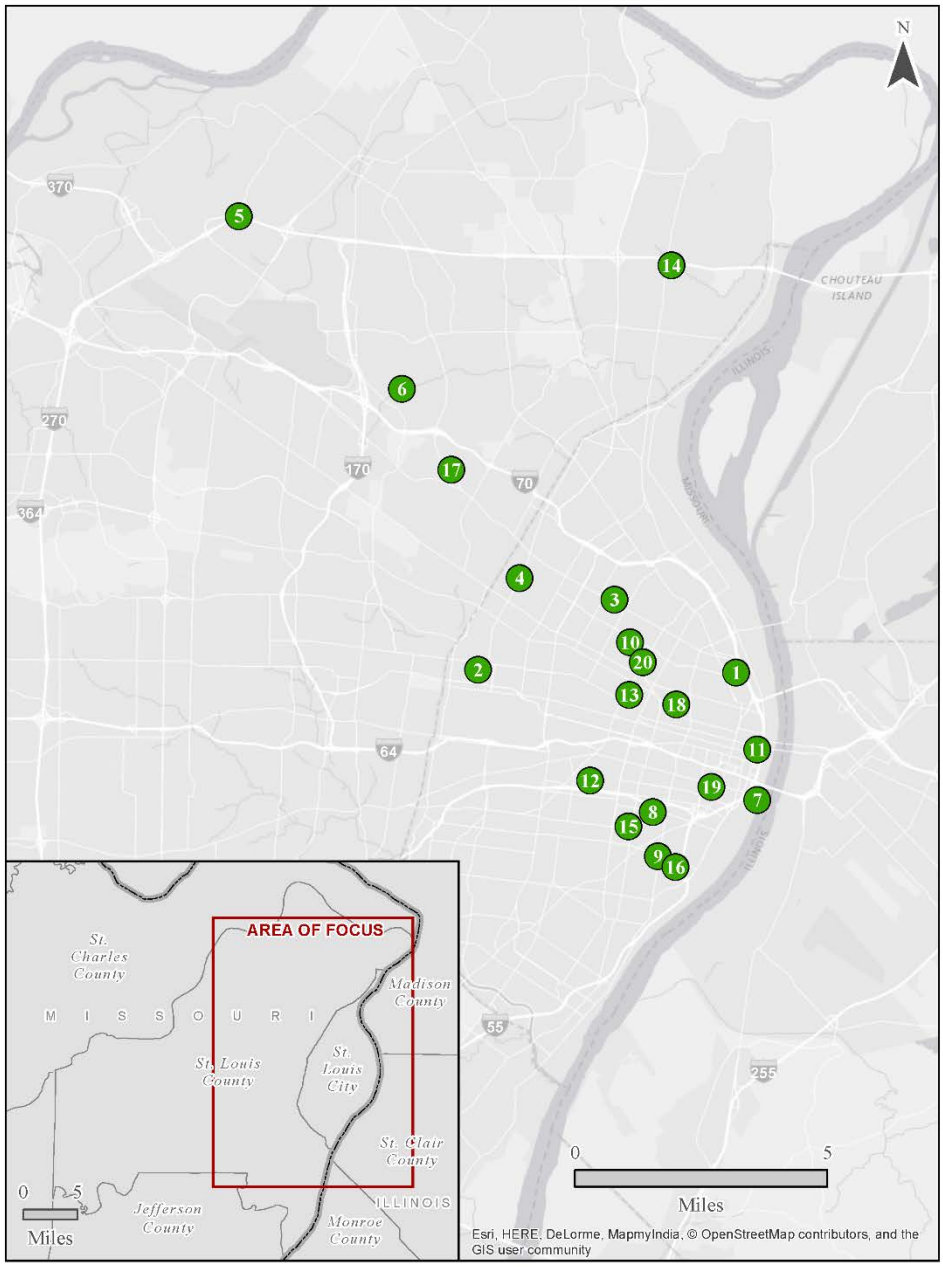

Figure B1. Map of gardens chosen for sampling. Inset displays area of focus of study

Twenty community gardens (Figure B1) were chosen from throughout St. Louis City and the northern part of neighboring St. Louis County. Gateway Greening, a local community gardening network, helped identify community gardens to represent four geographical areas within St. Louis City and County. Our final sample consisted of five community gardens within each of the four geographic regions of St. Louis: South, Central, North St. Louis County, and North St. Louis City. Soil samples were collected and a total of 93 gardeners were interviewed from all 20 gardens between June and August 2015. Tomato leaf samples from 10 of the gardens were also collected in July 2015. Gardens ranged in age from newly founded to nearly thirty years old. Six gardens were re-visited in November 2015, after produce had been harvested. Soil was re-sampled to determine if sampling location, season, or other factors such as turning the soil affected metal concentration. Soil samples were collected and analyzed for total metals content as during the initial sampling.

Soil Sampling and Analysis.

Gardens ranged in size from eight plots to over 30, with plots typically measuring 10 feet by 3 feet. In each garden, four plots were sampled to provide a snapshot of plot-to-plot variability. All but two plots sampled were raised beds filled with soil brought in from another source; the remaining two plots were in-ground beds. Non-adjacent plots in each garden were sampled to provide a representation of all parts of the garden. Three surface soil samples were taken from each plot by inserting a hollow plastic barrel (inner diameter 2.6 cm) to a depth of 9.8 cm into the

soil. Soils were stored in resealable plastic bags and kept in a refrigerator after sampling.

After sampling, the three samples from each plot were combined and hand-mixed thoroughly to create a representative composite sample. These samples were then oven-dried at 110^{o}C for 24 hours. Dried soils were used in all analysis procedures. Soil pH was measured with a pH probe in the solution generated from a 5:1 by mass water:soil mixture. To digest the samples in preparation for measurement of total metal concentrations, 0.25 g of soil were combined with 8 mL concentrated HNO_3 and 2 mL concentrated HCl. The mixture was heated at 100 ^{o}C for 4 hours before being diluted with 40 mL ultrapure water and filtered with a 0.2 □m PES filter. Duplicate samples for each plot were extracted. In order to test whether the soil digestion was effective in measuring total metals content, duplicate samples (2 g each) of a reference soil (Montana II Soil / Standard Reference Material 2711a) with a known composition were digested and analyzed by the same processes used for the garden soils. The results were in the range of the concentrations as reported by using EPA Method 3050B (USEPA, 2015).

The urban soils bioaccessible lead test (USBLT) was used to assess the amounts of Pb that could become accessible for human uptake if the soils were ingested (Beyer et al., 2016). Soils were passed through a 1.4 mm sieve and 2.5 g of sieved soil were combined with 25 mL of 0.4 M glycine that had been adjusted to pH 2.5. The samples were then agitated in a platform shaker at 100 RPM for two hours. The extraction was run at the ambient laboratory temperature (22±2 °C). Extracts were filtered through medium porosity filter paper (Whatman) followed by a 0.2 □m

polyethersulfone filter (Tisch Scientific). The extraction was run in duplicate for each plot.

The filtered samples from the total digestions and bioaccessibility tests were analyzed with inductively coupled plasma mass spectroscopy (ICP-MS) (Agilent 7500ce or Perkin-Elmer ELAN DRC II). A multi-element analytical method was used to quantify concentrations of Pb, As, Cd, Cu, Co, Ni, Mo, Ca, Mg, Fe, Zn, and Cr.

After the initial soil samples had been taken, leaves from tomato plants in ten of the gardens were collected. Eight leaves were collected from tomato plants in each of four plots in ten of the gardens; this usually involved collecting leaves from four plants in each plot, but fewer plants were used if a plot did not have four plants. When possible, leaves were collected from the same plots where soils had been sampled, but other plots were used when the original plots contained no tomato plants. For each plant, pairs of leaves were collected with one closer to the roots and the other higher up on the plant. Leaves were collected by cutting them off the plant. After sampling, leaves were oven-dried at 105 ^{o}C for 12 hours. Dried leaves were digested in nitric acid and analyzed by ICP-MS (PerkinElmer NexION) in a laboratory specializing in high-throughput plant tissue analysis. Leaves were analyzed for As, Cd, Na, Mg, Al, Ca, Fe, Mn, Co, Ni, Cu, Zn, Se, and Mo. The leaves were not analyzed for Pb because it was not an element run in the standard protocol of the plant tissue analysis laboratory.

Gardener Surveys.

Structured gardener surveys including questions on demographics, gardening practices and activities, and exposure were developed following a previous study conducted on urban community gardeners (Kim et al., 2014). Gardening practices and activities included items such as fertilizer, pesticide, and compost use. Questions on exposure examined items such as types of protective gear used, time spent at the garden, and type of produce grown. Garden leaders were also interviewed to obtain additional information including gardens' age and previous use of the land on which the garden was currently set. Interviews were conducted alongside soil sampling. Gardens were visited on days when the highest proportion of gardeners was present based on garden leaders recommendation. Results for the gardener surveys were analyzed using SPSS version 22. The Human Research Protection Office at Washington University in St. Louis approved the gardener surveys (#201506004).

Results and Discussion

Soils

Soil pH values ranged from 6.39 to 7.87, with a mean of 7.34. Gardens tended to have consistent pH across plots, with the exception of Garden 2. This matches the expected pH of St. Louis area soils, which typically have pH values above 6.0 (Nathan et al., 2007).

Although soil Pb concentrations varied from plot to plot, overall Pb concentrations did not exceed EPA standards (400 µg/g for "bare [residential] soil in children's play areas") (Figure B2a). One plot in Garden 13 had a value above 500

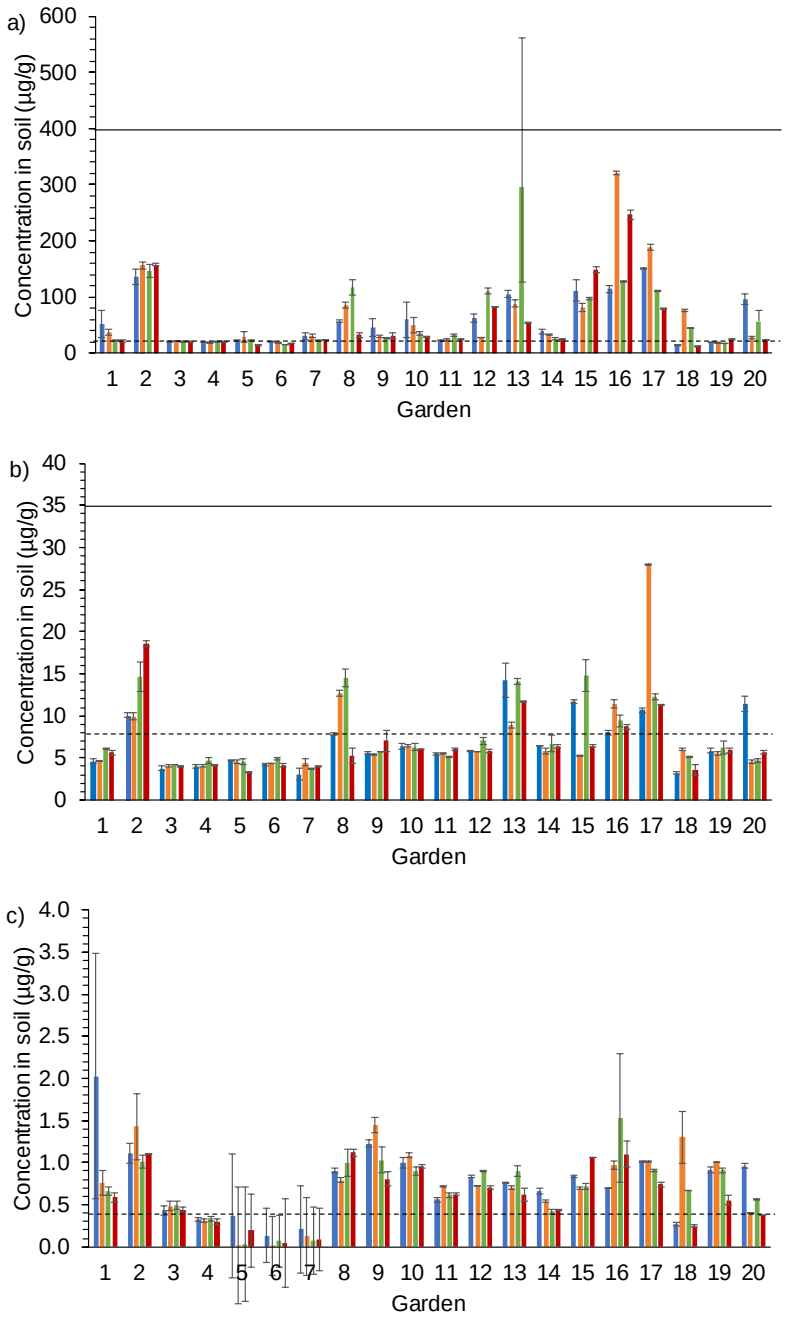

Figure B2. Total concentrations of (a) lead, (b) arsenic, and (c) cadmium for original soil samples. Individual bars indicate average concentrations by plot in each of the 20 gardens, with error bars showing minimum and maximum concentrations. Solid lines indicate EPA non-carcinogenic screening levels; dashed lines indicate average Missouri surface soil concentrations from USGS data. The screening level for cadmium is 71 µg/g, so it would be out of range for panel c.

µg/g for one of the duplicate extractions of soil from that plot, but the average for the plot was 296 µg/g. Based on U.S. Geological Survey (USGS) samples, the average surface soil Pb concentration in Missouri is 29.2 µg/g (Smith et al., 2014). Of the 80 plots sampled, 34 had an average Pb concentration below the 29.2 µg/g state average. Despite the high levels of Pb in many southeastern Missouri soils impacted by smelting and other industrial activities, the generally low levels of Pb in the raised beds sampled suggest that Pb is not a major environmental health threat in the gardens sampled. This could be due to the use of clean fill soil and raised beds, which reduce contact with the local soil that would be impacted by a longer legacy of urban industrial activity. Clean fill was also associated with lower Pb concentrations in a large community garden in Terre Haute, Indiana for which spatial variation was assessed (Latimer et al., 2016). However, regional sources of lead-containing windblown particles do have the potential to recontaminate gardens treated with clean fill as was observed in urban neighborhoods in Boston (Clark et al., 2008).

The Missouri average As soil concentration based on USGS samples is 7.63 µg/g (Smith et al., 2014). Of the 80 plots sampled, 22 exceeded this concentration (Figure B2b). These plots tended to be clustered in the same garden, with four gardens having all plots in excess of the state average. All plots had As levels above the EPA screening level of 0.68 µg/g for carcinogenic risk, but well below the screening level of 35 µg/g for noncarcinogenic risk to children (US EPA, 2016). Although As levels, even in clean fill soil, do exceed EPA carcinogenic screening standards, the majority of gardens are generally in line with statewide average As

concentrations. Therefore, urban gardens in St. Louis do not appear to pose a higher risk with respect to As than gardens elsewhere in Missouri.

The Missouri average Cd concentration based on USGS samples is 0.268 µg/g (Smith et al., 2014). Nearly all plots exceeded this concentration, but all fall well below the noncarcinogenic screening level of 71 µg/g (Figure B2c). Although St. Louis community gardens do appear to have higher concentrations of Cd than in the rest of the state, Cd likely does not pose an environmental health threat.

Lead and As concentrations were positively correlated with garden age (Figure B3), with Pearson correlation coefficients of values of 0.58 and 0.64, respectively. These correlations could indicate that clean fill soil is being contaminated over time because new inputs of Pb and As could accumulate over time to result in higher concentrations in older gardens. Such accumulation of contaminants over time in urban gardens was shown by Clark et al. (2008), and they determined that the contamination appeared to be a consequence of transport of wind-blown particles. However, the increases in lead over a four-year period in that study (from an average of 150 µg/g to an average of 336 µg/g) are much larger than the differences in lead concentrations between newer and older gardens in our St. Louis study. Consequently, any recontamination is less severe in the gardens studied here or the trend in Pb and AS concentrations with garden age could be the result of the source of the clean fill soil having changed over time, with newer sources containing less Pb and As.

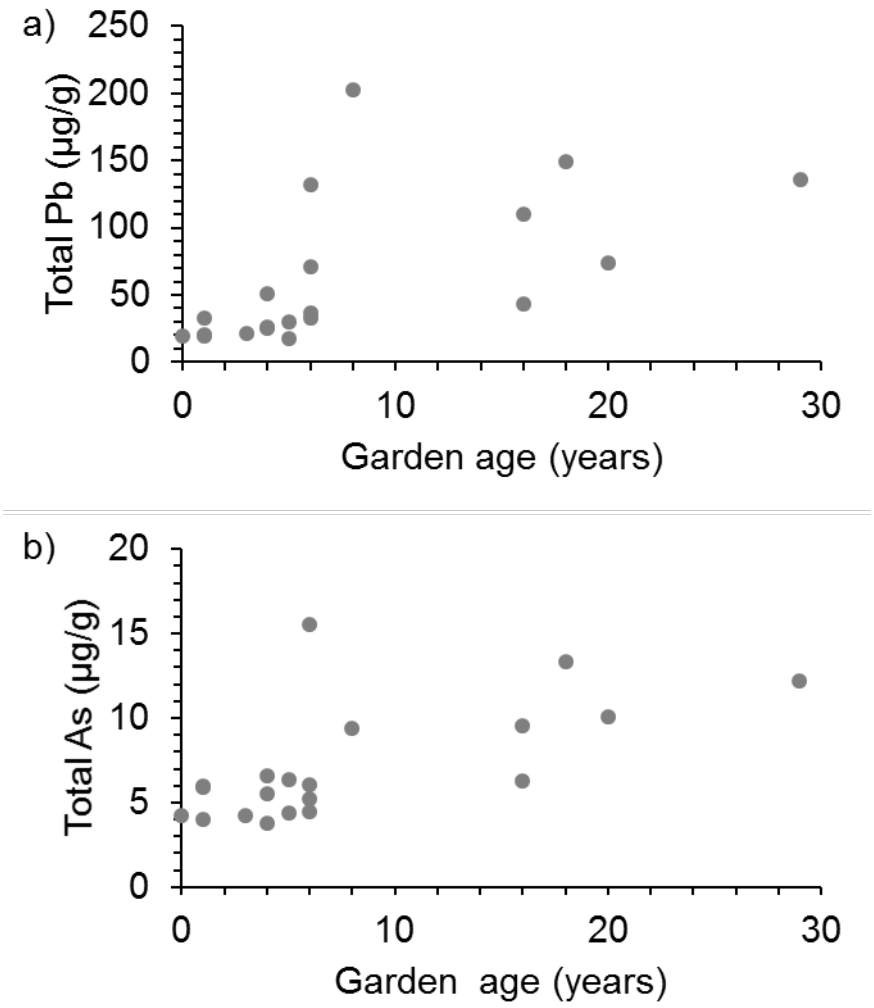

Figure B3. Average total (a) lead and (b) arsenic concentrations in soils

Most gardens showed little variation in Pb, As, or Cd from plot to plot. Several gardens, such as Gardens 3, 4, 5, 6, and 19, had consistent, low levels of all three elements. All of those gardens were established five years or fewer before sampling, which could account for this trend. Because newer gardens had all added clean fill soil to the beds recently, their metal concentrations are unlikely to have

been significantly affected by the use of fill with higher metal concentrations or the recontamination of the soil over time that had affected older gardens.

Total Pb and Zn concentrations had an appreciable correlation, with a Pearson correlation coefficient of 0.69. The correlation between Pb and Zn in soil may offer insight into the original source of possible contamination. Lead contamination from leaded gasoline, lead paint, or other lead-containing products would not be correlated with Zn. Hence Pb in the soils probably comes from natural sources or from the deposition of particles from ore-processing facilities and not from lead-containing products. Particles from smelters have Pb and Zn proportions that are similar to those in the raw ore (Batonneau et al. 2004), and Pb and Zn are both rich in these ores. Studies of soils impacted by smelter emissions have found elevated concentrations for both Pb and Zn (Deng et al., 2016; Douay et al., 2008).

Concentrations of Pb in the six gardens that were resampled 4-5 months after original samples were collected were generally consistent with the original values (Figure S1 of supplemental material). The average absolute percent difference in Pb was 21 percent in Pb for the plots sampled in different seasons. Of the 23 samples, 10 had Pb concentrations within 10 percent of the original sample concentrations. Because the November samples were collected from the same plots but not the exact same locations as the June-August samples, the values being comparable for both sampling periods suggests that plots tend to have consistent concentrations across time and space. Some beds had been turned between the original sampling and re-sampling, but turning also did not appear to have substantially altered the

concentrations. A complete comparison of original and resampled soil concentrations of As and Cd has been provided in the supplemental material (Figures S2 and S3).

Bioaccessible Pb Measurements

Bioaccessible Pb levels were obtained for 18 of the 20 gardens sampled. Insufficient soil from the original samples remained for gardens 1 and 9. All gardens tested had very low bioaccessible percentages, with a maximum of 1.8 percent of the total Pb being bioaccessible. Furthermore, there was no observable correlation between a garden's average total Pb concentration and its bioaccessible Pb percentage. The low levels of bioaccessible Pb in the raised beds indicate that Pb contamination through soil is not a major risk for St. Louis gardeners, as less than two percent of the total Pb was bioaccessible in the 18 gardens tested. This value is much lower than the bioaccessible fractions measured in other soils, such as soils in Joplin, Missouri, which had an estimated bioaccessible fraction of 29.7 percent based on the USBLT (Bugdalski et al., 2014). A study which specifically assessed potential urban garden soils in Cleveland, Ohio using the Relative Bioaccessibility Leaching Procedure (RBALP) also had higher bioaccessible fractions (Minca et al., 2013). As with the USBLT procedure used in the present study, the RBALP begins with an extraction in HCl with glycine added, and it then includes a subsequent step to simulate leaching in the small intestine. When the RBALP procedure was run at its typical pH of 1.5, the mean bioaccessible fraction was 72 percent for those soils, while a modified version of the procedure, run at pH 2.5, yielded a mean bioaccessible fraction of 38 percent (Minca et al., 2013).

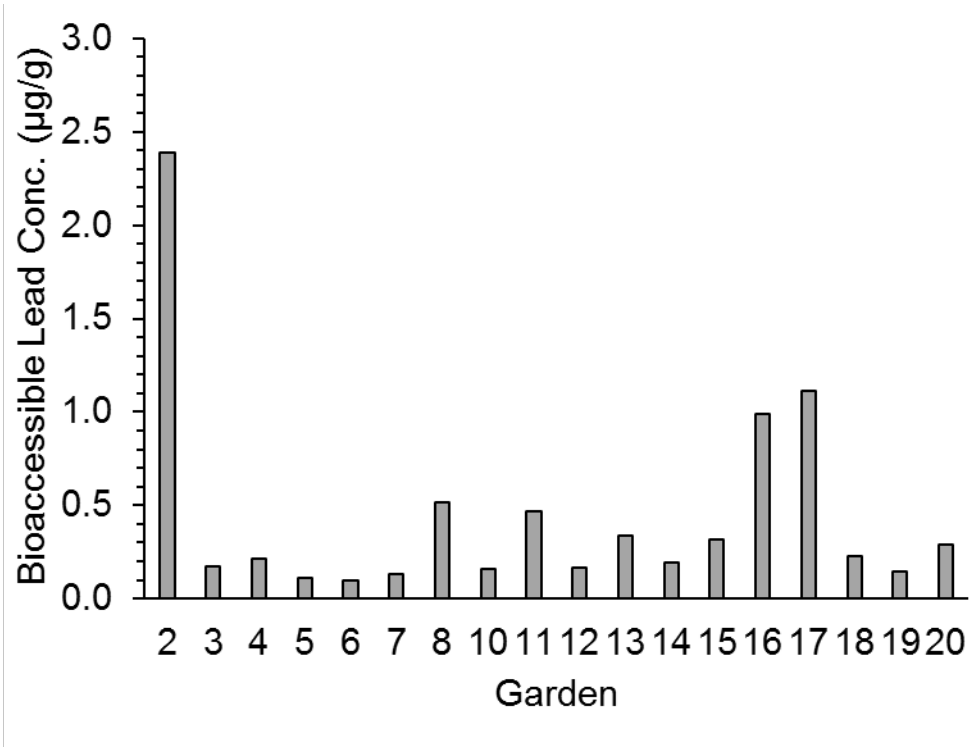

Figure 4. Average bioaccessible lead concentrations in soils

Tomato Leaves

Arsenic content in tomato leaves tended to be low regardless of the As concentration in the soil, with all but one leaf falling below 1 µg/g, and the remaining leaves containing 1.54 µg/g. Cadmium concentrations in the leaves ranged from 0.09 to 2.15 µg/g. Leaves from the same plot tended to be closely grouped in their Cd levels, although some plots had one leaf that was notably higher than the others collected in the plot. Copper levels were similarly closely clustered, with leaves in low copper soils ultimately taking up similar amounts of copper as those in high copper soils. While concentrations in leaves are only an indirect indication of

concentrations that would be present in the tomatoes themselves, the data do suggest limited transfer of As and Cd from the soil into the plants. These results are in line with other research into As uptake, which found that tomatoes grown in soil contaminated with 36-211 µg/g As contained no more than 0.02 µg/g As in the fruit. Choice of vegetable may be significant, as a study of Boston gardens showed that Pb uptake is typically lower in fruit crops than other types of crops (Spittler and Feder, 1979). A more recent study in the Boston area that analyzed both plant tissues and soil samples concluded that soil could contribute 72-91% of lead exposure while produce consumption only 2-3% (Clark et al., 2008).

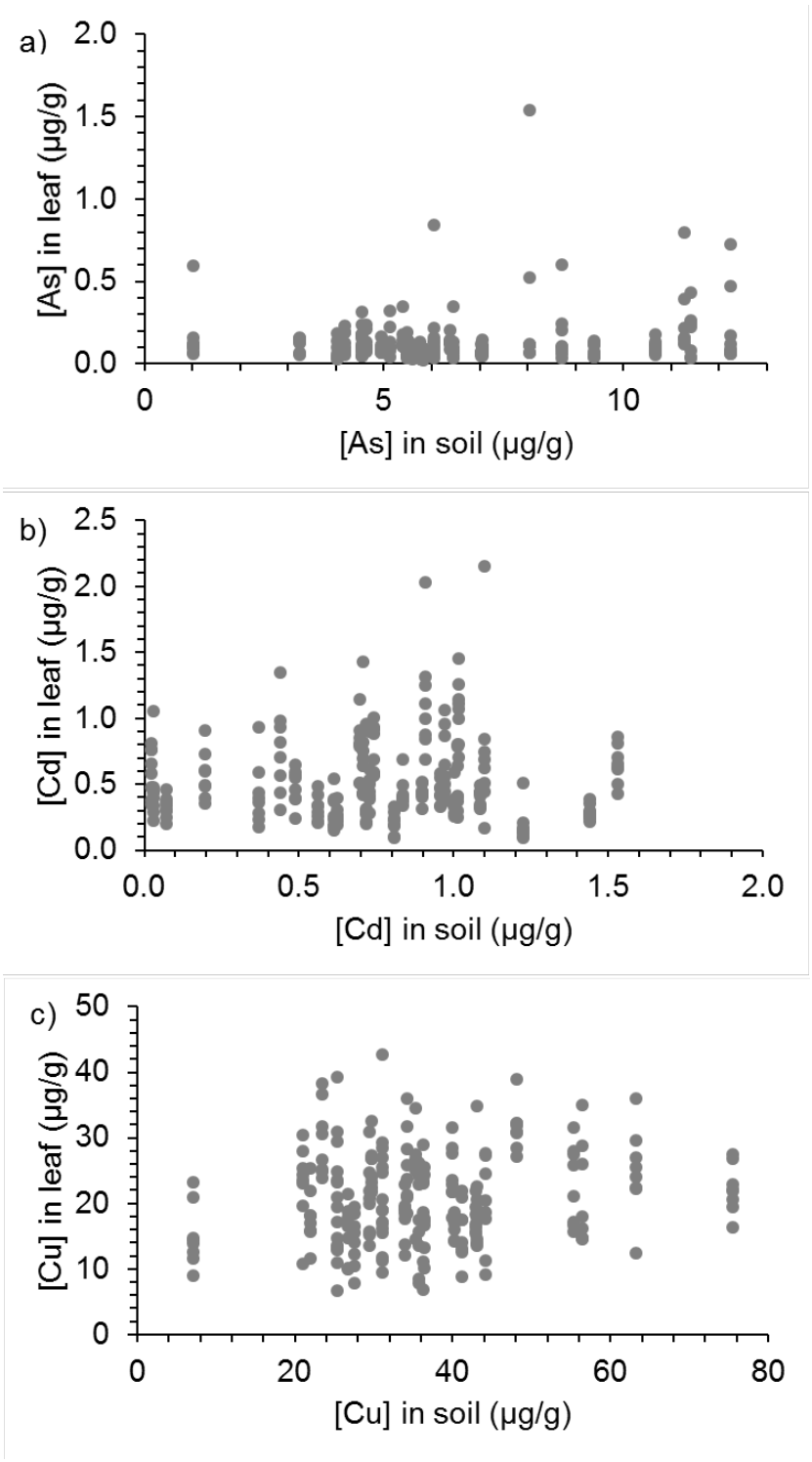

Figure 5. Relationship between concentrations of (a) arsenic, (b) cadmium, (c) copper in tomato leaves and in soils

Implications for Future Exposure Risk Assessment in Community Gardens

The results of the study can provide insights into the design of future community gardening sampling programs. There were variations in concentrations from garden to garden but also significant plot-to-plot variations for some gardens. Consequently, sampling strategies will need to balance the need for collection of multiple samples from a single garden with the desire to collect samples from many gardens across a region. The plot-to-plot variability demonstrates that it will be necessary to collect multiple samples from multiple plots in a garden to get a clear picture of metal concentrations; collection of a smaller number of samples could have obscured the ability to see garden-to-garden trends in the present study. Metal concentrations in the soils of a plot were quite consistent with time, even after some soils had been mixed by post-harvest turning of the soil, so getting soil samples from multiple locations should be a higher priority than getting soil samples at multiple times within a season. The trends in metal concentrations with garden age suggest that baseline samples should be collected when gardens are first established, and that if possible gardens should be resampled over multi-year timescales.

Collecting leaves at the same time as soil samples would be beneficial, as collecting leaves and soil simultaneously from the same plot would allow for direct comparison of metal levels in the soil to how much metal was taken up by the plant. The general trend of higher metals concentrations in older gardens may also become a concern as urban community gardens age. Investigation of the mechanisms by which clean fill soil is contaminated could potentially offer strategies for mitigating this concern. Analysis of the stable isotope composition of Pb has previously been used in southeastern

Missouri to help determine the source of Pb in soil; similar work in community gardens could shed light on the source of contamination over time (Rabinowitz and Wetherill, 1972).

There were several limitations to this study. Rather than using a random sample design, community gardens were recommended by Gateway Greening and six gardens opted to not participate in this study. Therefore, selection bias may be present and there could be differences between the gardens visited and those that chose not to participate. Future work with these gardens could also explore the levels of organic compounds in soils. Although toxic metals levels were below EPA soil standards, other chemicals including pesticides, polycyclic aromatic hydrocarbons (PAHs), polychlorinated biphenyls (PCBs), and petroleum products were not assessed and could be present in soils. These chemicals have been associated with a myriad of adverse health outcomes and persistent exposure may increase the risk for individuals in direct contact. The statistical strength of the findings is also limited by the sample size, and the results of the study can also not be generalized yet to urban gardens in other cities.

Conclusions

Soil sampling found that toxic metals were generally present in St. Louis community garden soils at concentrations below EPA screening levels. Additionally, the Pb that was present did not appear to be readily bioaccessible, as an in vitro bioaccessibility test found that less than two percent of the Pb in the soils tested was bioaccessible. Analysis of leaves from tomato plants—the crop most commonly grown

by gardeners surveyed—from the same gardens found that uptake of As and Cd in plants was similarly low. Future work should focus on regional trends in metal concentrations and mechanisms for recontamination, which may help gardeners better assess how to minimize exposure as their gardens mature.

Acknowledgements

This project was supported by the International Center for Advanced Renewable Energy and Sustainability at Washington University. We are grateful to Qingqing Zeng for performing the USBLT tests and to Ivan Baxter and Greg Ziegler of the Donald Danforth Plant Sciences Center for assistance with tomato leaf analysis. Gateway Greening played a critical role in identifying gardens for inclusion in the study and helping us coordinate with garden leaders. Finally, we appreciate the participation of the gardeners who provided access to their plots and who agreed to be interviewed for this study.

Appendix C. Iron production, urbanism, and environmental sustainability along the Medieval Silk Road: ecological niche construction and ancient industrial development at the highland smelting center Tashbulak, Uzbekistan

Appendix C is a summary of a field study and post-field lab work. It was performed as part of the interdisciplinary project "Iron production, urbanism, and environmental sustainability along the Medieval Silk Road: ecological niche construction and ancient industrial development at the highland smelting center Tashbulak, Uzbekistan" that was led by Dr. Michael Frachetti from the Anthropology Department at Washington University in St. Louis and involved team members from inside and outside of the university. I joined the 28-day field campaign in Uzbekistan, which included soil coring, trench excavations and sampling works. I guided an undergraduate student to process samples and determine the elemental composition, and I finished data analysis and interpretation. The content of this research has been included into the whole project findings, which is in preparation for publication to a peer-reviewed journal.

Background

This project was focused on the newly discovered medieval Silk Road city of Tashbulak (Uzbekistan), located in a high altitude environmental context unmodified by modern development. From a previous survey, a large urban complex was discovered and the area was assumed to have undergone intensive industrial development centuries before

the Industrial Revolution. The primary objective of the current project was to investigate the development of the urban sites in the medieval Qarakhanid period (10th-12th c. CE) and its ecology, chronology, environmental history, and cultural landscape of the society. Our main goal was to test for the geochemical signatures of intensive iron ore production and to assess how such production impacted the local biogeochemistry of the soil and forest ecosystem.

General Coordinate System and Field Work Procedures:

The area of investigation around the site was systematically labelled as a site-wide grid system. The first scale is based on 10 m × 10 m 'quadrats' that cover the entirety of the site area, using A-JJ to represent the north-south direction and numbers (1-33) for the east-west direction. The second scale is inside a 10 m × 10 m unit, where it is further divided into 1m x 1m grids, using letters 'a-j' to represent the east-west direction and numbers (1-10) for the north south direction. Based on this grid system, each excavation trench can be located in the map.

I was involved in daily fieldwork with the Geoarchaeology team and we undertook the geographic and geological reconnaissance to understand the basic information of the site and its soil context. Then soil coring was conducted over the site to understand more specific information of soil development at small areas of the site. After having an idea for the basic environment of the site, a set of trenches were excavated in both archaeological and nonarchaeological contexts to see if there was any evidence of human impact on the site development and the environments. Soil samples

from a greater distance (upstream of the site) were collected for comparison as background information. For each excavated trench, soil profiles were studied to distinguish the soil context, to record the horizons and to discover featured samples that have signatures from human activities.

Figure C-1. Sample profile example.

Sampling:

A total of 170 samples were collected from the Tashbulak site during June 2015. The samples were collected from excavation sites and from a set of trenches along the north-south (NS)/east-west (EW) direction, which cover both archaeological and non-archaeological contexts. From excavation units, samples were collected from the soil profiles at 10-cm intervals while other samples were collected by soil auguring at 10 cm

intervals from NS/EW trenches (depth ranges from 0.5 to 2 m, Figure C-1). Others samples were collected inside excavation sites, such as mudbrick from the cemetery, burned ashes, and sediments responsive to magnets. Sample names were labeled according to the labeling system that is consistent with other field teams, to locate them across the site. For example, for a sample taken from R14-d4-21, R14 represent a 100 × 100 m unit, d4 means a 10 × 10 m unit, 21 refers to the depth (21 being 200-210 cm below the surface) that this sample was taken from. For soil profiles, 0-10 cm means the first samples were taken from the surface. Accurate locations for all sampling sites were recorded by the main survey station.

Methods:

Samples were dried at 105 ºC for 24 hours to remove the moisture before further treatment procedures. To begin preparing the samples for digestion, approximately 2.0 grams of each dry soil sample was measured and its weight was recorded before being poured into digestion tubes. Digestion tubes were filled with 8.0 mL of concentrated nitric acid and 2.0 mL of concentrated hydrochloric acid. Digestion tubes were placed in a heated aluminum digestion block at 100°C for four hours. When the digestion was complete, the tubes were allowed to cool before ultrapure water was added to reach a final volume of 50 mL. Extractants were filtered by 0.22 µm PES (polyethersulfone) filters and diluted by a factor of 20 and run through ICP-MS to determine concentrations of the major elements (Ca, K, Na, Mg and Fe) and trace elements (Cr, Mn, Co, Ni, Cu, Zn, As, Ag, Cd, Pb, U).

Results and Discussions:

Based on the data gathered in these procedures, there are a few patterns. Many elemental concentrations show no clear dependence on depth, with the exception of Ca, which increases as the C horizon (rich in carbonates) is approached. Most elements studied also showed fairly consistent concentrations throughout the different site locations as well, with the exception of lead, copper, and silver. These three elements displayed drastically elevated concentrations in the feature samples taken from the R14 site, which was assumed to be the production center. This is echoed by the depth profiles for the Sondage samples (upstream, studied as the background sediments) and for R14-d4, R14-e4 and R14-e5, which also show noticeably greater concentrations of copper in comparison to Sondage. In examining the element correlations among all samples, these three elements also showed a similar pattern of heightened concentrations when correlated with other elements (Figure 2). Other pairs of elements showed either predictable proportional increases without any stand-out points or scattered concentrations with little to no correlation at all.

While Tashbulak was originally thought to have had an iron smelting facility, it appears that the activity at this site may have included metals other than iron. Iron concentrations at the proposed facility do not differ greatly from the concentrations around the rest of the site and from the Sondage samples. Our analysis showed that lead, copper, and silver have made an unexpected appearance, which could allude to the introduction of these metals to the environment due to iron-working at the site. Overall the iron-working activity in Tashbulak did not cause any lasting impact on the surrounding environment.

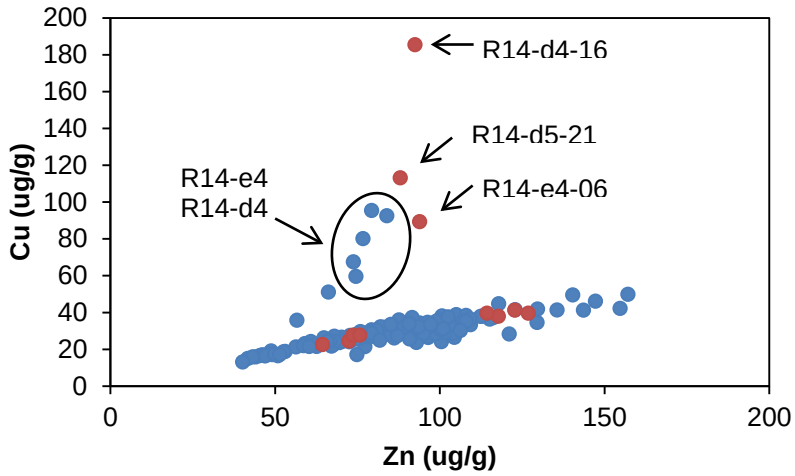

Figure C-2. Correlation between Cu and Zn among samples. Red points represent samples from featured samples and blue points represent the remaining samples.

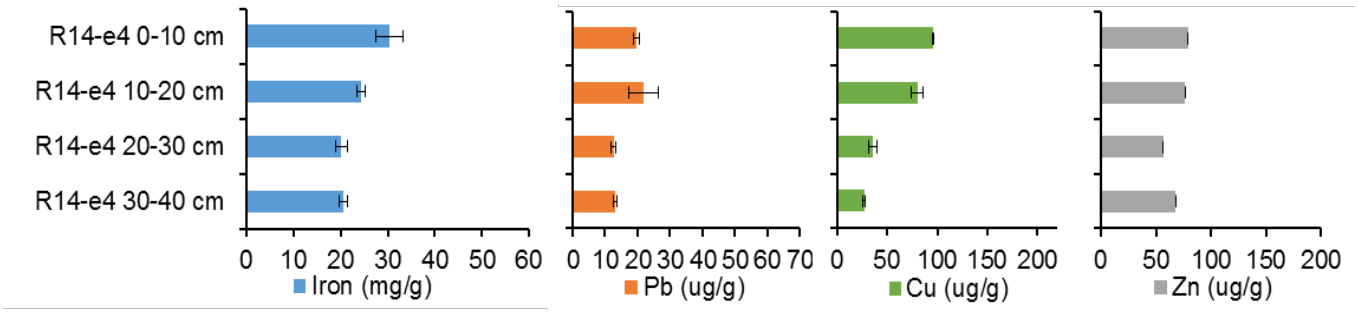

Figure C-3. Elemental concentration distribution in the depth profile (unit R14-e4 as an example)

Table C-1. Concentrations of 12 elements in soil samples (featured samples listed)

Sample	Fe (mg/g)	Pb (ug/g)	Zn (ug/g)	Cu (ug/g)	Ni (ug/g)	Ag (ug/g)	Ca (mg/g)	K (mg/g)	Na (mg/g)	Mg (mg/g)	As (ug/g)	Cr (ug/g)
Shot830 Burial 1 HM4	24.73	13.66	72.41	24.43	39.38	0.21	42.84	3.78	0.12	8.97	12.37	37.78
K12-A2 LVL 7	23.32	11.77	73.63	27.61	34.14	0.20	57.90	5.37	0.20	7.91	12.00	31.76
R14-d4-16	27.75	63.92	92.46	185.45	43.52	1.02	44.91	5.25	0.23	8.67	11.59	38.19
R14-e4-06	33.76	25.43	93.89	89.27	43.55	0.51	28.70	4.27	0.14	8.06	13.22	35.95
R14-d05-21	25.32	21.76	88.03	113.10	43.15	0.42	32.86	4.84	0.10	8.50	6.63	35.54
Shot830 Burial 1 HM4(BG)	22.58	12.41	64.40	22.57	38.42	0.19	92.58	4.05	0.13	10.15	12.75	34.16
R12-f10 Shot 713	25.19	13.50	75.70	27.69	38.31	0.14	62.02	3.78	0.10	7.98	12.83	33.63
W19-f9 cxt 11	27.16	16.91	122.79	41.25	40.91	0.26	42.66	9.24	0.28	9.12	9.48	38.36
X19-g2 cxt 6	28.02	14.44	126.85	39.58	38.88	0.28	39.95	8.78	0.29	8.53	9.11	36.42
X19-d3 cxt 5	31.44	16.08	117.79	37.94	44.81	0.24	23.70	5.20	0.13	8.76	9.61	40.14
X19-e3 cxt 5	32.24	22.10	114.35	39.55	43.28	0.23	26.23	4.80	0.19	8.01	10.63	36.53

Appendix D. Water, Metals, and Nutrition in Haiti: A Transdisciplinary Approach to Public Health Challenges in Developing Countries

Appendix D includes results from a study that aimed to examine drinking water sources in Cap Haitien, Haiti to characterize the metal contaminants and assess the temporal and spatial variability in metal contaminant levels among the main drinking water sources in Cap Haitien. I was in charge of lab preparation for sampling, sample treatment, and analysis and data interpretation. The manuscript 'Water, Metals, and Nutrition in Haiti: A Transdisciplinary Approach to Public Health Challenges in Developing Countries' has been prepared and is under revision for an anticipated submission, the authors are Zorimar Rivera-Núñeza, Zezhen Pan, Bazelais Duliencec, Daniel E. Giammar, Lora L. Iannotti.

Introduction

Water quality has been associated with nutritional deficiencies as contaminants can interfere with nutrient absorption and metabolism, affecting the manifestation of specific health outcomes (Ljung and Vahter 2007, Milton et al. 2004). In Haiti, waterborne diseases, such as cholera and other diarrheal diseases, contribute significantly to child morbidity and mortality. Although recent data suggest that exposure to environmental chemicals may pose an additional risk to public health, this has gone largely understudied (Schwartzbord et al. 2013) in the country. Toxic metals, such as

lead, may cause adverse health effects by blocking the absorption of important food nutrients thereby affecting children's growth.

Characterizing metal contamination in Haiti, as in most developing countries, is challenging because of the lack of water quality data, poor drinking water infrastructure, variability of water contaminants, and factors interacting with water-use activities, such as storage. Water quality monitoring systems and data may allow for the identification of contamination sources and variability of water contaminants. This information is extremely important to identify pathways of exposure and potential risks that may produce adverse health effects. Our team applied a transdisciplinary framework (Haire-Joshu and McBride 2013) to integrate research questions and perspectives with a view towards improving child health and development in Haiti. This study aimed to examine drinking water sources in Cap Haitien to characterize the metal contaminants and assess the temporal and spatial variability in metal contaminant levels among the main drinking water sources in Cap Haitien.

Methods

Study Area

Cap Hatien is the second largest city in Haiti, after Port-au-Prince, with a population of approximately 190,000. We have been conducting nutrition and public health research in Cap Haitien for over 6 years (Iannotti et al. 2014, Iannotti et al. 2015b). One randomized controlled trial (RCT) that assessed the impact of a nutrition intervention on child growth and morbidities was conducted at the Fort Saint Michel

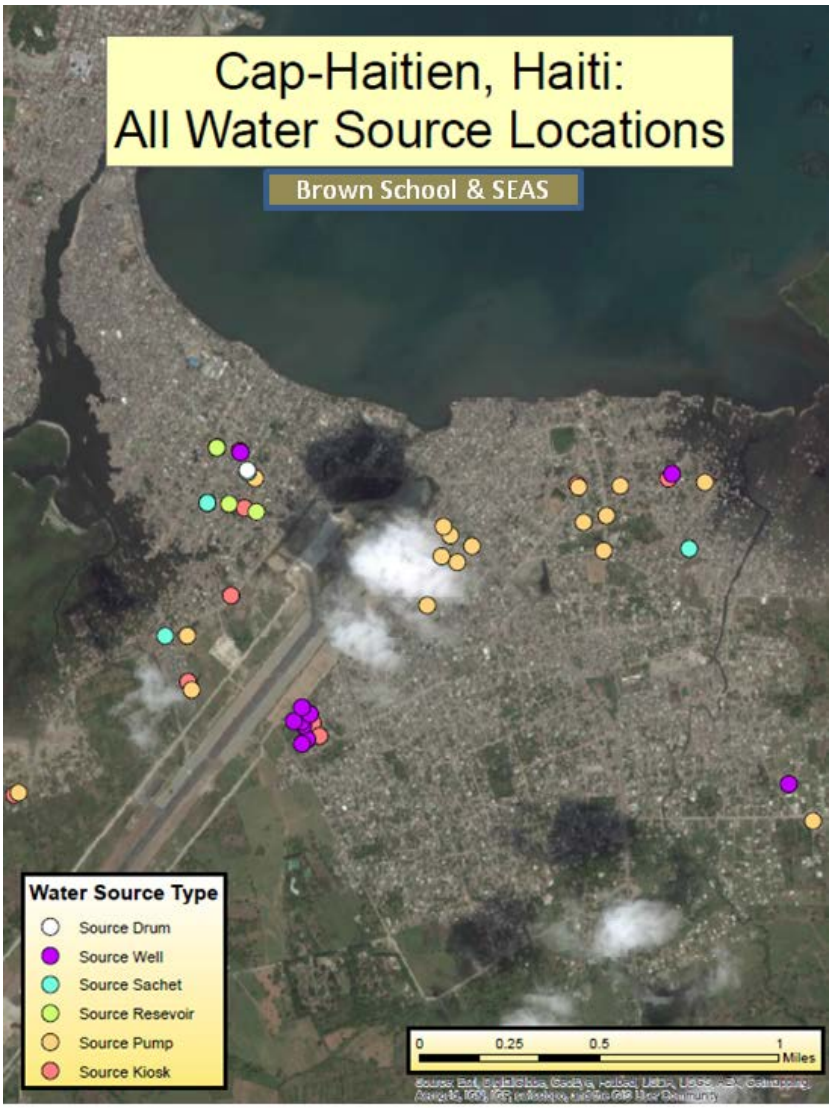

Figure D1. Sampling locations in Cap-Haitien, Haiti.

(FSM) clinic, located in the poorest communal section of the city: Petite Anse.(Iannotti et al. 2014) The catchment area for the clinic borders a small international airport, a major road, and a canal. Water sampling was complemented with data on water-use activities obtained previously from the mothers enrolled in the RCT. The area was divided in five different communities. Water sources in the communities included direct (i.e., public

pumps, wells) and indirect groundwater use sources (i.e., sachets, kiosks, drums, and reservoirs). Direct water sources included public pumps usually built by the government and serve communities of about 40-50 individuals, and wells for individual families (private well) or smaller communities (15-20 individuals). Kiosks are small businesses, generally 1-2 per community, and sell drinking water that has been treated through reverse osmosis. Sachets are small plastic bags containing water that has also been treated through reverse osmosis and that is sold by vendors to entire communities. Reservoirs and drums are large concrete tanks that are filled by the government or through rainwater harvesting.

Collection and Analysis of Water Samples

Water samples were collected during summer (June) and fall (October) of 2014 to evaluate and account for a potential seasonal variability. In order to determine toxic metal concentrations, water samples were collected in acid-washed low-density polyethylene bottles. Measurements of dissolved oxygen, temperature, conductivity, pH, nitrate, nitrite, and phosphate were conducted *in situ* using field instruments. All collected samples (incl. blanks and positive controls) were initially stored on ice and then transported for analyses to Washington University in St. Louis, Missouri. Water samples were filtered through 0.22 µm filters (PES membranes, Environmental Express) and acidified to 1% HNO_3 before analysis. Concentrations of 17 elements were measured using inductively coupled plasma-mass spectrometry (ICP-MS, Perkin-Elmer).

Statistical and Geographic Information System Analysis

Descriptive statistics were calculated for all analysed toxic metal concentrations and chemical parameters in drinking water sources using the SAS 9.4 statistical package. The magnesium to calcium (Mg/Ca) and barium to calcium (Ba/Ca) ratios were calculated as they are indicators of a contamination with seawater. Water source positional information was recorded using GPS (GPS unit information under preparation) and was then fed into the ArcMap 10.2.2 Geographic Information Systems Software to create an accurate map of the study area.

Results

Table 1 lists the metal concentrations and chemical parameters by drinking water source. Overall, metal concentrations were below the U.S. Environmental Protection Agency (USEPA) drinking water standards. The most common drinking water sources, as previously identified, were public pumps and wells[9] which showed overall higher concentrations for almost all metals. Barium concentrations were higher in summer than in fall (statistically significant, data not shown). One sampling location was above the USEPA 2,000 µg/L drinking water standard for barium but only during summer (2,460 µg/L). At a different sampling location, the arsenic concentration was above the USEPA drinking water standard during both summer and fall (41.7 µg/L and 57.8 µg/L, respectively). Manganese levels were higher in wells than in other water sources, and higher than those found in drinking water sources in the US. Although the USEPA does

not have a primary drinking water standard for manganese, their secondary standard based on cosmetic or aesthetic effects is 50 μg/L.

The elemental composition of the water samples can be an indication for an intrusion of seawater at a particular location. Figure D2 shows the relationship between barium, magnesium, and calcium with conductivity. Most locations showed low mean Mg/Ca and Ba/Ca ratios and only a few locations, closer to the ocean, exhibited elevated ratios (2.3-3.4). While elemental magnesium, calcium, and barium concentrations were moderately correlated with conductivity (0.77, 0.64, and 0.42, respectively), the mean Mg/Ca and Ba/Ca ratios exhibited only a poor correlation (0.23 and 0.05, respectively).

Discussion

This study assessed the quality of drinking water sources in five communities in Cap Haitien, Haiti. While the main toxic metals were below the EPA drinking water standards, emerging contaminants, such as manganese, with potentially important implications for child development, showed levels above the recommended thresholds. In resource-poor populations, toxic metal exposure should be considered within the framework of underlying mineral deficiencies, in particular since elements with similar coordination chemistry will compete for enteric absorption pathways. Further, in many developing countries exposure to chemicals is not regulated or monitored.

Based on this preliminary study, ground water toxic metal concentrations in Cap Haitien appear to be very low despite the lack of waste management, illegal dumping practices, waste dumps, and in the absence of any demarcation between residential and

industrial areas. This appears to contrast with the situation in Port-au-Prince, where the groundwater was found to contain greatly elevated levels of toxic metals, including lead and chromium, at concentrations in excess of U.S. regulatory values (Emmanuel et al. 2007, Emmanuel et al. 2009). A higher industrial activity in combination with extensive transportation systems in the capital may explain this difference.

Manganese occurs naturally in many surface and ground water sources but can also be present due to anthropological sources including pesticides, unleaded gasoline, fertilizers, and livestock feeding supplements. In Haiti, we observed an inverse correlation between manganese and dissolved oxygen suggesting groundwater contamination from natural sources. In view of the potential adverse health effects caused by manganese and the elevated concentrations found in many parts of the world, the USEPA recently listed manganese for the first time in the Drinking Water Contaminant Candidate List (CCL) (Ljung and Vahter 2007). The neurotoxicity of manganese after occupational exposures has been well documented (Levy and Nassetta 2003), and there is increasing evidence of neurotoxicity if consumed orally, especially in early life (Bouchard et al. 2007, Pappas et al. 1997, Tsai et al. 2015, Wasserman et al. 2006, Woolf et al. 2002). Manganese is also an essential micronutrient required for the functioning of many enzymes (e.g., pyruvate carboxylase) and can serve to activate many others (e.g., kinases, decarboxylases) (Lonnerdal 1994).

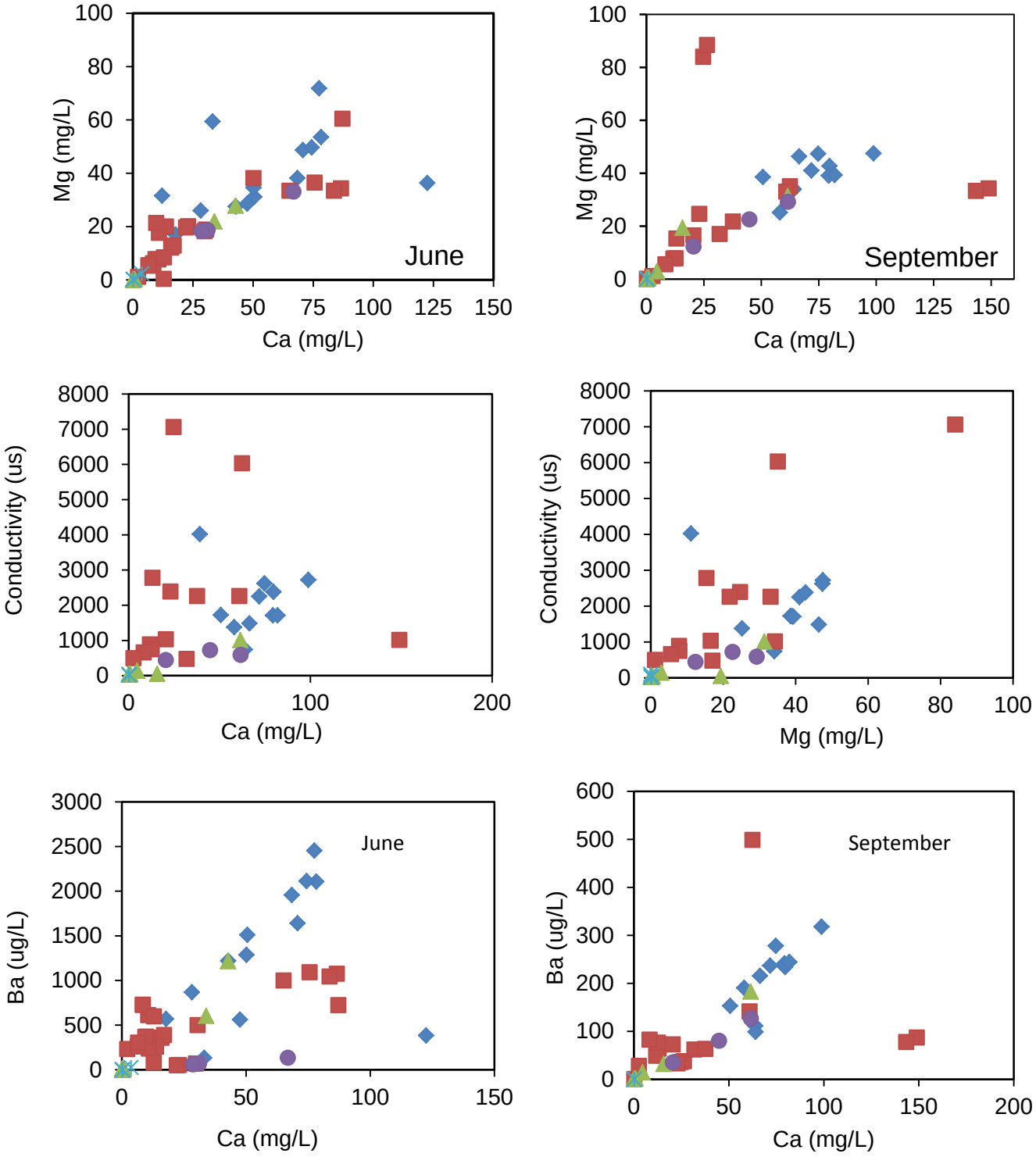

Figure D2. Mg concentration as a function of Ca concentrations from collected samples in June and September. Correlations between conductivity and Ca or Mg concentrations. ◆ :well; ■: pump; : kiosk; O: reservoir; *: sachet.

Of particular note might be the underlying public health issue of iron deficiency in undernourished populations of Haiti (Iannotti et al. 2015a), as manganese absorption may be higher with iron deficiency and can replace iron in the enzyme cytosolic aconitase with consequences for translational events (Gropper et al. 2009).

Overall, the seasonal variability of metal concentrations was very low but samples were collected during two time periods only (summer and fall). The higher Ba/Ca ratio during summer may indicate different interactions between seawater and groundwater throughout the year. Additionally, the spatial variation of the Ba/Ca ratio may indicate the potential risk of saltwater intrusion. Saltwater intrusion is the movement of saline water into a freshwater aquifer, which can lead to contamination of drinking water sources. It is possible that the increased extraction of water from wells for drinking purposes in Cap Haitien has facilitated the intrusion of marine water to portions of the local aquifer. A saltwater intrusion not only decreases the freshwater storage capacity of the aquifer but may also have adverse effects on the health of human populations who use the affected aquifer as their primary source for drinking water. Marine water is rich in chloride, sodium, magnesium, and calcium ions with a typical salinity around 35g/kg. The moderate-to-high correlations of some of these ions with conductivity measurements suggest their presence in well water samples. Although these ions are micronutrients essential to human health with deficiencies leading to morbidity and mortality, their excess may cause toxicity (IOM 2010).

The main limitation of this preliminary study is the lack of waterborne pathogen data to further examine associations between toxic metals and waterborne pathogens.

These interactions may cause diarrhoea and lead to other adverse health outcomes. Additionally, only the total metal concentration was measured in water samples. The ability to differentiate between different oxidation states of the same metal, or speciation, is very important for some metals since different species represent different toxicities. For example, it is well known that arsenic trivalent species (e.g., arsenite) are more toxic than pentavalent species (e.g., arsenate) (Hughes et al. 2011). Despite these limitations, the preliminary data presented here provide valuable information to plan future nutrition interventions in Cap Haitien, in particular since this type of data is notoriously sparse in most resource-poor country settings.

Chronic exposure to chemicals, including metals, is a growing global problem. In many developing countries, the lack or poor quality of environmental monitoring data represents a challenge not only for the assessment of environmental threats but also for the examination of interactions between metals and other areas of public health, including nutrition. Environmental chemicals can interact with nutrition and may affect health outcomes in two main ways: 1) the nutritional status may influence the level of chemical exposure and toxicity; and 2) nutritional deficiencies and chemicals affect similar health outcomes (Kordas et al. 2007). Certain populations, such as pregnant or lactating women and young children, may have a higher risk of experiencing adverse effects of chemical-nutrient interactions due to their higher nutrient requirements. These segments of the population are also more susceptible to waterborne pathogens, which is the number one cause of diarrhoea and other nutrition-related conditions in resource-poor countries.

Evaluating these interactions requires a transdisciplinary approach introducing strategies and methods across several fields.

This study combined nutrition, environmental health, and environmental geochemistry to develop an initial research framework to complement water sanitation and nutrition strategies with a view towards further assessments to understand and address child health and development challenges.

Financial Support

This work was supported by the International Center for Advanced Renewable Energy and Sustainability at Washington University in St Louis.

References

California Environmental Protection Agency (2016) Chromium-6 Drinking Water MCL. http://www.waterboards.ca.gov/drinking_water/certlic/drinkingwater/Chromium6.shtml (accessed 27 April 2017)

Arai, Y., Marcus, M.A., Tamura, N., Davis, J.A. and Zachara, J.M. (2007) Spectroscopic Evidence for Uranium Bearing Precipitates in Vadose Zone Sediments at the Hanford 300-area Site. Environmental Science & Technology 41(13), 4633-4639.

Bai, J., Liu, C. and Ball, W.P. (2009) Study of Sorption-Retarded U(VI) Diffusion in Hanford Silt/Clay Material. Environmental Science & Technology 43(20), 7706-7711.

Barnett, M.O., Jardine, P.M., Brooks, S.C. and Selim, H.M. (2000) Adsorption and transport of uranium(VI) in subsurface media. Soil Sci. Soc. Am. J. 64(3), 908-917.

Bauld, N.L. (2005) Amines. 2005 http://research.cm.utexas.edu/nbauld/CHAPTER%2021.htm (accessed April 27, 2017).

Benjamin, M.M. (2014) Water chemistry, Waveland Press.

Bouchard, M., Laforest, F., Vandelac, L., Bellinger, D. and Mergler, D. (2007) Hair Manganese and Hyperactive Behaviors: Pilot Study of School-age Children Exposed through Tap Water. Environmental health perspectives 115, 122-127.

Bruce, I.J. and Sen, T. (2005) Surface Modification of Magnetic Nanoparticles with Alkoxysilanes and Their Application in Magnetic Bioseparations. Langmuir 21(15), 7029-7035.

Campbell, K.M., Kukkadapu, R.K., Qafoku, N.P., Peacock, A.D., Lesher, E., Williams, K.H., Bargar, J.R., Wilkins, M.J., Figueroa, L., Ranville, J., Davis, J.A. and Long, P.E. (2012) Geochemical, mineralogical and microbiological characteristics of sediment from a naturally reduced zone in a uranium-contaminated aquifer. Applied Geochemistry 27(8), 1499-1511.

Catalano, J.G. and Brown, G.E. (2004) Analysis of uranyl-bearing phases by EXAFS spectroscopy: Interferences, multiple scattering, accuracy of structural parameters, and spectral differences. American Mineralogist 89(7), 1004-1021.

Catalano, J.G., McKinley, J.P., Zachara, J.M., Heald, S.M., Smith, S.C. and Brown, G.E. (2006) Changes in uranium speciation through a depth sequence of contaminated Hanford sediments. Environmental Science & Technology 40(8), 2517-2524.

Chang, Y.-C. and Chen, D.-H. (2005) Preparation and Adsorption Properties of Monodisperse Chitosan-bound Fe_3O_4 Magnetic Nanoparticles for Removal of Cu(II) Ions. Journal of colloid and interface science 283(2), 446-451.

Cheng, T., Barnett, M.O., Roden, E.E. and Zhuang, J.L. (2004) Effects of phosphate on uranium(VI) adsorption to goethite-coated sand. Environmental Science & Technology 38(22), 6059-6065.

Chowdhury, F.A., Yamada, H., Higashii, T., Goto, K. and Onoda, M. (2013) CO_2 Capture by Tertiary Amine Absorbents: a Performance Comparison Study. Industrial & Engineering Chemistry Research 52(24), 8323-8331.

Chowdhury, I., Duch, M.C., Mansukhani, N.D., Hersam, M.C. and Bouchard, D. (2014) Deposition and Release of Graphene Oxide Nanomaterials Using a Quartz Crystal Microbalance. Environmental Science & Technology 48(2), 961-969.

Clesceri, L.S., Greenberg, A.E. and Eaton, A.D. (1999) Standard methods for examination of water & wastewater.

Dong, H., Guan, X., Wang, D. and Ma, J. (2011) Individual and Combined Influence of Calcium and Anions on Simultaneous Removal of Chromate and Arsenate by Fe (II) under Suboxic Conditions. Separation and purification technology 80(2), 284-292.

Emmanuel, E., Angerville, R., Joseph, O. and Perrodin, Y. (2007) Human Health Risk Assessment of Lead in Drinking Water: a Case Study from Port-au-Prince, Haiti. International journal of Environment and pollution 31(3-4), 280-291.

Emmanuel, E., Pierre, M.G. and Perrodin, Y. (2009) Groundwater Contamination by Microbiological and Chemical Substances Released from Hospital Wastewater: Health Risk Assessment for Drinking Water Consumers. Environment international 35(4), 718-726.

Fowle, D.A., Fein, J.B. and Martin, A.M. (2000) Experimental Study of Uranyl Adsorption onto *Bacillus subtilis*. Environmental Science & Technology 34(17), 3737-3741.

Fuller, C.C., Bargar, J.R., Davis, J.A. and Piana, M.J. (2002) Mechanisms of uranium interactions with hydroxyapatite: Implications for groundwater remediation. Environmental Science & Technology 36(2), 158-165.

Ge, S., Agbakpe, M., Wu, Z., Kuang, L., Zhang, W. and Wang, X. (2015) Influences of Surface Coating, UV Irradiation and Magnetic Field on the Algae Removal Using Magnetite Nanoparticles. Environmental Science & Technology 49(2), 1190-1196.

Gropper, S., Smith, J. and Groff, J. (2009) Protein. Advanced nutrition and human metabolism, 179-250.

Haire-Joshu, D. and McBride, T.D. (2013) Transdisciplinary Public Health: Research, Education, and Practice, John Wiley & Sons.

Hao, Y.-M., Man, C. and Hu, Z.-B. (2010) Effective Removal of Cu (II) Ions from Aqueous Solution by Amino-functionalized Magnetic Nanoparticles. Journal of Hazardous Materials 184(1), 392-399.

Heald, S.M. (2011) Optics upgrades at the APS beamline 20-BM. Nuclear Instruments & Methods in Physics Research Section a-Accelerators Spectrometers Detectors and Associated Equipment 649(1), 128-130.

Heald, S.M., Brewe, D.L., Stern, E.A., Kim, K.H., Brown, F.C., Jiang, D.T., Crozier, E.D. and Gordon, R.A. (1999) XAFS and micro-XAFS at the PNC-CAT beamlines. Journal of Synchrotron Radiation 6, 347-349.

Hsi, C.-k.D. and Langmuir, D. (1985) Adsorption of Uranyl onto Ferric Oxyhydroxides: Application of the Surface Complexation Site-binding Model. Geochimica et Cosmochimica Acta 49(9), 1931-1941.

Hu, J., Chen, C., Zhu, X. and Wang, X. (2009) Removal of Chromium from Aqueous Solution by Using Oxidized Multiwalled Carbon Nanotubes. Journal of Hazardous Materials 162(2), 1542-1550.

Hu, J., Lo, I.M. and Chen, G. (2005) Fast Removal and Recovery of Cr (VI) Using Surface-modified Jacobsite ($MnFe_2O_4$) Nanoparticles. Langmuir 21(24), 11173-11179.

Hughes, M.F., Beck, B.D., Chen, Y., Lewis, A.S. and Thomas, D.J. (2011) Arsenic Exposure and Toxicology: a Historical Perspective. Toxicological Sciences 123(2), 305-332.

Iannotti, L.L., Delnatus, J.R., Odom, A.R., Eaton, J.C., Griggs, J.J., Brown, S. and Wolff, P.B. (2015a) Determinants of Anemia and Hemoglobin Concentration in Haitian School-aged Children. The American journal of tropical medicine and hygiene 93(5), 1092-1098.

Iannotti, L.L., Dulience, S.J.L., Green, J., Joseph, S., François, J., Anténor, M.-L., Lesorogol, C., Mounce, J. and Nickerson, N.M. (2014) Linear Growth Increased in Young Children in An Urban Slum of Haiti: a Randomized Controlled Trial of a Lipid-based Nutrient Supplement. The American journal of clinical nutrition 99(1), 198-208.

Iannotti, L.L., Henretty, N.M., Delnatus, J.R., Previl, W., Stehl, T., Vorkoper, S., Bodden, J., Maust, A., Smidt, R. and Nash, M.L. (2015b) Ready-to-use Supplementary Food Increases Fat Mass and BMI in Haitian School-aged Children. Journal of Nutrition 145(4), 813-822.

IOM (2010) Dietary Reference Intakes Tables and Application, The National Academies of Sciences Engineering Medicine.

Jerden, J.L. and Sinha, A.K. (2003) Phosphate based immobilization of uranium in an oxidizing bedrock aquifer. Applied Geochemistry 18(6), 823-843.

Jiang, W., Cai, Q., Xu, W., Yang, M., Cai, Y., Dionysiou, D.D. and O'Shea, K.E. (2014) Cr (VI) Adsorption and Reduction by Humic Acid Coated on Magnetite. Environmental Science & Technology 48(14), 8078-8085.

Johnston, C.P. and Chrysochoou, M. (2012) Investigation of Chromate Coordination on Ferrihydrite by In Situ ATR-FTIR Spectroscopy and Theoretical Frequency Calculations. Environmental Science & Technology 46(11), 5851-5858.

Kanematsu, M., Perdrial, N., Um, W., Chorover, J. and O'Day, P.A. (2014) Influence of Phosphate and Silica on U(VI) Precipitation from Acidic and Neutralized Wastewaters. Environmental Science & Technology 48(11), 6097-6106.

Kazy, S.K., D'Souza, S.F. and Sar, P. (2009) Uranium and Thorium Sequestration by a *Pseudomonas* sp.: Mechanism and Chemical Characterization. Journal of Hazardous Materials 163(1), 65-72.

Kordas, K., Lönnerdal, B. and Stoltzfus, R.J. (2007) Interactions between Nutrition and Environmental Exposures: Effects on Health Outcomes in Women and Children. Journal of Nutrition 137(12), 2794-2797.

Langrrd, S. (1990) One Hundred Years of Chromium and Cancer: a Review of Epidemiological Evidence and Selected Case Reports. American journal of industrial medicine 17(2), 189-214.

Lee, S.S., Li, W., Kim, C., Cho, M., Catalano, J.G., Lafferty, B.J., Decuzzi, P. and Fortner, J.D. (2015a) Engineered Manganese Oxide Nanocrystals for Enhanced Uranyl Sorption and Separation. Environmental Science: Nano 2(5), 500-508.

Lee, S.S., Li, W., Kim, C., Cho, M., Lafferty, B.J. and Fortner, J.D. (2015b) Surface Functionalized Manganese Ferrite Nanocrystals for Enhanced Uranium Sorption and Separation in Water. Journal of Materials Chemistry A 3(43), 21930-21939.

Levy, B.S. and Nassetta, W.J. (2003) Neurologic Effects of Manganese in Humans: a Review. International journal of occupational and environmental health 9(2), 153-163.

Li, W., Hinton, C.H., Lee, S.S., Wu, J. and Fortner, J.D. (2016a) Surface Engineering Superparamagnetic Nanoparticles for Aqueous Applications: Design and Characterization of Tailored Organic Bilayers. Environmental Science: Nano 3, 95-93.

Li, W., Lee, S.S., Wu, J., Hinton, C.H. and Fortner, J.D. (2016b) Shape and Size Controlled Synthesis of Uniform Iron Oxide Nanocrystals through New Non-hydrolytic Routes. Nanotechnology 27(32), 324002.

Li, W., Liu, D., Wu, J., Kim, C. and Fortner, J.D. (2014) Aqueous Aggregation and Surface Deposition Processes of Engineered Superparamagnetic Iron Oxide Nanoparticles for Environmental Applications. Environmental Science & Technology 48(20), 11892-11900.

Li, W., Mayo, J.T., Benoit, D.N., Troyer, L.D., Lewicka, Z.A., Lafferty, B.J., Catalano, J.G., Lee, S.S., Colvin, V.L. and Fortner, J.D. (2016c) Engineered

Superparamagnetic Iron oxide Nanoparticles for Ultra-enhanced Uranium Separation and Sensing. Journal of Materials Chemistry A 4(39), 15022-15029.

Li, W., Troyer, L.D., Lee, S.S., Wu, J., Kim, C., Lafferty, B.J., Catalano, J.G. and Fortner, J.D. (2017) Engineering Nanoscale Iron Oxides for Uranyl Sorption and Separation: Optimization of Particle Core Size and Bilayer Surface Coatings. ACS Applied Materials & Interfaces 9(15), 13163-13172.

Liu, C., Shi, Z. and Zachara, J.M. (2009a) Kinetics of Uranium(VI) Desorption from Contaminated Sediments: Effect of Geochemical Conditions and Model Evaluation. Environmental Science and Technology 43(17), 6560-6566.

Liu, C., Zachara, J.M., Yantasee, W., Majors, P.D. and McKinley, J.P. (2006) Microscopic reactive diffusion of uranium in the contaminated sediments at Hanford, United States. Water Resources Research 42(12).

Liu, J., Zhao, Z. and Jiang, G. (2008) Coating Fe_3O_4 Magnetic Nanoparticles with Humic Acid for High Efficient Removal of Heavy Metals in Water. Environmental Science & Technology 42(18), 6949-6954.

Liu, T., Rao, P. and Lo, I.M. (2009b) Influences of Humic acid, Bicarbonate and Calcium on Cr (VI) Reductive Removal by Zero-valent Iron. Science of The Total Environment 407(10), 3407-3414.

Ljung, K. and Vahter, M. (2007) Time to Re-evaluate the Guideline Value for Manganese in Drinking Water? Environmental health perspectives 115, 1533-1538.

Locock, A.J., Burns, P.C., Duke, M.J.M. and Flynn, T.M. (2004a) Monovalent cations in structures of the meta-autunite group. The Canadian Mineralogist 42(4), 973-996.

Locock, A.J., Burns, P.C. and Flynn, T.M. (2004b) Divalent transition metals and magnesium in structures that contain the autunite-type sheet. The Canadian Mineralogist 42(6), 1699-1718.

Lonnerdal, B. (1994) Manganese nutrition of infants. Manganese in Health and Disease. CRC Press, Boca Raton, FL, 175-191.

Mehta, V.S., Maillot, F., Wang, Z., Catalano, J.G. and Giammar, D.E. (2014) Effect of co-solutes on the products and solubility of uranium(VI) precipitated with phosphate. Chemical Geology 364(0), 66-75.

Mehta, V.S., Maillot, F., Wang, Z., Catalano, J.G. and Giammar, D.E. (2015) Transport of U(VI) through sediments amended with phosphate to induce in situ uranium immobilization. Water Research 69(0), 307-317.

Mehta, V.S., Maillot, F., Wang, Z., Catalano, J.G. and Giammar, D.E. (2016) Effect of Reaction Pathway on the Extent and Mechanism of Uranium (VI) Immobilization with Calcium and Phosphate. Environmental Science & Technology 50(6), 3128-3136.

Milton, A.H., Hasan, Z., Shahidullah, S., Sharmin, S., Jakariya, M., Rahman, M., Dear, K. and Smith, W. (2004) Association between Nutritional Status and Arsenicosis due to Chronic Arsenic Exposure in Bangladesh. International journal of environmental health research 14(2), 99-108.

Morosin, B. (1978) Hydrogen uranyl phosphate tetrahydrate, a hydrogen ion solid electrolyte. Acta Crystallographica 34 (DEC)(12), 3732-3734.

Newville, M. (2001) IFEFFIT: Interactive EXAFS analysis and FEFF fitting. Journal of Synchrotron Radiation 8, 322-324.

Olazabal, M., Nikolaidis, N., Suib, S. and Madariaga, J. (1997) Precipitation Equilibria of the Chromium (VI)/Iron (III) System and Spectrospcopic Characterization of the Precipitates. Environmental Science & Technology 31(10), 2898-2902.

Palmisano, A. and Hazen, T. (2003) Bioremediation of Metals and Radionuclides: What It Is and How It Works (2nd Edition), p. Medium: ED; Size: 45 pages.

Pan, C., Troyer, L.D., Catalano, J.G. and Giammar, D.E. (2016a) Dynamics of Chromium (VI) Removal from Drinking Water by Iron Electrocoagulation. Environmental Science & Technology.

Pan, Z., Giammar, D.E., Mehta, V., Troyer, L.D., Catalano, J.G. and Wang, Z. (2016b) Phosphate-induced Immobilization of Uranium in Hanford Sediments. Environmental Science & Technology 50(24), 13486-13494.

Pappas, B., Zhang, D., Davidson, C., Crowder, T., Park, G. and Fortin, T. (1997) Perinatal Manganese Exposure: Behavioral, Neurochemical, and Histopathological Effects in the Rat. Neurotoxicol. Teratol. 19(1), 17-25.

Payne, T.E., Brendler, V., Ochs, M., Baeyens, B., Brown, P., Davis, J., Ekberg, C., Kulik, D.A., Lutzenkirchen, J. and Missana, T. (2013) Guidelines for Thermodynamic Sorption Modelling in the Context of Radioactive Waste Disposal. Environ. Model Softw., 42, 143-156.

Peterson-Roth, E., Reynolds, M., Quievryn, G. and Zhitkovich, A. (2005) Mismatch Repair Proteins are Activators of Toxic Responses to Chromium-DNA Damage. Molecular and cellular biology 25(9), 3596-3607.

Prakash, A., Zhu, H., Jones, C.J., Benoit, D.N., Ellsworth, A.Z., Bryant, E.L. and Colvin, V.L. (2009) Bilayers as Phase Transfer Agents for Nanocrystals Prepared in Nonpolar Solvents. Acs Nano 3(8), 2139-2146.

Qafoku, N.P., Zachara, J.M., Liu, C.X., Gassman, P.L., Qafoku, O.S. and Smith, S.C. (2005) Kinetic desorption and sorption of U(VI) during reactive transport in a contaminated Hanford sediment. Environmental Science & Technology 39(9), 3157-3165.

Ravel, B. and Newville, M. (2005) ATHENA, ARTEMIS, HEPHAESTUS: data analysis for X-ray absorption spectroscopy using IFEFFIT. Journal of Synchrotron Radiation 12(4), 537-541.

Salentinig, S., Sagalowicz, L. and Glatter, O. (2010) Self-assembled Structures and pK_a Value of Oleic Acid in Systems of Biological Relevance. Langmuir 26(14), 11670-11679.

Schwartzbord, J.R., Emmanuel, E. and Brown, D.L. (2013) Haiti's Food and Drinking Water: a Review of Toxicological Health Risks. Clinical Toxicology 51(9), 828-833.

Serne, R.J., Brown, C.F., Schaef, H.T., Pierce, E.M., Lindberg, M.J., Wang, Z., Gassman, P.L. and Catalano, J. (2002) *300 Area uranium leach and adsorption project*, Pacific Northwest National Laboratory: Richland, WA, PNNL-14022.

Shang, J., Liu, C., Wang, Z. and Zachara, J. (2014) Long-term kinetics of uranyl desorption from sediments under advective conditions. Water Resources Research 50(2), 855-870.

Shi, Z., Liu, C., Zachara, J.M., Wang, Z. and Deng, B. (2009) Inhibition effect of secondary phosphate mineral precipitation on uranium release from contaminated sediments. Environmental Science & Technology 43(21), 8344-8349.

Singer, D.M., Chatman, S.M., Ilton, E.S., Rosso, K.M., Banfield, J.F. and Waychunas, G.A. (2012a) Identification of Simultaneous U(VI) Sorption Complexes and U(IV) Nanoprecipitates on the Magnetite (111) Surface. Environmental Science & Technology 46(7), 3811-3820.

Singer, D.M., Chatman, S.M., Ilton, E.S., Rosso, K.M., Banfield, J.F. and Waychunas, G.A. (2012b) U(VI) Sorption and Reduction Kinetics on the Magnetite (111) Surface. Environmental Science & Technology 46(7), 3821-3830.

Singer, D.M., Zachara, J.M. and Brown, G.E. (2009) Uranium speciation as a function of depth in contaminated Hanford sediments - A micro-XRF, micro-XRD, and micro- and bulk-XAFS study. Environmental Science & Technology 43(3), 630-636.

Singh, A., Catalano, J.G., Ulrich, K.U. and Giammar, D.E. (2012) Molecular-scale structure of uranium(VI) immobilized with goethite and phosphate. Environmental Science & Technology 46(12), 6594-6603.

Singh, A., Ulrich, K.U. and Giammar, D.E. (2010) Impact of phosphate on U(VI) immobilization in the presence of goethite. Geochimica Et Cosmochimica Acta 74(22), 6324-6343.

Singh, S., Barick, K. and Bahadur, D. (2011) Surface Engineered Magnetic Nanoparticles for Removal of Toxic Metal Ions and Bacterial Pathogens. Journal of Hazardous Materials 192(3), 1539-1547.

Stewart, B.D., Mayes, M.A. and Fendorf, S. (2010) Impact of Uranyl-Calcium-Carbonato Complexes on Uranium(VI) Adsorption to Synthetic and Natural Sediments. Environmental Science and Technology 44(3), 928-934.

Stoliker, D.L., Kent, D.B. and Zachara, J.M. (2011) Quantifying Differences in the Impact of Variable Chemistry on Equilibrium Uranium(VI) Adsorption Properties of Aquifer Sediments. Environmental Science & Technology 45(20), 8733-8740.

Stoliker, D.L., Liu, C., Kent, D.B. and Zachara, J.M. (2013) Characterizing particle-scale equilibrium adsorption and kinetics of uranium(VI) desorption from U-contaminated sediments. Water Resources Research 49(2), 1163-1177.

Sun, Y., Wu, Z.-Y., Wang, X., Ding, C., Cheng, W., Yu, S.-H. and Wang, X. (2016) Macroscopic and Microscopic Investigation of U(VI) and Eu(III) Adsorption on Carbonaceous Nanofibers. Environmental Science & Technology 50(8), 4459-4467.

Tang, G., Mayes, M.A., Parker, J.C., Yin, X.L., Watson, D.B. and Jardine, P.M. (2009) Improving parameter estimation for column experiments by multi-model evaluation and comparison. Journal of Hydrology 376(3-4), 567-578.

Tessier, A., Campbell, P.G.C. and Bisson, M. (1979) Sequential extraction procedure for the speciation of particulate trace-metals. Analytical Chemistry 51(7), 844-851.

Troyer, L.D., Maillot, F., Wang, Z., Wang, Z., Mehta, V.S., Giammar, D.E. and Catalano, J.G. (2016) Effect of phosphate on U (VI) sorption to montmorillonite: Ternary complexation and precipitation barriers. Geochimica Et Cosmochimica Acta 175, 86-99.

Tsai, M.-S., Liao, K.-W., Chang, C.-H., Chien, L.-C., Mao, I.-F., Tsai, Y.-A. and Chen, M.-L. (2015) The Critical Fetal Stage for Maternal Manganese Exposure. Environmental research 137, 215-221.

U.S., E. (1985) Drinking Water Health Advisory for Chromium., Prepared by the Office of Health and Environmental Assessment, Environmental Criteria and Assessment Office, Cincinnati, OH, for the Office of Drinking Water, Washington, DC.

Vermeul, V.R., Bjornstad, B.N., Fritz, B.G., Fruchter, J.S., Mackley, R.D., Newcomer, D.R., Mendoza, D.P., Rockhold, M.L., Wellman, D.M. and Williams, M.D. (**2009**) 300 Area Uranium Stabilization Through Polyphosphate Injection: Final Report.

Waite, T.D., Davis, J.A., Payne, T.E., Waychunas, G.A. and Xu, N. (1994) Uranium(VI) Adsorption to ferrihydrite: Application of a Surface Complexation Model. Geochimica et Cosmochimica Acta 58(24), 5465-5478.

Wang, L., Yang, Z., Gao, J., Xu, K., Gu, H., Zhang, B., Zhang, X. and Xu, B. (2006) A Biocompatible Method of Decorporation: Bisphosphonate-modified Magnetite

Nanoparticles to Remove Uranyl Ions from Blood. Journal of the American Chemical Society 128(41), 13358-13359.

Wang, T., Zhang, L., Li, C., Yang, W., Song, T., Tang, C., Meng, Y., Dai, S., Wang, H. and Chai, L. (2015) Synthesis of Core–shell Magnetic Fe_3O_4@ poly (m-phenylenediamine) Particles for Chromium Reduction and Adsorption. Environmental Science & Technology 49(9), 5654-5662.

Wang, T., Zhang, L., Wang, H., Yang, W., Fu, Y., Zhou, W., Yu, W., Xiang, K., Su, Z. and Dai, S. (2013) Controllable Synthesis of Hierarchical Porous Fe_3O_4 Particles Mediated by Poly (diallyldimethylammonium chloride) and Their Application in Arsenic Removal. ACS Applied Materials & Interfaces 5(23), 12449-12459.

Wang, Y., Morin, G., Ona-Nguema, G., Juillot, F., Calas, G. and Brown, G.E. (2011a) Distinctive Arsenic(V) Trapping Modes by Magnetite Nanoparticles Induced by Different Sorption Processes. Environmental Science & Technology 45(17), 7258-7266.

Wang, Z. and Giammar, D.E. (2013) Mass Action Expressions for Bidentate Adsorption in Surface Complexation Modeling: Theory and Practice. Environmental Science & Technology 47(9), 3982-3996.

Wang, Z., Lee, S.-W., Catalano, J.G., Lezama-Pacheco, J.S., Bargar, J.R., Tebo, B.M. and Giammar, D.E. (2012) Adsorption of Uranium (VI) to Manganese Oxides: X-ray Absorption Spectroscopy and Surface Complexation Modeling. Environmental Science & Technology 47(2), 850-858.

Wang, Z., Zachara, J.M., Liu, C., Gassman, P.L., Felmy, A.R. and Clark, S.B. (2008) A cryogenic fluorescence spectroscopic study of uranyl carbonate, phosphate and oxyhydroxide minerals. Radiochimica Acta 96(9-11), 591-598.

Wang, Z.M., Zachara, J.M., Boily, J.F., Xia, Y.X., Resch, T.C., Moore, D.A. and Liu, C. (2011b) Determining individual mineral contributions to U(VI) adsorption in a contaminated aquifer sediment: A fluorescence spectroscopy study. Geochimica Et Cosmochimica Acta 75(10), 2965-2979.

Wang, Z.M., Zachara, J.M., Gassman, P.L., Liu, C.X., Qafoku, O., Yantasee, W. and Catalano, J.G. (2005) Fluorescence spectroscopy of U(VI)-silicates and U(VI)-contaminated Hanford sediment. Geochimica Et Cosmochimica Acta 69(6), 1391-1403.

Wang, Z.M., Zachara, J.M., Yantasee, W., Gassman, P.L., Liu, C.X. and Joly, A.G. (2004) Cryogenic laser induced fluorescence characterization of U(VI) in hanford vadose zone pore waters. Environmental Science & Technology 38(21), 5591-5597.

Wasserman, G.A., Liu, X., Parvez, F., Ahsan, H., Levy, D., Factor-Litvak, P., Kline, J., van Geen, A., Slavkovich, V. and Lolacono, N.J. (2006) Water Manganese Exposure and Children's Intellectual Function in Araihazar, Bangladesh. Environmental health perspectives 114, 124-129.

Wazne, M., Korfiatis, G.P. and Meng, X. (2003) Carbonate Effects on Hexavalent Uranium Adsorption by Iron Oxyhydroxide. Environmental Science & Technology 37(16), 3619-3624.

Woolf, A., Wright, R., Amarasiriwardena, C. and Bellinger, D. (2002) A Child with Chronic Manganese Exposure from Drinking Water. Environmental health perspectives 110(6), 613.

Xie, X., Giammar, D.E. and Wang, Z. (2016) MINFIT: A Spreadsheet-based Tool for Parameter Estimation in an Equilibrium Speciation Software Program. Environmental Science & Technology 50(20), 11112-11120.

Xu, P., Zeng, G.M., Huang, D.L., Feng, C.L., Hu, S., Zhao, M.H., Lai, C., Wei, Z., Huang, C. and Xie, G.X. (2012) Use of Iron Oxide Nanomaterials in Wastewater Treatment: A Review. Science of The Total Environment 424, 1-10.

Xu, Y., Axe, L., Yee, N. and Dyer, J.A. (2006) Bidentate Complexation Modeling of Heavy Metal Adsorption and Competition on Goethite. Environmental Science & Technology 40(7), 2213-2218.

Yavuz, C.T., Mayo, J., William, W.Y., Prakash, A., Falkner, J.C., Yean, S., Cong, L., Shipley, H.J., Kan, A. and Tomson, M. (2006) Low-field Magnetic Separation of Monodisperse Fe_3O_4 Nanocrystals. Science 314(5801), 964-967.

Zachara, J.M., Davis, J.A., Liu, C.X., McKinley, J.P., Qafoku, N.P., Wellman, D.M. and Yabusaki, S.B. (**2005**) *Uranium geochemistry in vadose zone and aquifer sediments from the 300 area uranium plume*; Pacific Northwest National Laboratory: Richland, WA, PNNL-15121.

Zachara, J.M., Girvln, D., Schmidt, R. and Resch, C.T. (1987) Chromate Adsorption on Amorphous Iron Oxyhydroxide in the Presence of Major Groundwater Ions. Environmental Science & Technology 21(6).

Zachara, J.M., Long, P.E., Bargar, J., Davis, J.A., Fox, P., Fredrickson, J.K., Freshley, M.D., Konopka, A.E., Liu, C.X., McKinley, J.P., Rockhold, M.L., Williams, K.H. and Yabusaki, S.B. (2013) Persistence of uranium groundwater plumes: Contrasting mechanisms at two DOE sites in the groundwater-river interaction zone. Journal of Contaminant Hydrology 147, 45-72.

Zeng, H., Arashiro, M. and Giammar, D.E. (2008) Effects of Water Chemistry and Flow Rate on Arsenate Removal by Adsorption to An Iron Oxide-based Sorbent. Water Research 42(18), 4629-4636.

Zeng, H., Singh, A., Basak, S., Ulrich, K.-U., Sahu, M., Biswas, P., Catalano, J.G. and Giammar, D.E. (2009) Nanoscale Size Effects on Uranium(VI) Adsorption to Hematite. Environmental Science & Technology 43(5), 1373-1378.

Zeng, Z., Yang, S., Zhang, L. and Hua, D. (2016) Phosphonate-functionalized Polystyrene Microspheres with Controlled Zeta Potential for Efficient Uranium Sorption. RSC Advances 6(78), 74110-74116.

Zhang, F., Lan, J., Zhao, Z., Yang, Y., Tan, R. and Song, W. (2012) Removal of Heavy Metal Ions from Aqueous Solution Using Fe_3O_4–SiO_2-poly (1, 2-diaminobenzene) core–shell Sub-Micron Particles. Journal of colloid and interface science 387(1), 205-212.

Zhang, R., Chen, C., Li, J. and Wang, X. (2015) Investigation of Interaction between U(VI) and Carbonaceous Nanofibers by Batch Experiments and Modeling Study. Journal of colloid and interface science 460, 237-246.

Zhang, W. (2003) Nanoscale Iron Particles for Environmental Remediation: An Overview. Journal of Nanoparticle Research 5(3-4), 323-332.

Zhao, Y.-G., Shen, H.-Y., Pan, S.-D., Hu, M.-Q. and Xia, Q.-H. (2010) Preparation and Characterization of Amino-functionalized Nano-Fe_3O_4 Magnetic Polymer Adsorbents for Removal of Cromium(VI) Ins. Journal of materials science 45(19), 5291-5301.